

2016

Subgrid models for heat transfer in multiphase flows with immersed geometry

<https://hdl.handle.net/2144/17067>

Boston University

BOSTON UNIVERSITY
COLLEGE OF ENGINEERING

Dissertation

**SUBGRID MODELS FOR HEAT TRANSFER IN
MULTIPHASE FLOWS WITH IMMERSED GEOMETRY**

by

WILLIAM A. LANE

B.S., University of New Brunswick, 2012
M.S., Boston University, 2015

Submitted in partial fulfillment of the
requirements for the degree of
Doctor of Philosophy

2016

© 2016 by
WILLIAM A. LANE
All rights reserved, except for § 3.1,
which is © 2014 by Elsevier

Approved by

First Reader

Emily M. Ryan, Ph.D.
Assistant Professor of Mechanical Engineering

Second Reader

Daniel C. Cole, Ph.D.
Associate Professor of Mechanical Engineering

Third Reader

Sheryl M. Grace, Ph.D.
Associate Professor of Mechanical Engineering

Fourth Reader

Aaron J. Schmidt, Ph.D.
Assistant Professor of Mechanical Engineering

This dissertation is dedicated to my parents.

Acknowledgments

I would like express my deepest gratitude to the following people, without whom none of this would have been possible:

Dr. Emily Ryan, my advisor. Her unwavering patience, continuous support, and vast knowledge was invaluable over the last four years. Many lengthy discussions and emails have culminated in my research and my growth as a scientist. Furthermore, I am extremely grateful for the truly unique experience of collaborating with a diverse group of scientists from around the country as part of a much larger effort.

Jeff Dietiker, Tingwen Li, Curt Storlie, and many other CCSI members. It was a privilege to work with such exceptional scientists. The patience and support exuded throughout the CCSI project made me feel welcome, like an equal team member. I am forever grateful and have the utmost respect for the entire time.

Kathleen Alexander, my wife. There is no one else in the world that I could imagine going through this *experience* with. Your persistent support and enthusiasm kept me going, through good times and bad. You are amazing and I am excited to start the next chapter of our lives!

Bill and Mary Ann Lane, my parents. They have been there for me my entire life; always believing in me, encouraging me to do my best, and being proud, regardless of the outcome. I will forever be indebted to them.

Julie McRorie and Bradley Lane, my siblings. Their constant teasing and encouragement brought many smiles to otherwise dull days of simulations, data analysis, and writing.

And finally, my funding agency. This work was funded by the U.S. Department of Energy, Office of Fossil Energy's Carbon Capture Simulation Initiative through the National Energy Technology Laboratory.

Disclaimer

This dissertation was prepared as an account of work sponsored by an agency of the United States Government. Neither the United States Government nor any agency thereof, nor any of their employees, makes any warranty, express or implied, or assumes any legal liability or responsibility for the accuracy, completeness, or usefulness of any information, apparatus, product, or process disclosed, or represents that its use would not infringe privately owned rights. Reference herein to any specific commercial product, process, or service by trade name, trademark, manufacturer, or otherwise does not necessarily constitute or imply its endorsement, recommendation, or favoring by the United States Government or any agency thereof. The views and opinions of authors expressed herein do not necessarily state or reflect those of the United States Government or any agency thereof.

SUBGRID MODELS FOR HEAT TRANSFER IN MULTIPHASE FLOWS WITH IMMERSED GEOMETRY

WILLIAM A. LANE

Boston University, College of Engineering, 2016

Major Professor: Emily M. Ryan, Ph.D.

Assistant Professor of Mechanical Engineering

ABSTRACT

Multiphase flows are ubiquitous across engineering disciplines: water-sediment river flows in civil engineering, oil-water-sand transportation flows in petroleum engineering; and sorbent-flue gas reactor flows in chemical engineering. These multiphase flows can include a combination of momentum, heat, and mass transfer. Studying and understanding the behavior of multiphase, multiphysics flow configurations can be crucial for safe and efficient engineering design.

In this work, a framework for the development and validation, verification and uncertainty quantification (VVUQ) of subgrid models for heat transfer in multiphase flows is presented. The framework is developed for a carbon capture reactor; however, the concepts and methods described in this dissertation can be generalized and applied broadly to multiphase/multiphysics problems. When combined with VVUQ methods, these tools can provide accurate results at many length scales, enabling large upscaling problems to be simulated accurately and with calculable errors.

The system of interest is a post-combustion solid-sorbent carbon capture reactor featuring a solid-sorbent bed that is fluidized with post-combustion flue gas. As the flue gas passes through the bed, the carbon dioxide is exothermically adsorbed onto

the sorbent particles surface, and the clean gas is passed onto further processes. To prevent overheating and degradation of the sorbent material, cooling cylinders are immersed in the flow to regulate temperatures.

Simulating a full-scale, gas-particle reactor using traditional methods is computationally intractable due to the long time scale and variations in length scales: reactor, $\mathcal{O}(10\text{ m})$; cylinders, $\mathcal{O}(1\text{ cm})$; and sorbent particles, $\mathcal{O}(100\text{ }\mu\text{m})$. This research developed an efficient subgrid method for simulating such a system. A constitutive model was derived to predict the effective suspension-cylinder Nusselt number based on the local flow and material properties and the cylinder geometry, analogous to single-phase Nusselt number correlations. This model was implemented in an open source computational fluid dynamics code, MFIX, and has undergone VVUQ. Verification and validation showed great agreement with comparable highly-resolved simulations, achieving speedups of up to 100,000+ times faster. Our model is currently being used to simulate a 1 MW, solid-sorbent carbon capture unit and is outperforming previous methods in both speed and physically accuracy.

Contents

List of Tables	xii
List of Figures	xiii
1 Introduction	1
1.1 Modeling Multiphase Flows	2
1.2 Subgrid Methods	3
1.3 Upscaling & Uncertainty Quantification	6
1.4 Applications	6
1.5 Dissertation Structure	7
2 Numerical Methods	8
2.1 Governing Equations	9
2.2 Interphase Momentum Exchange	11
2.3 Interphase Energy Exchange	13
3 VVUQ Framework for Upscaling CFD	15
3.1 Gas-Particle Hydrodynamics	17
3.1.1 Setup	18
3.1.2 Statistical Analysis	22
3.1.3 Results	28
3.2 Gas-Particle Heat Transfer	37
3.2.1 Setup	37
3.2.2 Analysis	38

3.2.3	Results	39
4	Subgrid Models	43
4.1	Setup	44
4.2	Filtering Methods	47
4.3	Grid Size Determination	51
4.4	Filter Size Determination	52
4.5	Developing the Constitutive Model	54
4.6	Implementation	61
4.7	Verification	62
4.7.1	Model form	63
4.7.2	Implemented model	66
4.8	Validation	73
4.8.1	Bubbling bed	75
4.8.2	Turbulent bed	81
4.9	Uncertainty Quantification	85
4.9.1	Sensitivity analysis	85
4.9.2	Model-prediction error	86
5	Carbon Capture System	91
5.1	Setup	91
5.2	Results	93
6	Conclusions	98
6.1	VVUQ Framework for CFD	98
6.2	Subgrid Models	99
6.3	Future Work	99
A	Simulation Data	101

B Source Code	104
Bibliography	106
Curriculum Vitae	116

List of Tables

3.1	Experimental parameters and physical properties.	20
3.2	Model parameters and statistics.	23
3.3	Bayesian calibration variables.	25
4.1	Material properties and parameters.	47
4.2	Pi-group values for simulation campaign.	56
4.3	Model verification input parameters distributions.	63
4.4	Model verification input parameters, sampled using nearly orthogonal Latin hypercube sampling [93, 94].	64
4.5	Material properties for verification Case 1.	67
4.6	Material properties for verification Case 2.	70
4.7	Geometry, initial conditions, and boundary conditions for the bubbling and turbulent bed validation cases.	74
4.8	Material properties for the bubbling and turbulent bed validation cases.	74
4.9	Simulation benchmark timing for the bubbling bed case.	75
4.10	Simulation timing for the turbulent bed case.	82
4.11	First-order and total-effect Sobol indices measuring model sensitivity to parameters.	85
5.1	Geometry and boundary conditions for the 1 MW carbon capture system.	93
5.2	Material properties for the 1 MW carbon capture system.	93
A.1	Data used to generate the subgrid model.	101

List of Figures

3.1	CCSI validation hierarchy [53]. The full scale model is broken into smaller, simplified unit problems with decoupled physics.	16
3.2	Bubbling fluidized bed domains and probes: (a) system schematic; (b) experimental probe with optical and thermal sensors (top) [58], MFIX probe and measurement cells (bottom); and (c) MFIX simulation, where v_g is the gas phase velocity inflow, T is the bulk temperature, and p_o is the pressure outflow.	19
3.3	Prior distributions of the model parameters used for the sensitivity analysis: (a) coefficient of restitution, solid-solid; (b) coefficient of restitution, solid-wall; (c) packed bed void fraction; (d) friction angle, solid-solid; (e) friction angle, solid-wall; and (f) drag models, where Syamlal is the Syamlal-O'Brien drag model. The dashed lines are prior distributions and the histograms are LHS samples from the prior distributions. The prior distribution equations are listed inside their respective figures.	24
3.4	Latin Hypercube sampling steps: (a) define the prior distribution, (b) divide the distribution into equal-probability areas, and (c) randomly sample each area.	26

3·5	Bubble frequency results for 90 simulations using LHS of sizes 60 ($v_g = 12.6$ cm/s) and 30 ($v_g = \{5.5, 7.0, 11.0\}$ cm/s) for gas velocities: (a) $v_g = 5.5$, (b) $v_g = 7.0$, (c) $v_g = 11.0$, and (d) $v_g = 12.6$ cm/s; where G, W-Y, and S-O are Gidaspow, Wen-Yu and Syamlal-O'Brien drag models, respectively, and Exp. is experimental results [58].	30
3·6	Bubble phase fraction results for 90 simulations using LHS of sizes 60 ($v_g = 12.6$ cm/s) and 30 ($v_g = \{5.5, 7.0, 11.0\}$ cm/s) for gas velocities: (a) $v_g = 5.5$, (b) $v_g = 7.0$, (c) $v_g = 11.0$, and (d) $v_g = 12.6$ cm/s; where G, W-Y, and S-O are Gidaspow, Wen-Yu and Syamlal-O'Brien drag models, respectively, and Exp. is experimental results [58].	31
3·7	Results of sensitivity analysis for bubble frequency across angular location for gas velocities: (a) $v_g = 5.5$, (b) $v_g = 7.0$, (c) $v_g = 11.0$, and (d) $v_g = 12.6$ cm/s.	32
3·8	Posterior distributions of model parameters: (a) coefficient of restitution, solid-solid; (b) coefficient of restitution, solid-wall; (c) packed bed void fraction; (d) friction angle, solid-solid; (e) friction angle, solid-wall; and (f) drag models, where Syamlal is the Syamlal-O'Brien drag model. The dashed lines are prior distributions and the histograms are posterior distributions.	34
3·9	Out-of-sample bubble frequency predictions from the calibration model (including discrepancy) with 95% confidence bands for gas velocities: (a) $v_g = 5.5$, (b) $v_g = 7.0$, (c) $v_g = 11.0$, and (d) $v_g = 12.6$ cm/s; where μ is mean predicted bubble frequency, $\delta_{95\%}$ are 95% confidence bands, and Exp. is experimental results [58].	36

3·10	Refined mesh for Kim et al.'s system simulation, smallest grid cells are $1d_p$ and largest grid cells are $10d_p$: a) mesh of entire domain, b) close up of local refinement around cylinders.	38
3·11	Local heat transfer coefficients from MFIX based on different grid sizes compared with data from Kim et al. with an inlet velocity of 11 cm/s [58].	40
3·12	Temperature field around the central cylinder for different grid sizes: a) $10d_p$, b) $2d_p$, and c) $1d_p$	40
3·13	Theoretical maximum heat transfer coefficient attainable with (3.7) compared with Kim et al.'s average value [58].	42
4·1	Laboratory-scale fluidized bed simulation (left) and periodic unit-cell domain (right), where D_c is cylinder diameter, a_c is cylinder spacing, T_c is cylinder surface temperature, ϕ_s is solids fraction, p_g is gas pressure, Δp is the gas pressure drop, \mathbf{g} is gravitational acceleration, $\ell = a_c$ is the length of the domain, and CV is the control volume, shown in gray. 45	45
4·2	Scaled filtered Nusselt number vs. grid size for particle diameters: 100, 200, and 300 μm , with $\bar{\phi}_s = 0.3$ and $ \tilde{\mathbf{v}}_s = 0.5$. Error bars denote 95% confidence intervals.	52
4·3	Filter domains considered to determine the optimal filter size, expressed as integer multiples of the unit-cell size ℓ , with $\bar{\phi}_s = 0.3$ and $ \tilde{\mathbf{v}}_s = 0.5$ m/s.	53
4·4	Nusselt number vs. filter size to determine minimum acceptable filter size, with $\bar{\phi}_s = 0.3$ and $ \tilde{\mathbf{v}}_s = 0.5$. The error bars represent 95% confidence intervals.	54

4.5	The Nusselt number vs. solids fraction for $D_c/a_c = 0.25$, $ \tilde{\mathbf{v}}_s /v_t = 3.8$, and $\overline{\text{Pe}}_{cs} = 530$, except as noted by the legend. Markers represent simulated data with $\pm\sigma_{\overline{\text{Nu}}_{cs}}$ error bars and the solid lines denote the model fit.	57
4.6	The Nusselt number vs. cylinder diameter-spacing ratio for $\bar{\phi}_s = 0.3$, $ \tilde{\mathbf{v}}_s /v_t = 3.8$ and $\overline{\text{Pe}}_{cs} = 530$, except as noted by the legend. Markers represent simulated data with $\pm\sigma_{\overline{\text{Nu}}_{cs}}$ error bars and the solid lines denote the model fit.	58
4.7	The Nusselt number vs. filtered solids velocity for $\bar{\phi}_s = 0.3$, $D_c/a_c = 0.25$, and $\overline{\text{Pe}}_{cs} = 530$, except as noted by the legend. Markers represent simulated data with $\pm\sigma_{\overline{\text{Nu}}_{cs}}$ error bars and the solid lines denote the model fit.	59
4.8	The Nusselt number vs. Peclet number for $\bar{\phi}_s = 0.3$, $D_c/a_c = 0.25$, and $ \tilde{\mathbf{v}}_s /v_t = 3.8$, except as noted by the legend. Markers represent simulated data with $\pm\sigma_{\overline{\text{Nu}}_{cs}}$ error bars and the solid lines denote the model fit.	60
4.9	Model verification results showing predicted vs. observed filtered Nusselt numbers. Circles and numbers correspond to the parameter input combinations in Table 4.4. The light-red dashed line represents an exact match, and the light-blue dashed-dotted lines represent $\pm 20\%$ bands.	65
4.10	Simulation domain schematic for verification Case 1. Domain boundaries are periodic and a pressure gradient is imposed along the y-direction.	67

4.11	Simulation domains and meshes for verification Case 1: (a) high-resolution, “control” case, explicitly modeling the cylinders and fully resolving the heat transfer, $\Delta_{\text{grid}}^{\text{high-res.}}/d_p = 2$; (b) coarse-grid, explicitly modeling the cylinders, no longer fully resolving the heat transfer, $\Delta_{\text{grid}}^{\text{coarse}}/d_p = 8$; and (c) coarse-grid with subgrid model, $\Delta_{\text{subgrid}}^{\text{coarse}}/d_p = 8$.	68
4.12	Temperature profiles from verification Case 1. Shaded regions represent 95% confidence regions.	69
4.13	Simulation domain schematic for verification Case 2. Domain boundaries are periodic and a pressure gradient is imposed along the y-direction. Cylinder walls are held at $T_s = 20^\circ$ and a heat generation is added to the solids, $\Pi_s = 1K/s$	70
4.14	Simulation domains and meshes for verification case 2: (a) high-resolution, “control” case, explicitly modeling the cylinders and fully resolving the heat transfer, $\Delta_{\text{grid}}^{\text{high-res.}}/d_p = 4$; (b) coarse-grid, explicitly modeling the cylinders, no longer fully resolving the heat transfer, $\Delta_{\text{grid}}^{\text{coarse}}/d_p = 32$; and (c) coarse-grid with subgrid model, $\Delta_{\text{subgrid}}^{\text{coarse}}/d_p = 32$	71
4.15	Temperature profiles from verification Case 2. Shaded regions represent 95% confidence regions.	72
4.16	Filtered Nusselt number vs grid size for Case 2, comparing the subgrid model prediction versus the observed (simulated) values.	73
4.17	Local grid refinement along the boundary to capture the inlet conditions.	77
4.18	Initial bed height (solids fraction) for a) high-resolution case, $\Delta_{\text{grid}}^{\text{high-res.}}/d_p = 4$ and b) coarse subgrid case, $\Delta_{\text{subgrid}}^{\text{coarse}}/d_p = 128$	78
4.19	Average temperature fields for a) high-resolution case, $\Delta_{\text{grid}}^{\text{high-res.}}/d_p = 4$ and b) coarse subgrid case, $\Delta_{\text{subgrid}}^{\text{coarse}}/d_p = 128$	79

4·20	Temperature profiles for the bubbling bed along the height, averaged across the width for 100 seconds of simulation.	80
4·21	Temperature profiles for the bubbling bed along the height, averaged across the width for 100 seconds of simulation. The asterisk denotes the use of local grid-refinement near the inlet boundary.	80
4·22	Turbulent bed simulation: a) initial bed height (solids fraction) for the high-resolution case, $\Delta_{\text{grid}}^{\text{high-res.}}/d_p = 4$, b) average temperature field for the high-resolution case, and c) average temperature field for the subgrid model, $\Delta_{\text{subgrid}}^{\text{coarse}}/d_p = 128$	83
4·23	Temperature profiles for the turbulent bed along the height, averaged across the width for 20 seconds of simulation.	84
4·24	Temperature profiles for the turbulent bed along the height, averaged across the width for 100 seconds of simulation. The asterisk denotes the use of local grid-refinement near the inlet boundary.	84
4·25	Filtered Nusselt number vs filtered solids fraction. Mean predicted values are shown as a red solid line with corresponding 95% confidence intervals shown as blue dashed lines (MATLAB). The ensemble of grey lines represents 1000 bootstrap realizations.	87
4·26	Filtered Nusselt number vs ratio of cylinder diameter to spacing. Mean predicted values are shown as a red solid line with corresponding 95% confidence intervals shown as blue dashed lines (MATLAB). The ensemble of grey lines represents 1000 bootstrap realizations.	88
4·27	Filtered Nusselt number vs dimensionless filtered suspension velocity. Mean predicted values are shown as a red solid line with corresponding 95% confidence intervals shown as blue dashed lines (MATLAB). The ensemble of grey lines represents 1000 bootstrap realizations.	89

4.28	Filtered Nusselt number vs solids Peclet number. Mean predicted values are shown as a red solid line with corresponding 95% confidence intervals shown as blue dashed lines (MATLAB). The ensemble of grey lines represents 1000 bootstrap realizations.	90
5.1	1 MW carbon capture reactor: a) 3D geometry showing boundary conditions and immersed geometry, b) 2D slice approximation showing effective cylinder area, and c) dimensions of downchute and pressure outlet.	92
5.2	Snapshot of a) solids fraction and b) solids temperature fields in a 1 MW solid-sorbent carbon capture (using an ad-hoc heat transfer model [107]) after 500 seconds.	95
5.3	Snapshot of a) solids fraction, b) solids temperature, and c) carbon dioxide species fraction fields in a 1 MW solid-sorbent carbon capture (using the subgrid heat transfer model) after 500 seconds.	96
5.4	Average a) solids fraction, b) solids temperature, c) and carbon dioxide species fraction fields in a 1 MW solid-sorbent carbon capture (using the subgrid heat transfer model). Data was averaged from 200–500 seconds.	97

Nomenclature

Abbreviations

2D	two-dimensional
3D	three-dimensional
ACOSSO	Adaptive COmponent Selection and Smoothing Operator
BSS-ANOVA	Bayesian Smoothing Spline ANalysis Of VAriance
CCSI	Carbon Capture Simulation Initiative
CFD	computational fluid dynamics
CO ₂	carbon dioxide
CDMPM	continuous and discrete mixture phase models
CPM	continuous phase models
CV	control volume
DPM	dense discrete phase model
DEM	discrete element method
DOE	Department of Energy
E-E	Eulerian-Eulerian
E-L	Eulerian-Lagrangian
GT	granular temperature
LES	large eddy simulation
LHS	Latin hypercube sampling
MCMC	Markov chain Monte Carlo
MFIX	Multiphase Flow with Interphase eXchanges
MPPIC	multiphase particle-in-cell
PDE	partial differential equation
PDF	probability density function
SiO ₂	silicon dioxide
TFM	two-fluid model
UQ	uncertainty quantification
V&V	verification and validation
VVUQ	verification, validation, and uncertainty quantification

Variables¹

a_c	cylinder spacing (m)
$A-D$	constants in Syamlal-O'Brien drag model (-)
A_c	cylinder surface area (m ²)
A'_{c_i}	effective cylinder area in a computational cell (m ²)
$C_{p,g}, C_{p,s}$	specific heat capacity (J/kg·K)
d_p	diameter of solid phase particles (cm, m)
D_c	cylinder diameter (m)
D	rate of strain (1/s)
e	coefficient of restitution (-)
f_b	bubble frequency (bubbles/s)
F_s	sampling frequency (Hz)
g	gravitational acceleration (m/s ²)
G	filter function (-)
h_{cs}	suspension-cylinder heat transfer coefficient (W/m ² ·K)
h_{gs}	gas-cylinder heat transfer coefficient (W/m ² ·K)
I	unit tensor (-)
k_g, k_s	thermal conductivity (W/m·K)
K_i	granular stress constants
ℓ	unit-cell domain length (m)
L	filter length (m)
L^*	characteristic length (m)
N_b	total number of bubbles
Nu_{gs}	gas-cylinder Nusselt number (-)
Nu_{cs}	suspension-cylinder Nusselt number (-)
p	pressure (Pa)
Re_s	Reynolds number for a single particle (-)
\bar{q}_Θ	diffusive flux of granular energy (J/m ² ·s)
\dot{Q}_s	solids heat transfer rate (W)
t	time (s)
t_{bc}	total bubble contact time (s)
$t_{bc_{min}}$	minimum contact time for classification as bubble (s)
t_s	total sampling time (s)
T_g, T_s	temperature (K)
T_c	cylinder surface temperature (K)
T_{susp}	suspension temperature (K)
U_{mf}	minimum fluidization velocity (m/s)

¹Units given in nomenclature are default units and variables may be represented with different prefixes depending on the magnitude.

U_r	ratio of terminal settling velocity of a multi-particle system to that of a single particle (-)
$\mathbf{v}_g, \mathbf{v}_s$	velocity (m/s)
v_t	particle terminal velocity (m/s)
v^*	characteristic velocity (m/s)
$\mathbf{V}_g, \mathbf{V}_s$	corrected velocity (m/s)
\bar{x}	experimental inputs
\bar{y}	experimental outputs

Greek Letters

β	interphase momentum transfer coefficient
β_i	regression coefficients (-)
γ_Θ	granular energy dissipation (J/m ³ ·s)
δ	discrepancy
$\delta_{95\%}$	95% confidence bands
δ_b	bubble phase fraction (-)
Δ_x, Δ_y	computational grid cell size (m)
ϵ	measurement error
ϕ_g, ϕ_s	phase fraction (-)
Φ_g, Φ_s	corrected phase fraction (-)
η	emulator
$\bar{\theta}$	model parameters
Θ	granular temperature (m ² /s ²)
Θ_g, Θ_s	corrected temperature (-)
μ	mean bubble frequency (bubbles/s)
μ_g, μ_s	solids viscosity (kg/m·s)
Π	interphase exchange of granular energy (J/m ³ ·s)
Π_i	dimensionless Pi groups (-)
$\dot{\Pi}_s$	solids heat generation rate (K/s)
ρ_g, ρ_s	density (kg/m ³)
σ	standard deviation (-)
$\boldsymbol{\tau}_g, \boldsymbol{\tau}_s$	stress tensor (Pa)

Chapter 1

Introduction

Multiphase flows can be found in most engineering disciplines, but they are used extensively in chemical engineering systems and processes, for example, combustion, gasification, coating, fluid-catalytic cracking, and carbon capture. The flow behavior within these systems is typically chaotic and coupled with heat and/or mass transfer. These complex multiphase, multiphysics systems pose a significant problem to design engineers, who need to predict their behavior for design and process optimization. Approximations of such systems are typically done by building costly experimental systems or through computational fluid dynamics (CFD) simulations. However, few computational methods exist for simulating such systems at large scales. Traditional methods tend to scale poorly and become computationally intractable due to the long time scales and large variations in length scales. This dissertation details the framework for- and the development of an efficient subgrid method for simulating large, complex, multiphase, multiphysics systems.

1.1 Modeling Multiphase Flows

Multiphase flow defines any flow with more than one phase, typically two or three phases. These flows include both mixtures of similar phase states, e.g., oil-water (liquid-liquid) and different phase-states, e.g., air-solid particles (gas-solid). This results in many possible unique combinations of flows, each of which can behave in significantly different ways, and thus need to be modeled accordingly. Many numerical methods have been developed for- and applied to various multiphase systems. These methods can be largely broken down into three frameworks: continuous phases, discrete phases, and a hybrid of continuous and discrete phases.

Continuous phase models (CPMs), also known as Eulerian-Eulerian models, model all phases as interpenetrating continua, for example, the two-fluid model (TFM) [1]. For multi-fluid flows this is an accurate representation of the physics; however, for gas-solid flows, this involves approximating the solid phase as a fluid through constitutive models for equivalent properties (e.g, viscosity and stress). CPMs are typically applied through the mesh-based finite volume and finite element methods due to their ease of implementation: CPMs solve the same governing equations for each individual phase and simply couple them by considering the volume fraction of each phase present and transport coupling terms (e.g., interphase drag, heat transfer, and mass transfer terms). These methods have been widely implemented in CFD codes, including: Fluent[®], COMSOL[®], Multiphase Flow with Interphase eXchanges (MFIx) [2] and OpenFOAM [3], and used to model complex systems [4–8].

Discrete phase models (DPMs), also known as Lagrangian-Lagrangian models, model all phases as discrete particles, such as in the discrete element method (DEM) [9]. These methods solve Newton’s equations of motion for each individual particle. Contrary to the CPMs, DPMs are well suited for solid-solid flows due to their accurate physical representation, while fluid-solid flows must be handled carefully to ensure

the fluid-phase particles are sufficiently small to accurately represent the continuum transport phenomena. DPMs have also been widely implemented in CFD codes, including: Fluent[®], Barracuda[®], and OpenFOAM.

Hybrid continuous and discrete mixture phase models couple the transport phenomena between continuous phases (CPMs) and discrete particles (DPMs). These methods best physically represent gas-solid flows; however, because of the complex coupling and numerical methods, these models can be unstable and computationally intensive. These methods are still in early research and development [10–13], but could be excellent candidates for gas-solid flows once fully verified and validated methods have been developed.

Each of these modeling frameworks are highly dependent on the simulation resolution. High-resolution models, such as direct numerical simulation, can accurately model these systems, but are limited to very small time and length scales. Medium-resolution models employ simplifying assumptions, such as modeling the fluidized solid phases as a continua (multi-fluid model) or solid phase clustering (discrete element method), and are capable of modeling systems of laboratory-scale and some full-scale; however, full-scale models are typically computationally intractable, especially in three-dimensions. Low-resolution models can make use of subgrid models to approximate the unresolved physics using constitutive relations. While these assumptions reduce the ability to predict fine-scale behavior, they can sufficiently predict bulk flow behavior of full-scale simulations at a small fraction of the computation time [14–18].

1.2 Subgrid Methods

Subgrid models were originally developed to simplify and speed up turbulent flow calculations [19]. Smagorinsky was attempting to model single-phase turbulent flow

for meteorological applications. It was obvious that resolving the intricacies of turbulence was not possible for such large length scales. Smagorinsky proposed a solution: use a low-pass filter to smooth out the physics and model the unresolved turbulence explicitly through an effective viscosity term. This would allow the calculation of large-scale systems while still providing sufficiently accurate results.

To develop the effective stress term, Smagorinsky used small, periodic domains to simulate the average flow occurring anywhere in a large system. Because the periodic domain is small, a fine grid could be used to resolve the details of the turbulent flow while remaining computationally tractable. Using the small domain, several simulations were carried out with varying flow field properties. From these an effective viscosity model was developed that related the microscopic stress to a function of the grid-cell volume and the filtered stress. This model is known as the Smagorinsky-Lilly model.

This filtering process was first introduced in large eddy simulation (LES) methods and has been used extensively to calculate effective single-phase turbulent flow behavior with coarse-grid simulation [19]. This field is continually under active research trying to develop more accurate and efficient models/methods [16, 20, 21]. More recently these methods were extended to consider gas-solid multiphase flows with a focus on interphase drag by Igci et al. [16–18]. Igci et al. used a similar filtering process to investigate the chaotic nature of gas-particle flows in risers¹. In such a system, a grid size of approximately 10 times the solid particle diameter is typically required to resolve the hydrodynamics. In a riser that spans several meters tall this results in a mesh of millions of cells. Igci et al. used small, periodic domain simulations to simulate the flow in a riser and developed an effective gas-particle drag term. Sarkar et al. [14, 15] extended the Igci drag model by considering multiphase flow with immersed horizontal cylinders. A small periodic domain with immersed

¹A tall, narrow, vertical tube reactor; often used in petroleum refining. [22, 23]

cylinders was used to develop an effective cylinder drag model. Agrawal et al. also extended the Igci model by considering simple gas-particle interphase heat transfer. Using the same filtering methods, Agrawal et al. [24] derived a subgrid model for effective gas-particle heat transfer. The Igci and Sarkar models have been implemented in the open source CFD code, MFIX and undergone verification and validation, showing excellent results. The Agrawal model has not yet been implemented.

The framework for developing all of the aforementioned models is identical:

- 1) Construct a high-resolution sub-system from the full-scale system. This must be done carefully such that it minimizes computational time but still represents the average flow behavior of the full-scale system. This is usually achieved by using periodic domains; however, it can be done with larger systems and applying a filter over varying regions.
- 2) Simulate the sub-system many times with varying flow and geometry conditions, e.g., solid phase fractions, flow velocities, and cylinder diameter and spacing. These flow and geometry conditions will be the input variables to your model, so it is important to know how the system behaves under all possible conditions. Design of experiments methods [25, 26] can optimize the number of simulations and parameter values to be simulated.
- 3) Calculate filtered quantity of interest. This quantity must be derived for each problem by filtering the governing equations.
- 4) Construct model by regressing the quantity of interest to the predictor variables—the flow and geometry conditions. Using parametric non-linear regression methods, an algebraic constitutive relation can be developed.
- 5) Implement the subgrid model within a CFD package and perform verification and validation experiments. Depending on the CFD code, implementation can be as simple as a user-defined function or can require the modification of the source code. Verifying and validating the model is the most important step as it gives insight to the accuracy and uncertainty in the newly developed model.

1.3 Upscaling & Uncertainty Quantification

It is important to note that due to the nature of filtering in subgrid models, information is being sacrificed for computation speed. Because of this loss of information, it is critical to quantify the uncertainties associated with the model to determine the accuracy of the predictions. This is known as uncertainty quantification (UQ). When combined with upscaling techniques, UQ should be applied at each length scale. This ensures accurate propagation of error through upscaling and gives confidence levels for all predictions.

Statistical UQ techniques, such as sensitivity analysis and Bayesian calibration, can help quantify uncertainties in the system and make out-of-sample output predictions [27–30]. A sensitivity analysis quantifies the variation in output that is directly related to the uncertainty and variation in the model input parameters. This can identify important (and unimportant) model parameters, allowing for improved control and simplification of the model being assessed. Additionally, Bayesian calibration methods [31] can be implemented with statistical response surface models (emulators) that are capable of quickly approximating the system. Bayesian calibration uses Markov chain Monte Carlo methods to determine the optimal model parameter values (i.e., values that could have plausibly reproduced the experiment).

1.4 Applications

This work was done in collaboration with the Department of Energy as part of their Carbon Capture Simulation Initiative (CCSI). The goal of CCSI is to develop a computational tool set to expedite the research and development of new carbon capture technologies. These tools could then be used to design efficient carbon capture reactors, capable of reducing the rate of carbon dioxide (CO_2) emissions from combustion power plants.

The system of interest is a post-combustion, multiphase carbon capture reactor, featuring a solid-sorbent particulate bed that is fluidized with post-combustion, CO₂ rich, flue gas. As the flue gas passes through the bed, the CO₂ is adsorbed onto the sorbent particle's surface and the clean gas is passed onto further processes. The adsorption process is exothermic, releasing heat into the system. To prevent overheating and degradation of the sorbent material, cooling heat transfer cylinders are immersed in the flow to regulate temperatures. To maximize the CO₂ capture rate we wish to optimize the operating conditions of the reactor through simulations. As a result, a subgrid model was developed for gas-particle flows around heated/cooled horizontal cylinders. However, the framework is presented such that it can be applied to a variety of problems/systems. The subgrid model was used to simulate a 1 MW solid-sorbent carbon capture reactor as an intermediate step in upscaling from decoupled-physics unit problems to a full-scale 650 MW reactor for VVUQ purposes.

1.5 Dissertation Structure

This dissertation is broken into six chapters: Chapter 2 details the numerical methods employed by MFIX. Chapter 3 describes a framework for upscaling and VVUQ of large-scale systems. The framework is applied to unit problems examining gas-particle hydrodynamics and heat transfer from immersed geometry. The subgrid model development framework, including the derivation, implementation, verification, validation, and uncertainty quantification are detailed in Chapter 4. Chapter 5 briefly compares the results of a 1 MW pilot-scale carbon-capture system using the developed subgrid model versus an alternative coarse-grid approach. Conclusions and future work are summarized in Chapter 6.

Chapter 2

Numerical Methods

Throughout this work the Department of Energy’s open source CFD code, Multiphase Flow with Interphase eXchanges (MFIx) [2] was used to simulate all systems considered. Many other CFD software packages and codes are capable of simulating multiphase flow, such as ANSYS Fluent[®], Barracuda[®], and OpenFOAM[®]; however, MFIx was chosen for this work because it has been developed explicitly for solving multiphase systems and is open source. The ability to view and modify the source code, makes MFIx ideal for our research purposes. Additionally, MFIx has been used to simulate numerous multiphase and multiphysics systems (e.g., circulating and bubbling fluidized beds, combustion reactors, and chemical vapor depositors) [32–36] and is continuously going through systematic verification and validation (V&V).

MFIx is capable of simulating multiphase flow using CPMs (MFIx-TFM) or DPMs (MFIx-DEM or MFIx-MPPIC). Both modeling frameworks have been used to successfully simulate fluidized beds [32, 37, 38]. DPMs more closely simulate the physics of granular systems due to the discrete particles. As such, a DPM approach was previously considered for the carbon capture system modeling of CCSI [39]. However, due to numerical stability issues and the computational expense of the DPM, it was decided the CPM was more appropriate for our applications. A summary of the equations used by MFIx-TFM for solving non-reacting, two-phase flow can be found below. For a complete description of the equations implemented in MFIx, see Benyahia et al. [2].

2.1 Governing Equations

The governing equations for the TFM are similar to those used in single-phase flow, with a few important differences. To account for the fraction of each phase present in a given location, a volume fraction variable is included in each term, and coupled by an additional continuity equation. The momentum and energy equations are further coupled by interphase transport terms that allow the transfer of momentum and energy between the phases. These terms are described in detail below.

The continuity equations are written as

$$\frac{\partial}{\partial t}(\phi_g \rho_g) + \nabla \cdot (\phi_g \rho_g \mathbf{v}_g) = 0 \quad (2.1)$$

$$\frac{\partial}{\partial t}(\phi_s \rho_s) + \nabla \cdot (\phi_s \rho_s \mathbf{v}_s) = 0 \quad (2.2)$$

$$\phi_g + \phi_s = 1, \quad (2.3)$$

where ϕ is phase fraction, ρ is density, \mathbf{v} is velocity, and subscripts g and s denote the gas and solid phases, respectively. The momentum equations are written as

$$\frac{\partial}{\partial t}(\phi_g \rho_g \mathbf{v}_g) + \nabla \cdot (\phi_g \rho_g \mathbf{v}_g \mathbf{v}_g) = -\nabla \cdot \boldsymbol{\tau}_g - \phi_g \nabla p + \phi_g \rho_g \mathbf{g} - I_{gs} \quad (2.4)$$

$$\frac{\partial}{\partial t}(\phi_s \rho_s \mathbf{v}_s) + \nabla \cdot (\phi_s \rho_s \mathbf{v}_s \mathbf{v}_s) = -\nabla \cdot \boldsymbol{\tau}_s - \phi_s \nabla p + \phi_s \rho_s \mathbf{g} + I_{gs}, \quad (2.5)$$

where $\boldsymbol{\tau}$ is stress, p is pressure, \mathbf{g} is gravitational acceleration, and I_{gs} is the interphase momentum transfer. And the energy equations are written as

$$\frac{\partial}{\partial t}(\phi_g \rho_g C_{p,g} T_g) + \nabla \cdot (\phi_g \rho_g C_{p,g} \mathbf{v}_g T_g) = \nabla \cdot (\phi_g k_g \nabla T_g) - H_{gs} \quad (2.6)$$

$$\frac{\partial}{\partial t}(\phi_s \rho_s C_{p,s} T_s) + \nabla \cdot (\phi_s \rho_s C_{p,s} \mathbf{v}_s T_s) = \nabla \cdot (\phi_s k_s \nabla T_s) + H_{gs}, \quad (2.7)$$

where T is temperature, C_p is specific heat capacity, k is thermal conductivity, and

H_{gs} is the interphase heat transfer.

Solving the momentum governing equations in the TFM requires appropriate closure relations to calculate the solids properties (e.g., viscosity and pressure). The Kinetic Theory of Granular Flow provides necessary closures by quantifying the energy in the solid-phase through an additional governing equation. This energy is proportional to the mean square of the solid-phase velocity and is referred to as the granular temperature (GT). The full partial differential equation for GT is written as

$$\frac{3}{2} \left[\frac{\partial}{\partial t} (\phi_s \rho_s \Theta) + \nabla \cdot (\phi_s \rho_s \Theta) \mathbf{v}_s \right] = \boldsymbol{\tau}_s : \nabla \mathbf{v}_s - \nabla \cdot \bar{q}_\Theta - \gamma_\Theta + \Pi, \quad (2.8)$$

where Θ is granular temperature, \bar{q}_Θ is diffusive flux of granular energy, γ_Θ is granular energy dissipation, and Π is interphase exchange of granular energy [40]. Because solving the full GT partial differential equation can be computationally demanding, Syamlal [41] proposed an algebraic expression for GT that neglects convection and diffusion terms and retains the generation and dissipation terms [40]. The algebraic expression for GT is

$$\Theta = \left\{ \frac{-K_1 \phi_s \text{tr}(\mathbf{D}_s) + \sqrt{K_1^2 \text{tr}(\mathbf{D}_s) \phi_s^2 + 4K_4 \phi_s [K_2 \text{tr}(\mathbf{D}_s)^2 + 2K_3 \text{tr}(\mathbf{D}_s^2)]}}{2\phi_s K_4} \right\}^2 \quad (2.9)$$

$$K_1 = 2(1 + e_{ss})\rho_s g_0 \quad (2.10)$$

$$K_2 = \frac{4d_s \rho_s (1 + e_{ss}) \phi_s g_0}{e\sqrt{\pi}} - \frac{2}{3} K_3 \quad (2.11)$$

$$K_3 = \frac{d_s \rho_s}{2} \left\{ \frac{\sqrt{\pi}}{3(3 - e_{ss})} \left[\frac{1}{2}(1 + 3e_{ss}) + 0.4(1 + e_{ss})(3e_{ss} - 1)\phi_s g_0 \right] + \frac{8\phi_s g_0(1 + e_{ss})}{5\sqrt{\pi}} \right\} \quad (2.12)$$

$$K_4 = \frac{12(1 - e_{ss}^2)\rho_s g_0}{d_s \sqrt{\pi}}, \quad (2.13)$$

where K_{1-4} are granular stress constants, e_{ss} is the coefficient of restitution for solid-

solid interactions, g_0 is the radial distribution function at contact, e is the coefficient of restitution for solid-wall interactions, and d_s is the diameter of solid-phase particles.

The GT is then used to calculate the solids viscosity and pressure, which are used to calculate the gas- and solid-phase stress tensors.

$$\boldsymbol{\tau}_g = 2\mu_{gt} \left\{ \frac{1}{2} [\nabla \mathbf{v}_g + (\nabla \mathbf{v}_g)^T] - \frac{1}{3} \nabla \cdot \mathbf{v}_g \mathbf{I} \right\} \quad (2.14)$$

$$\boldsymbol{\tau}_s = (-P_s + \eta\mu_b \nabla \cdot \mathbf{v}_s) \mathbf{I} + 2\mu_s \left\{ \mathbf{D}_s - \frac{1}{3} \nabla \cdot \mathbf{v}_s \mathbf{I} \right\} \quad (2.15)$$

$$\mathbf{D}_s = \frac{1}{2} [\nabla \mathbf{v}_s + (\nabla \mathbf{v}_s)^T], \quad (2.16)$$

where μ_{gt} is turbulent viscosity, \mathbf{I} is the unit tensor, P_s is solids pressure, η is a function of the coefficient of restitution, μ_s is solids viscosity, and \mathbf{D}_s is rate of strain.

2.2 Interphase Momentum Exchange

The interphase momentum exchange term consists of a drag model (β) and difference of velocities between the phases

$$I_{gs} = \beta(\mathbf{v}_g - \mathbf{v}_s). \quad (2.17)$$

The drag model is a correlation that is developed through empirical studies and quantifies the interaction between the two phases. Many correlations have been proposed, for example, Wen-Yu [42, 43], Gidaspow [43], Syamlal-O'Brien [43, 44], Koch-Hill [45, 46], BVK [47], and HYS [48]. This work primarily uses the Wen-Yu correlation, but also considered the Gidaspow and Syamlal-O'Brien correlations for a comparison study.

The Wen-Yu model is the simplest of the three models [2]

$$\beta = \frac{3}{4} \frac{\rho_g \phi_g \phi_s}{d_s} C_D |\mathbf{v}_g - \mathbf{v}_s| \phi_g^{-2.65} \quad (2.18)$$

$$C_D = \begin{cases} \frac{24}{\phi_g \text{Re}_s} [1 + 0.15(\phi_g \text{Re}_s)^{0.687}] & \text{Re}_s < 1000 \\ 0.44 & \text{Re}_s \geq 1000, \end{cases} \quad (2.19)$$

where Re_s is Reynolds number based on slip velocity and solid-phase particle diameter. The Gidaspow model is a combination of the Ergun [49] and Wen-Yu models. Here, the drag model is piecewise and is driven by the flow regime of the system, i.e., dense versus dilute flow [2],

$$\beta = \begin{cases} \frac{3}{4} \frac{\rho_g \phi_g \phi_s}{d_s} C_D |\mathbf{v}_g - \mathbf{v}_s| \phi_g^{-2.65} & \phi_g < 0.8 \\ 150 \frac{\phi_s^2 \mu_g}{\phi_g d_s^2} + 1.75 \frac{\phi_s \rho_g}{d_s} |\mathbf{v}_g - \mathbf{v}_s| & \phi_g \geq 0.8 \end{cases} \quad (2.20)$$

$$C_D = \begin{cases} \frac{24}{\phi_g \text{Re}_s} [1 + 0.15(\phi_g \text{Re}_s)^{0.687}] & \text{Re}_s < 1000 \\ 0.44 & \text{Re}_s \geq 1000. \end{cases} \quad (2.21)$$

The Syamlal-O'Brien [2, 44] model is the most complicated of the three. It is loosely based on the Wen-Yu model; however, it uses a modified drag coefficient and additional supporting equations. Furthermore, the drag model must be iterated to determine the values of the model coefficients, B - D , which go into the calculation of β via U_r [2],

$$\beta = \frac{3}{4} \frac{\rho_g \phi_g \phi_s}{U_r^2 d_s} C_D |\mathbf{v}_g - \mathbf{v}_s| \quad (2.22)$$

$$C_D = \left(0.63 + 4.8 \sqrt{\frac{U_r}{\text{Re}_s}} \right)^2 \quad (2.23)$$

$$A = \phi_g^{4.41} \quad (2.24)$$

$$B = \begin{cases} C\phi_g^{1.28} & \phi_g < 0.85 \\ \phi_g^D & \phi_g \geq 0.85 \end{cases} \quad (2.25)$$

$$D = 1.28 + \frac{\log(C)}{\log(0.85)}, \quad (2.26)$$

where U_r is the ratio of terminal settling velocity of a multi-particle system to that of a single particle. The iterative process minimizes the difference between the theoretical and experimental minimum fluidization velocities (i.e., $|U_{mf}^{th} - U_{mf}^{exp}| \rightarrow 0$, where U_{mf}^{th} and U_{mf}^{exp} are theoretical and experimental minimum fluidization velocities, respectively).

For each simulation utilizing the Syamlal-O'Brien drag model, the model coefficients are calculated and set based on the physical properties of the system. The coefficients are not further adjusted to change the fluidization behavior of the system.

2.3 Interphase Energy Exchange

Interphase energy exchange is calculated in an analogous manner to interphase momentum exchange by using a simple convection-type model

$$H_{gs} = \gamma_{gs}(T_s - T_g), \quad (2.27)$$

where γ_{gs} is the interphase heat transfer coefficient, which can be related to the interphase Nusselt number via

$$\gamma_{gs} = \frac{6k_g\phi_s\text{Nu}_{gs}}{d_p^2}, \quad (2.28)$$

where Nu_{gs} is the interphase Nusselt number. There exist several different correlations to calculate the interphase Nusselt number [50–52]. MFIX employs the Gunn

correlation [50] which takes the form

$$\begin{aligned} \text{Nu}_{gs} = & (7 - 10\phi_g + 5\phi_g^2) \left(1 + 0.7\text{Re}_g^{0.2}\text{Pr}_g^{1/3}\right) \\ & + (1.33 - 2.4\phi_g + 1.2\phi_g^2) \text{Re}_g^{0.7}\text{Pr}_g^{1/3}, \end{aligned} \quad (2.29)$$

where Pr_g is the Prandtl number for the gas phase, given by

$$\text{Pr}_g = \frac{C_{p,g}\mu_g}{k_g}. \quad (2.30)$$

Chapter 3

VVUQ Framework for Upscaling CFD

Simulating full-scale systems with CFD methods is usually computationally intractable. Resolving complex multiphysics spanning several orders of magnitude in length-scales requires supercomputers with extensive run-times. One alternative approach to such problems is to separate the length scales and decouple the physics. This reduces the system to sub-systems that can easily be simulated to give insight into the building blocks of the system. These decoupled sub-systems can then be combined and up-scaled to intermediate laboratory-scales to create small-scale representations of the full-scale system. As the complexity and scales are increased, the error in the predictions can be propagated through the upscaling to give an idea of the total uncertainty at each scale. To best quantify these errors and uncertainties, intermediate systems should be compared with experimental setups. This process is referred to as a VVUQ hierarchy.

The system of interest, a full-scale (650 MW), solid-sorbent, carbon capture reactor, is too large to simulate using traditional CFD methods. Instead, we apply a VVUQ hierarchy and the problem is broken down into several intermediate scales (pilot- and laboratory-scales) and the physics are decoupled. This reduces the problem to the fundamental building blocks (unit problems) of the full-scale reactor: hydrodynamics of a bubbling fluidized bed, heat transfer, reaction kinetics, and hydrodynamics of a moving fluidized bed (Figure 3.1) [53]. This hierarchical road map provides a clear path to simulating the full-scale system, starting with the basic unit

problems, then upscaling, incorporating multiphysics, and further upscaling. At each upscaling phase, VVUQ methods are applied to quantify the error for the associated sub-systems. This error is then propagated through to the next level.

In this chapter we begin the VVUQ upscaling process and consider the first two unit problems: the hydrodynamics and heat transfer of a bubbling fluidized bed with immersed heat transfer cylinders. These unit problems will provide the necessary data (i.e., errors and uncertainties) for upscaling to a laboratory-scale CO₂ adsorber reactor (Figure 3.1).

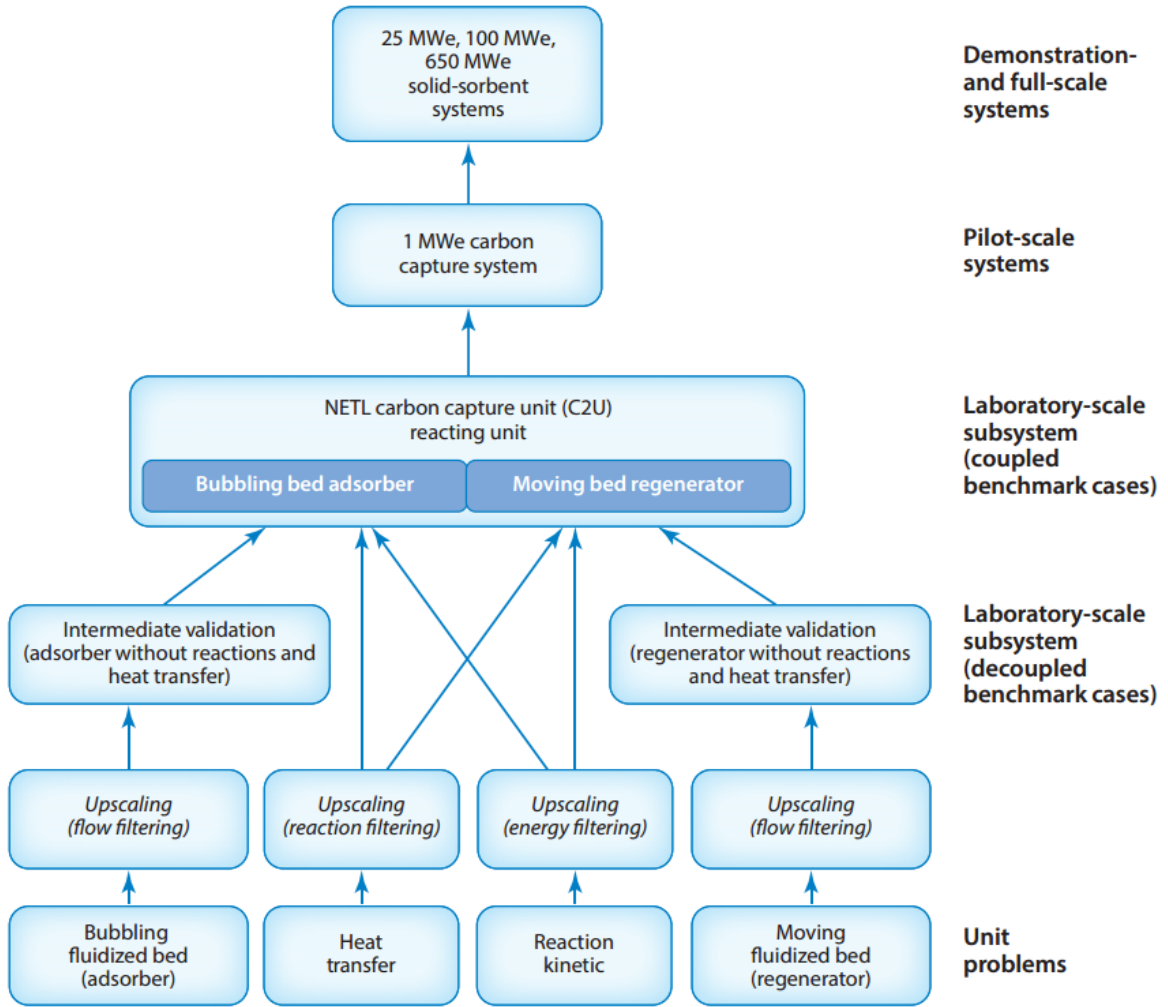


Figure 3.1: CCSI validation hierarchy [53]. The full scale model is broken into smaller, simplified unit problems with decoupled physics.

3.1 Gas-Particle Hydrodynamics

The first unit problem consists of validating the hydrodynamics of gas-particle flow around immersed geometry. There are many reports of experimental results for such systems [54–58]; however, each publication has different foci (e.g., bubble characteristics, tracer concentration, mixing times, solids hold up, and pressure drops). For the validation of the hydrodynamics, we use the experimental work of Kim et al. [58], who investigated the effects of immersed horizontal tubes in a bubbling bed by observing bubble frequency, phase fraction, and contacting time. This case was chosen because the domain was sufficiently small to run many simulations, they provided several different validation quantities, and the setup, methods, and results were all reported in detail (and with quantified errors).

As demonstrated in Chapter 2, approximating a granular material as a liquid with the TFM requires additional mathematical models, such as drag, granular temperature, and friction. These models have been developed based on empirical and theoretical constitutive relations. Consequently, results can vary significantly depending on the choice of models used. Furthermore, physical quantities, such as coefficients of restitution, friction angle, and packed bed void fraction, can be difficult to measure experimentally and are often chosen based on previous studies or without rationalization. Because there is no single correct choice for the aforementioned models and quantities, there exists an associated uncertainty for each choice. These uncertainties must be quantified and propagated through each scale of the VVUQ hierarchy to ensure integrity of the large-scale predictions.

Statistical UQ techniques, such as sensitivity analysis and Bayesian calibration, can help quantify uncertainties in the system and make out-of-sample output predictions [27–30]. A sensitivity analysis quantifies the variation in output that is directly related to the uncertainty and variation in the model input parameters. This

can identify important (and unimportant) model parameters, allowing for improved control and simplification of the model being assessed. Additionally, Bayesian calibration methods [31] can be implemented with statistical response surface models (emulators) that are capable of quickly approximating the system. Bayesian calibration uses Markov chain Monte Carlo methods to determine the optimal model parameter values (i.e., values that could have plausibly reproduced the experimental results). These approaches are used in this study and are discussed in further detail in Section 3.1.2.

3.1.1 Setup

Kim et al.’s [58] experimental setup measured $34 \times 48 \times 60$ cm with 25 horizontal 2.54 cm diameter tubes. As seen in Figure 3-2a, the tubes were arranged in a triangular configuration with horizontal spacing of 8 cm, vertical spacing of 7 cm, pitch spacing of 8 cm, and positioned 10 cm above the distributor plate (measured to the center of the bottom tubes). The central tube, marked “Probe” in Figure 3-2a, contained optical sensors and thermocouples spaced 45° apart, clockwise from $+90^\circ$ (top surface) to -90° (bottom surface), as shown in Figure 3-2b. Ambient air and sand (silicon dioxide, SiO_2) were used as the gas and solid phases, respectively. The experimental parameters are tabulated in Table 3.1.

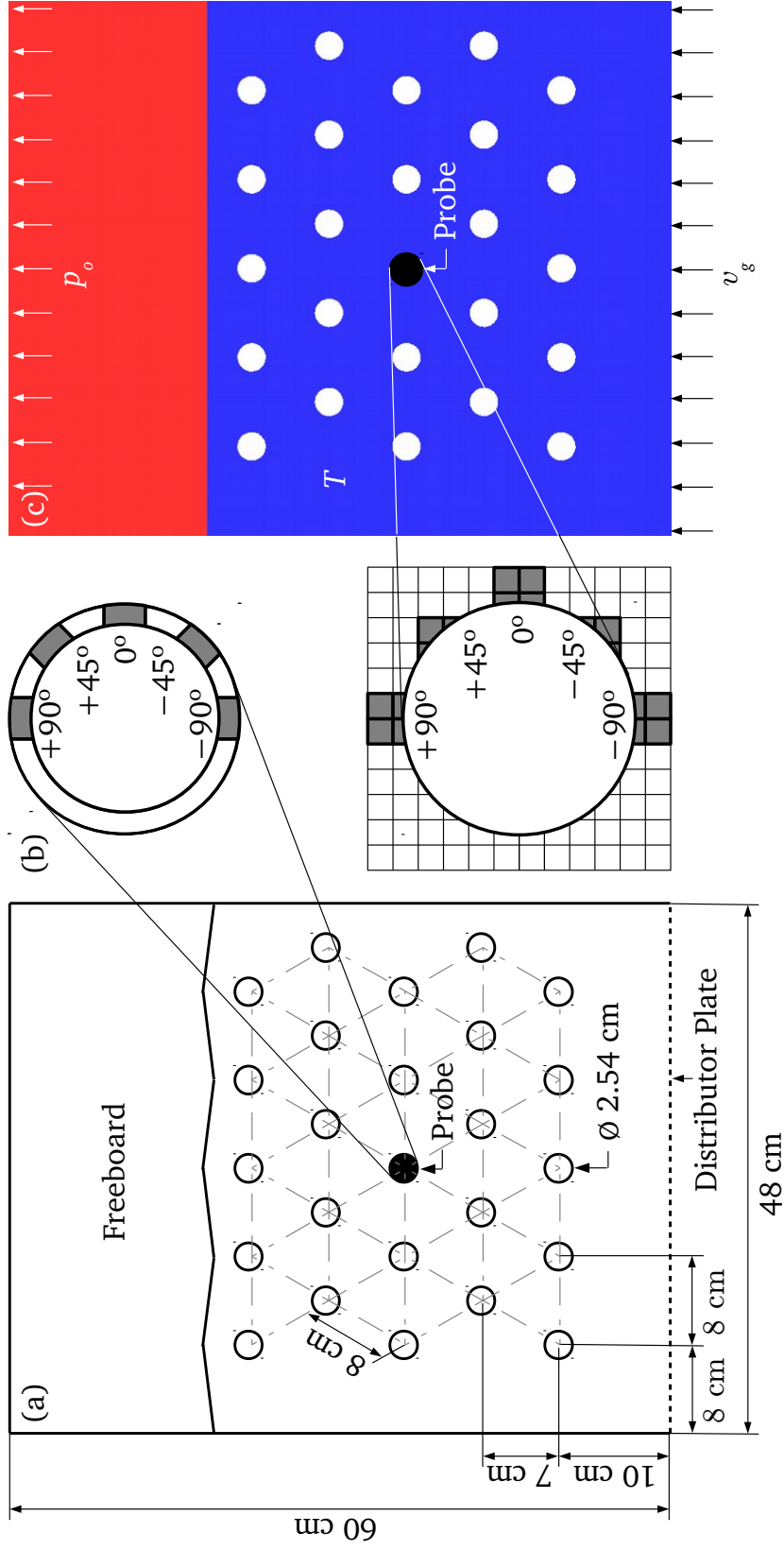


Figure 3-2: Bubbling fluidized bed domains and probes: (a) system schematic; (b) experimental probe with optical and thermal sensors (top) [58], MFIX probe and measurement cells (bottom); and (c) MFIX simulation, where v_g is the gas phase velocity inflow, T is the bulk temperature, and p_o is the pressure outflow.

Table 3.1: Experimental parameters and physical properties.

Parameter	Value	Parameter	Value
Bed		Tube Bank	
Width (cm)	48	Number of tubes	25
Height (cm)	60	Diameter (cm)	2.54
Depth (cm)	34	Spacing, horz. (cm)	8
Bed height (cm)	42	Spacing, vert. (cm)	7
Pressure (kPa)	101.3	Pitch (cm)	8
Gas Phase		Solid Phase	
Density (g/cm ³)	1.2·10 ⁻³	Diameter (μm)	240
Viscosity (Pa·s)	1.8·10 ⁻⁵	Density (g/cm ³)	2.582
Min. fluidization velocity (cm/s)	4.8		

Experimental hydrodynamics data were collected at four gas velocities: $v_g = \{5.5, 7.0, 11.0, 12.6\}$ cm/s. Bubble frequency (frequency at which bubbles passed by the probe sensors) and bubble contacting time (root-square-average of time that bubbles were in contact with the probe sensors) were measured for all gas velocities, while bubble phase fraction (ratio of time bubbles were in contact with the probe sensors) was only measured for the gas velocity of $v_g = 12.6$ cm/s. Data from the optical sensors were recorded for 28 seconds at a sampling frequency of 500 Hz. Kim et al.'s calculation methods for these quantities are detailed in [58].

A two-dimensional (2D) Eulerian CFD model was developed using the MFIX code. This 2D model neglects the 34 cm depth of the experimental setup [58], and represents a slice through the middle of the domain. The use of a 2D simulation model for this domain was studied by Li et al. [32] and was shown to provide reasonable predictions of bubble dynamics. The simplified MFIX domain can be seen in Figure 3-2c. The

vertical sidewalls were treated with no-slip boundary conditions, while the base and top had fixed velocity inflow and pressure outflow boundary conditions. Based on a previous study by Li et al. [32], the domain was discretized into approximately 39,000 cells (cell size $\Delta_x = \Delta_y = 2.7 \text{ mm} \approx 10 d_p$) and the system was simulated for 60 seconds, of which the last 30 seconds were analyzed. Measurements were extracted from MFIX simulations by defining simulation cells that coincided with the experimental optical sensor locations (Figure 3.2b).

Kim et al. [58] studied the hydrodynamics of bubble behavior through bubble frequency, phase fraction, and contacting time. These output variables were calculated from the optical sensor data. Similarly, gas-fraction measurements from the MFIX simulations were used to calculate the simulated bubble frequency and phase fraction by

$$f_b = \frac{N_b}{t_s} \quad \delta_b = \frac{t_{bc}}{t_s}, \quad (3.1)$$

where f_b is bubble frequency, δ_b is bubble phase fraction, N_b is total number of bubbles observed at the sensor, t_s is total sampling time, and t_{bc} is total contacting time [58]. Converting void fraction to bubbles requires a threshold value to differentiate bubbles from emulsion. Studies by Li et al. [32, 59] used void fraction values of 0.7 and 0.8 for bubble thresholds and showed best agreement with literature data using 0.8. As a result, a bubble threshold of 0.8 was used throughout this study. Additionally, bubbles needed to be differentiated from an instantaneous void. This was accomplished by defining a bubble to be a void fraction that remained above the bubble threshold for two consecutive sampling time steps,

$$t_{bc_{min}} = 2 \frac{1}{F_s}, \quad (3.2)$$

where $t_{bc_{min}}$ is minimum contact time for classification as a bubble and F_s is sampling

rate (100 Hz in this study).

3.1.2 Statistical Analysis

The MFIX CFD model was analyzed with statistical UQ techniques, including sensitivity analysis and Bayesian calibration. These tools were used to evaluate the model, determine the optimal model input parameters and predict outputs with associated uncertainties.

Parameter Selection and Statistics

Analysis began by identifying CFD model input parameters $\bar{\theta} = (\theta_1, \theta_2, \dots, \theta_n)$ that were thought to be important and had an associated uncertainty in their values. Six model parameters were chosen for this study: $\theta_{1,2}$ = coefficients of restitution for solid-solid and solid-wall interactions, respectively; θ_3 = packed bed void fraction, $\theta_{4,5}$ = friction angles for solid-solid and solid-wall interactions, respectively; and θ_6 = drag model. A review of the literature of numerical studies on fluidized beds and solicitation of expert advice was used to determine physical ranges and most likely values of these parameters [60–69]; the results are summarized in Table 3.2.

Table 3.2: Model parameters and statistics.

Parameter	Distribution	
Continuous	Range	Mode
$\theta_1 =$ coefficient of restitution, solid-solid (-)	0.8–0.997	0.9
$\theta_2 =$ coefficient of restitution, solid-wall (-)	0.8–0.997	0.9
$\theta_3 =$ packed bed void fraction (-)	0.3–0.4	0.35
$\theta_4 =$ friction angle, solid-solid ($^\circ$)	25.0–45.0	28.5
$\theta_5 =$ friction angle, solid-wall ($^\circ$)	25.0–45.0	28.5
Categorical	Likelihood	
$\theta_6 =$ drag model		
Gidaspow	33.3%	
Syamlal-O’Brien	33.3%	
Wen-Yu	33.3%	

From these values, prior distributions (probability density functions, PDFs) were constructed to approximate the likelihood of values for each parameter. Coefficients of restitution and packed bed void fraction had symmetric distributions and were assigned shifted and scaled β -distributions centered at their respective modes. Friction angles had asymmetric distributions and were also assigned shifted and scaled β -distributions that matched their respective modes. The drag models were treated as categorical variables and were weighted equally with a discrete uniform distribution. The prior distributions are shown by the dashed lines in Figure 3-3.

The variables used for the analysis were aligned with the experimental inputs and outputs of Kim et al. [58]. The input parameters were angular position of probe sensors (\bar{y}_1) and gas velocity (\bar{x}_2). The output parameters were bubble frequency (\bar{x}_1) and phase fraction (\bar{y}_2) (Table 3.3).

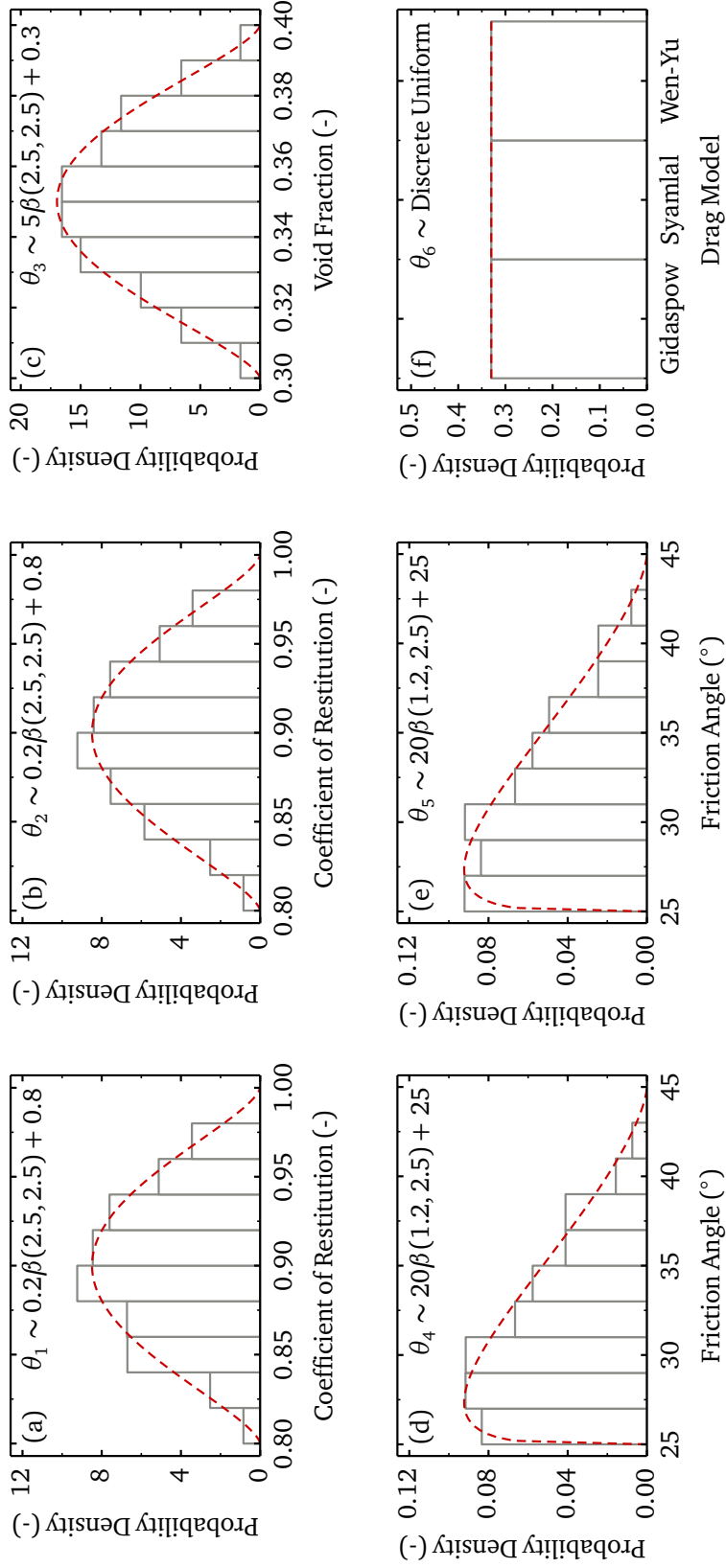


Figure 3-3: Prior distributions of the model parameters used for the sensitivity analysis: (a) coefficient of restitution, solid-solid; (b) coefficient of restitution, solid-wall; (c) packed bed void fraction; (d) friction angle, solid-solid; (e) friction angle, solid-wall; and (f) drag models, where Syamlal is the Syamlal-O'Brien drag model. The dashed lines are prior distributions and the histograms are LHS samples from the prior distributions. The prior distribution equations are listed inside their respective figures.

Table 3.3: Bayesian calibration variables.

Experimental Inputs (\bar{x}_i)	
\bar{x}_1	angular positions ($^\circ$)
\bar{x}_2	gas velocities (cm/s)
Experimental Outputs (\bar{y}_i)	
\bar{y}_1	bubble frequency (bubbles/s), for $\bar{x}_1 \in \{\pm 90, \pm 45, 0\}$, $\bar{x}_2 \in \{5.5, 7.0, 11.0, 12.6\}$
\bar{y}_2	bubble phase fraction (-), for $\bar{x}_1 \in \{\pm 90, \pm 45, 0\}$, $\bar{x}_2 \in \{12.6\}$

Sampling

The joint prior distribution for all 6 parameters was formed by assuming all 6 parameters were independent (i.e., resulting in a product of the marginal prior densities). To design an efficient matrix of simulations, special care was taken to properly sample the prior distributions. Many sampling methods exist (e.g., random, Latin Hypercube, and Monte Carlo); however, the choice is application dependent. Latin Hypercube Sampling (LHS) [70] was used in this study because of its efficiency (versus Monte Carlo sampling) and its ability to guarantee sampling of the entire state space (versus random sampling). The LHS method can be broken down into 3 steps: 1) define the prior distribution (Figure 3.4a), 2) divide the distribution into equal-probability areas (Figure 3.4b), and 3) randomly sample each area (Figure 3.4c). The LHS realizations of the prior distributions are shown by the histograms in Figure 3.3.

Each simulation produced (after post-processing) the \bar{y}_1 and \bar{y}_2 values at angular locations $\{\pm 90.0, \pm 67.5, \pm 45.0, \pm 22.5, 0\}^\circ$ (additional intermediate values were recorded to smooth the data trends). Therefore we had 7 “free parameters” for which to choose values in the LHS, $\{\bar{x}_1, \theta_1, \theta_2, \dots, \theta_6\}$. For the initial analysis, gas velocity

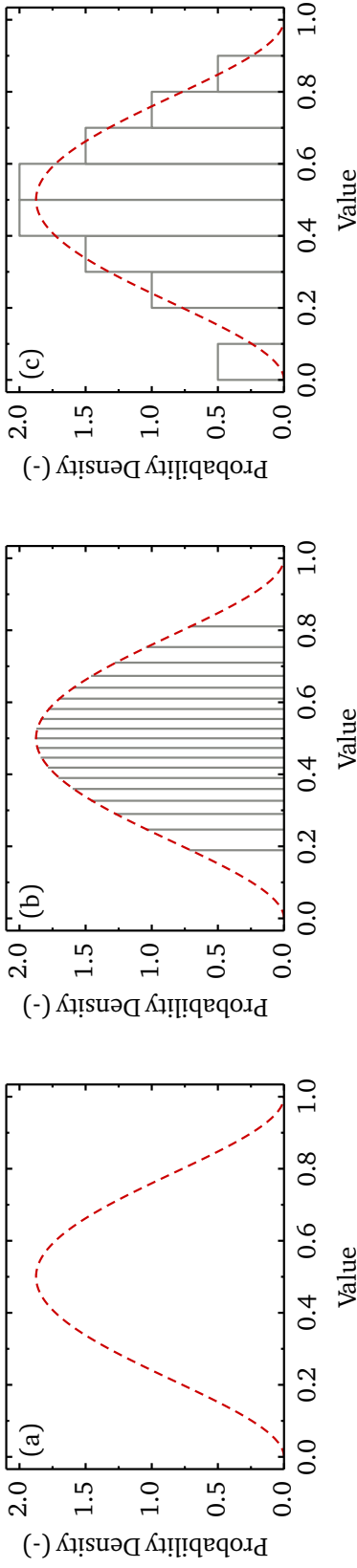


Figure 3-4: Latin Hypercube sampling steps: (a) define the prior distribution, (b) divide the distribution into equal-probability areas, and (c) randomly sample each area.

was restricted to $\bar{x}_2 = 12.6$ cm/s because extra experimental data was available at that velocity. This initial analysis consisted of a LHS of size 60. A subsequent LHS of size 30 was then designed to evaluate the effects of varying the velocity, where $\bar{x}_2 = \{5.5, 7.0, 11.0\}$ cm/s. The additional 30 CFD simulations were distributed evenly across the values of \bar{x}_2 and used the same prior distributions that were used in the initial LHS (Figure 3-3).

Calibration

To explore the state-space of the input parameters, a Bayesian calibration [71] was performed. A brief overview of the calibration methods can be found below; however, the specifics of this approach are provided in Storlie et al. [72]. In this calibration procedure, an emulator (i.e., statistical response surface model) was developed to approximate the behavior of the CFD model. The emulator is designed such that it is computationally efficient, allowing thousands of pseudo simulations (emulations) to be computed quickly. The emulator can then be used to predict the experimental data (\bar{y}_i) as

$$\bar{y}_i = \eta(\bar{x}_i, \bar{\theta}) + \delta(\bar{x}_i) + \epsilon_i, \quad (3.3)$$

where $\eta(\bar{x}_i, \bar{\theta})$ is the emulator, $\delta(\bar{x}_i)$ is the model form discrepancy, and ϵ_i is the measurement error. In principle the CFD model could be used directly for η , but due to the computational expense of running the CFD model, it is replaced with the emulator. In this approach, the emulator and discrepancy terms are modeled with Bayesian Smoothing Spline ANalysis Of VAriance (BSS-ANOVA) models [73], where the BSS-ANOVA model is merely a Gaussian Process (GP) with a special covariance function [72]. Compared to the standard GP, the BSS-ANOVA model increases the ease of handling categorical inputs and correlated outputs, and improves computa-

tional efficiency. It is important to understand that the emulator is not simply a fast surrogate model for the CFD code, it accounts for the additional uncertainty inherent in the estimation of a response surface. To approximate the posterior distribution of the emulator, discrepancy, and model parameters, Markov chain Monte Carlo (MCMC) was used. While many forms of MCMC have been developed (e.g., Gibbs, reversible jump, and Langevin), a hybrid Gibbs, Metropolis-Hastings sampling scheme [74] was chosen and run for 40,000 MCMC iterations (run time of 4 hours). The results of this analysis thus include an emulator capable of predicting output values (bubble frequency and phase fraction) with uncertainty at untested input and model parameter values.

3.1.3 Results

The results from the LHS campaign of simulations can be seen in Figures 3-5 and 3-6, for bubble frequency and phase fraction, respectively. The CFD simulation results of bubble frequency showed three important traits: low bubble frequencies at angular positions $-90^\circ > \bar{x}_1 > 0^\circ$ with a gas velocity of $\bar{x}_2 = 5.5$ cm/s (Figure 3-5a), wide variation of bubble frequencies at angular positions $-90^\circ > \bar{x}_1 > 0^\circ$ with gas velocities $\bar{x}_2 = \{5.5, 7.0\}$ cm/s (Figures 3-5a and 3-5b), and over prediction of bubble frequencies across all gas velocities (Figures 3-5a–3-5d). The smallest gas velocity, $\bar{x}_2 = 5.5$ cm/s, was just slightly larger than the reported minimum fluidization velocity ($U_{mf} = 4.8$ cm/s) [58]. This minimal difference in velocities resulted in poor fluidization of the simulated systems depending on the drag model chosen. Gidaspow and Syamlal-O’Brien models both resulted in poor fluidization for a gas velocity of $\bar{x}_2 = 5.5$ cm/s, while the Wen-Yu model was unaffected. The Syamlal-O’Brien model also resulted in poor fluidization for a gas velocity of $\bar{x}_2 = 7.0$ cm/s, while Wen-Yu and Gidaspow models were unaffected. These fluidization problems are also responsible for the wide variation in results at lower velocities. Over prediction of bubble frequency occurred

at all velocities (of systems that reached fluidization) and is thought to be a result of the simplified simulation domain. Simplifying the system from 3D to 2D eliminated front- and rear-wall effects. Had these effects been present, the additional drag forces would have resulted in slower moving bubbles and an overall lower bubble frequency.

The CFD simulation results of bubble phase fraction showed similar trends compared to the bubble frequency: low bubble phase fraction at angular positions $-90^\circ > \bar{x}_1 > 0^\circ$, with a gas velocity of $\bar{x}_2 = 5.5$ cm/s (Figure 3.6a), wide variation of bubble phase fraction at angular positions $-90^\circ > \bar{x}_1 > 0^\circ$ with gas velocities $\bar{x}_2 = \{5.5, 7.0\}$ cm/s (Figures 3.6a and 3.6b), and under prediction of bubble phase fraction for gas velocities $\bar{x}_2 = 12.6$ cm/s (Figure 3.6d). The low values and wide variation of bubble phase fraction at low gas velocities were also thought to be caused by the poor fluidization of the system. The slower moving bubbles in a full 3D system would remain at the tube surface for longer periods of time, resulting in a higher bubble phase fraction.

The resulting emulator from the calibration procedure was used to perform a global sensitivity analysis [27] of the CFD model (on the bubble frequency output) as in Storlie et al. [75] and Storlie & Helton [76, 77]. The total variance index was calculated for each of the parameters across several values of the input space and is displayed in Figure 3.7. The total variance index values identify which input parameters contribute significantly to the overall fluctuation of the output. It is clear from Figure 3.7 that the parameter importance does not change significantly across input space. In this problem, friction angle for solid-solid interactions and drag model were the two parameters that had the largest effect on bubble frequency. The same results for bubble frequency were also obtained using the Adaptive COmponent Selection and Smoothing Operator (ACOSSO) response surface [75].

The Bayesian calibration resulted in an approximate sample from the posterior

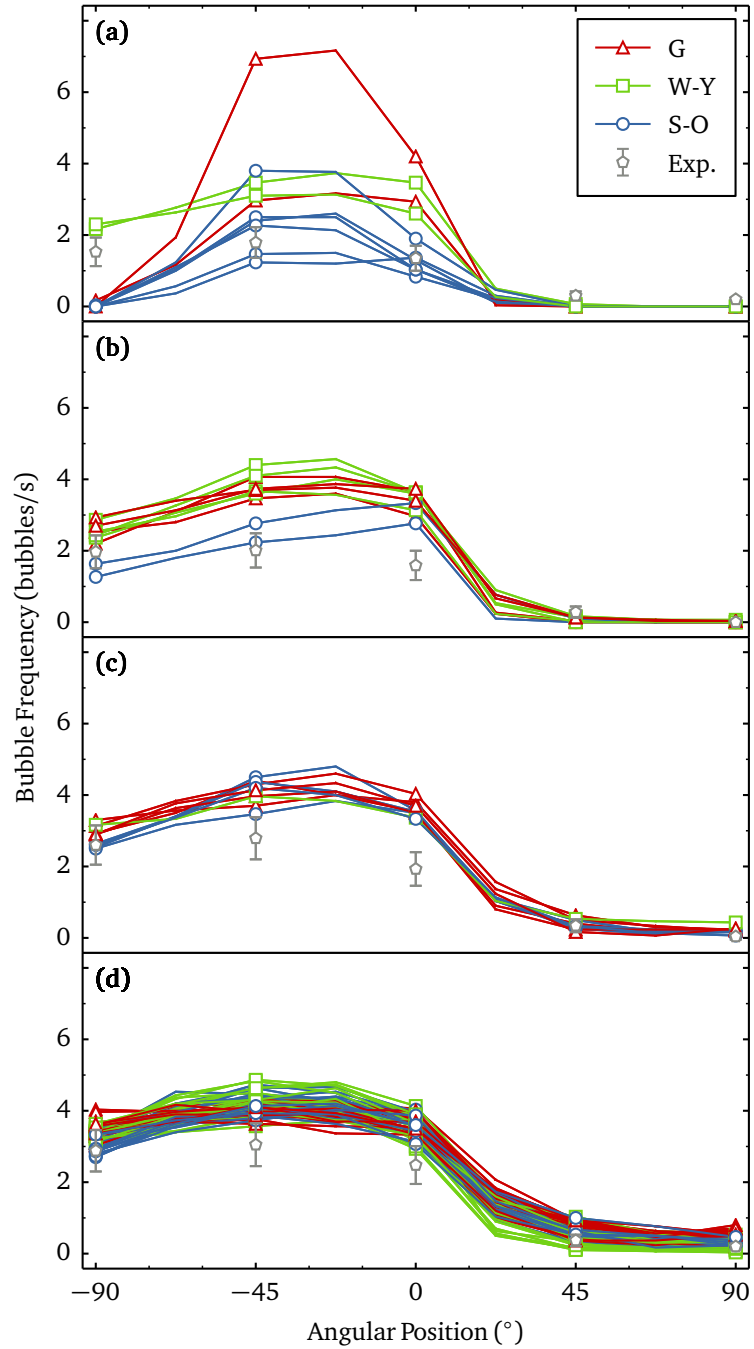


Figure 3-5: Bubble frequency results for 90 simulations using LHS of sizes 60 ($v_g = 12.6$ cm/s) and 30 ($v_g = \{5.5, 7.0, 11.0\}$ cm/s) for gas velocities: (a) $v_g = 5.5$, (b) $v_g = 7.0$, (c) $v_g = 11.0$, and (d) $v_g = 12.6$ cm/s; where G, W-Y, and S-O are Gidaspow, Wen-Yu and Syamlal-O'Brien drag models, respectively, and Exp. is experimental results [58].

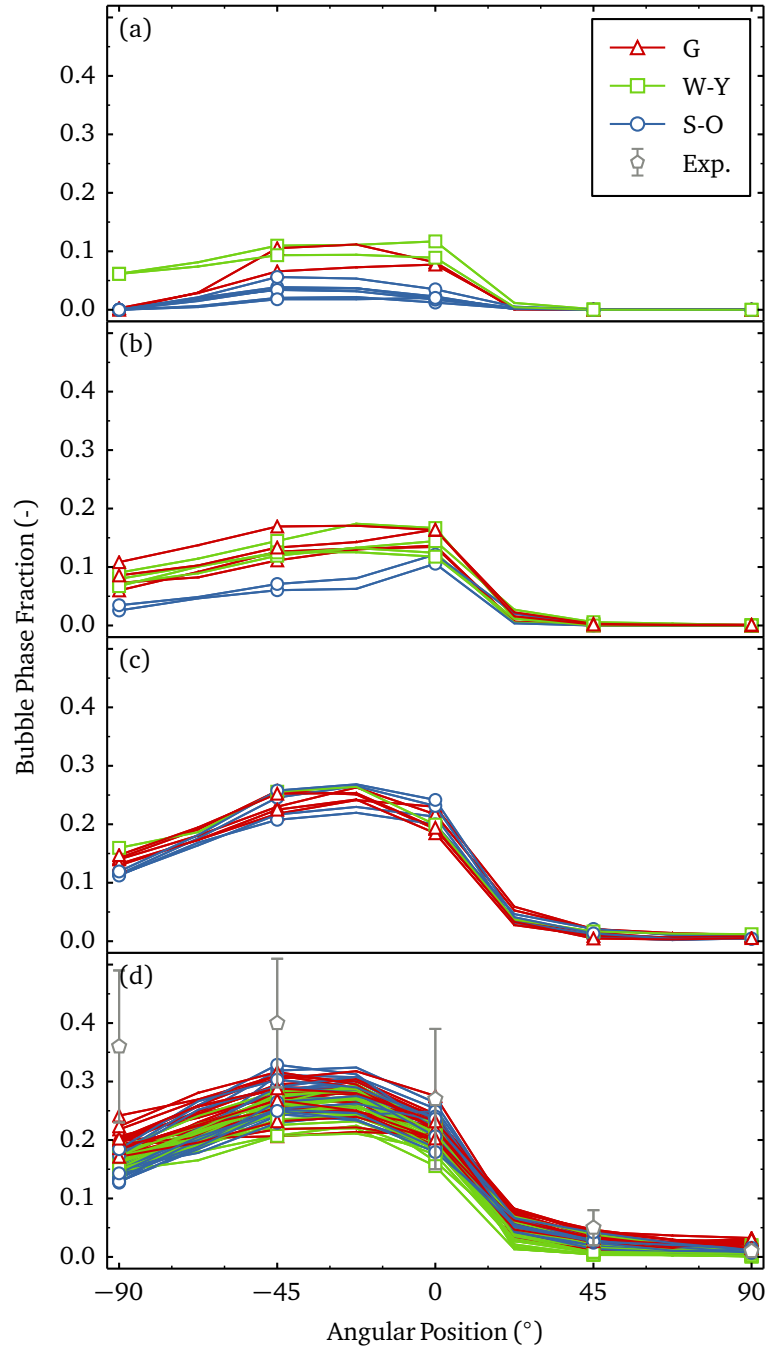


Figure 3-6: Bubble phase fraction results for 90 simulations using LHS of sizes 60 ($v_g = 12.6$ cm/s) and 30 ($v_g = \{5.5, 7.0, 11.0\}$ cm/s) for gas velocities: (a) $v_g = 5.5$, (b) $v_g = 7.0$, (c) $v_g = 11.0$, and (d) $v_g = 12.6$ cm/s; where G, W-Y, and S-O are Gidaspow, Wen-Yu and Syamlal-O'Brien drag models, respectively, and Exp. is experimental results [58].

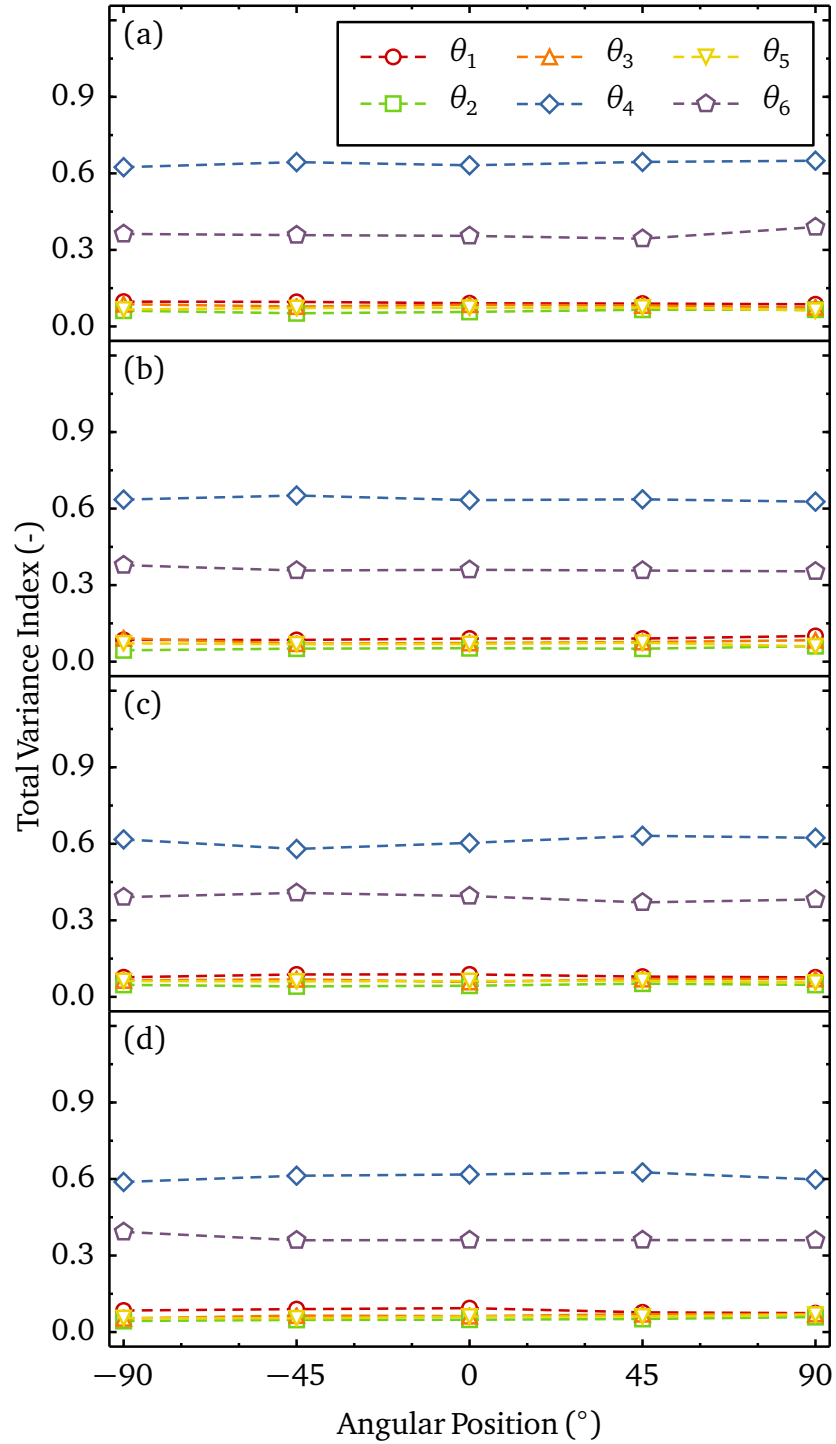


Figure 3.7: Results of sensitivity analysis for bubble frequency across angular location for gas velocities: (a) $v_g = 5.5$, (b) $v_g = 7.0$, (c) $v_g = 11.0$, and (d) $v_g = 12.6$ cm/s.

distribution for the model parameters based on the MCMC simulation. The marginal posterior distributions (i.e., histograms from 20,000 observations from the MCMC approximated posterior sample) can be seen in Figure 3-8 compared with their respective prior distributions (shown as dashed lines). The posterior distributions for the model parameters: coefficients of restitution for solid-solid and solid-wall interactions (Figures 3-8a and 3-8b, respectively); packed bed void fraction (Figure 3-8c); and friction angle for solid-wall interactions (Figure 3-8e) did not change significantly from their prior distributions. This makes intuitive sense in light of the sensitivity analysis results. A lack of sensitivity in the output to these parameters will necessarily mean that there is not much information in these data to inform the value of these parameters. This may or may not be the case for different outputs, or a different problem with different physics, geometry, etc. The insignificant change in posterior distribution for friction angle for solid-wall interactions can be attributed to the choice of boundary conditions. Because no-slip boundary conditions were used for the vertical walls, only internal friction was considered. This resulted in the parameter acting as a dummy variable. The friction angle for solid-solid interactions (θ_4) exhibited a posterior distribution strongly shifted to the left (Figure 3-8d), significantly more so than the prior distribution. The drag model (θ_6) posterior distribution also changed significantly from the prior distribution. Originally all three models were weighted equally; however, as seen in Figure 3-8f, the Wen-Yu model is strongly favored. These results suggest that in future simulations of similar systems and flow regimes, the friction angle for solid-solid interactions be set to $\sim 25^\circ$ and the drag model be set to Wen-Yu, while the remaining parameters be set within their respective ranges listed in Table 3.2.

The posterior distribution of the model parameters along with the emulator can be used to predict output variables with uncertainty (e.g., bubble frequency (Figure

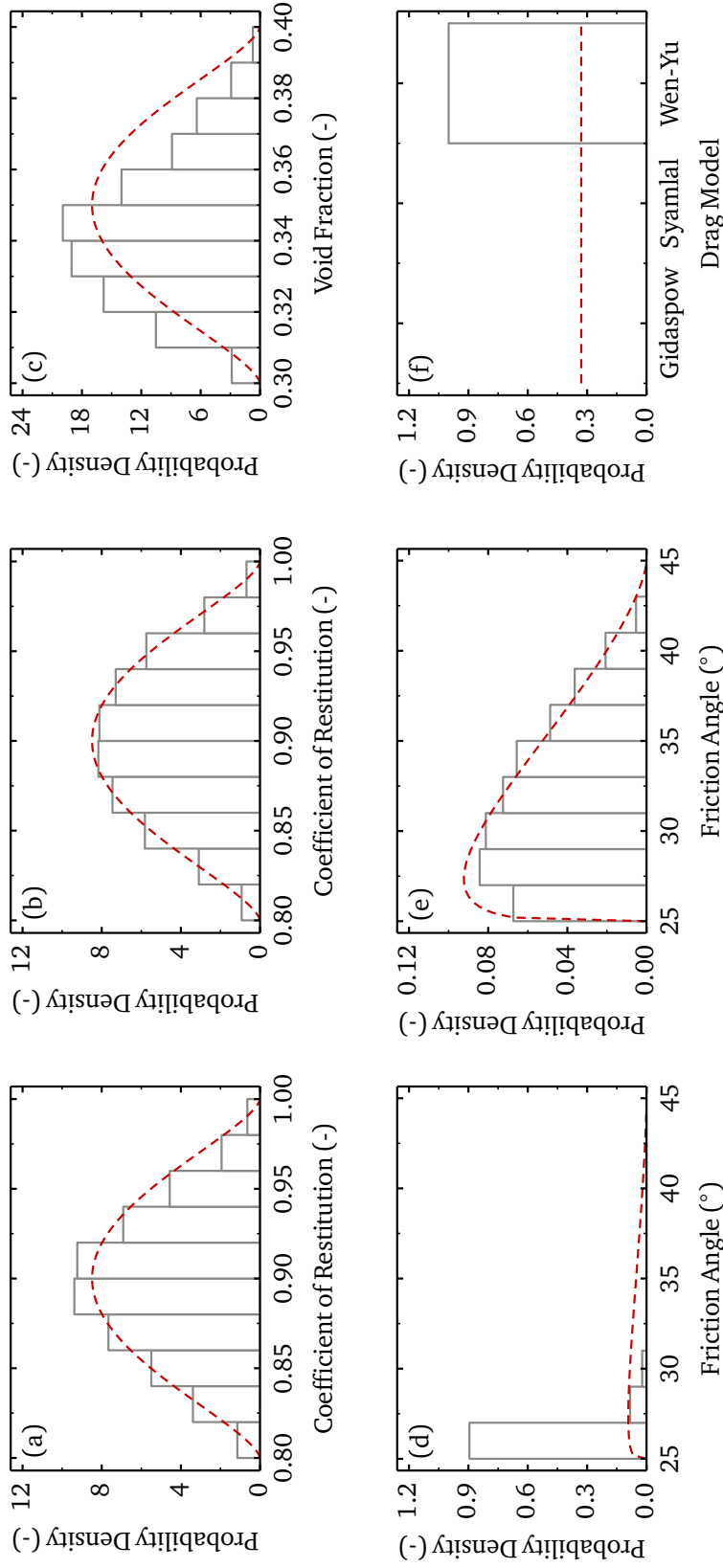


Figure 3-8: Posterior distributions of model parameters: (a) coefficient of restitution, solid-solid; (b) coefficient of restitution, solid-wall; (c) packed bed void fraction; (d) friction angle, solid-solid; (e) friction angle, solid-wall; and (f) drag models, where Syamial is the Syamial-OBrien drag model. The dashed lines are prior distributions and the histograms are posterior distributions.

3.9) and bubble phase fraction), at untested input values. To assess the predictive capability of the calibrated model (including the discrepancy term), we fit the calibration procedure four more times, each time holding out experimental data at a particular velocity. The resulting calibration fit is then used to predict the held out data to assess how well it performs out-of-sample predictions. This process is called cross-validation. At low gas velocities (i.e., $\bar{x}_2 = \{5.5, 7.0\}$ cm/s), the confidence bands are very wide and the mean over predicts the bubble frequency. At higher gas velocities (i.e., $\bar{x}_2 = \{11.0, 12.6\}$ cm/s), the emulated confidence bands are tighter, encompassing the experimental data and error [58], and the emulated mean passed through the experimental data confidence intervals [58]. Given the wide variance of CFD model results at low gas velocities (Figures 3.5a, 3.5b, 3.6a, and 3.6b), and the small variance at high gas velocities (Figures 3.5c, 3.5d, 3.6c, and 3.6d), these results are not unexpected.

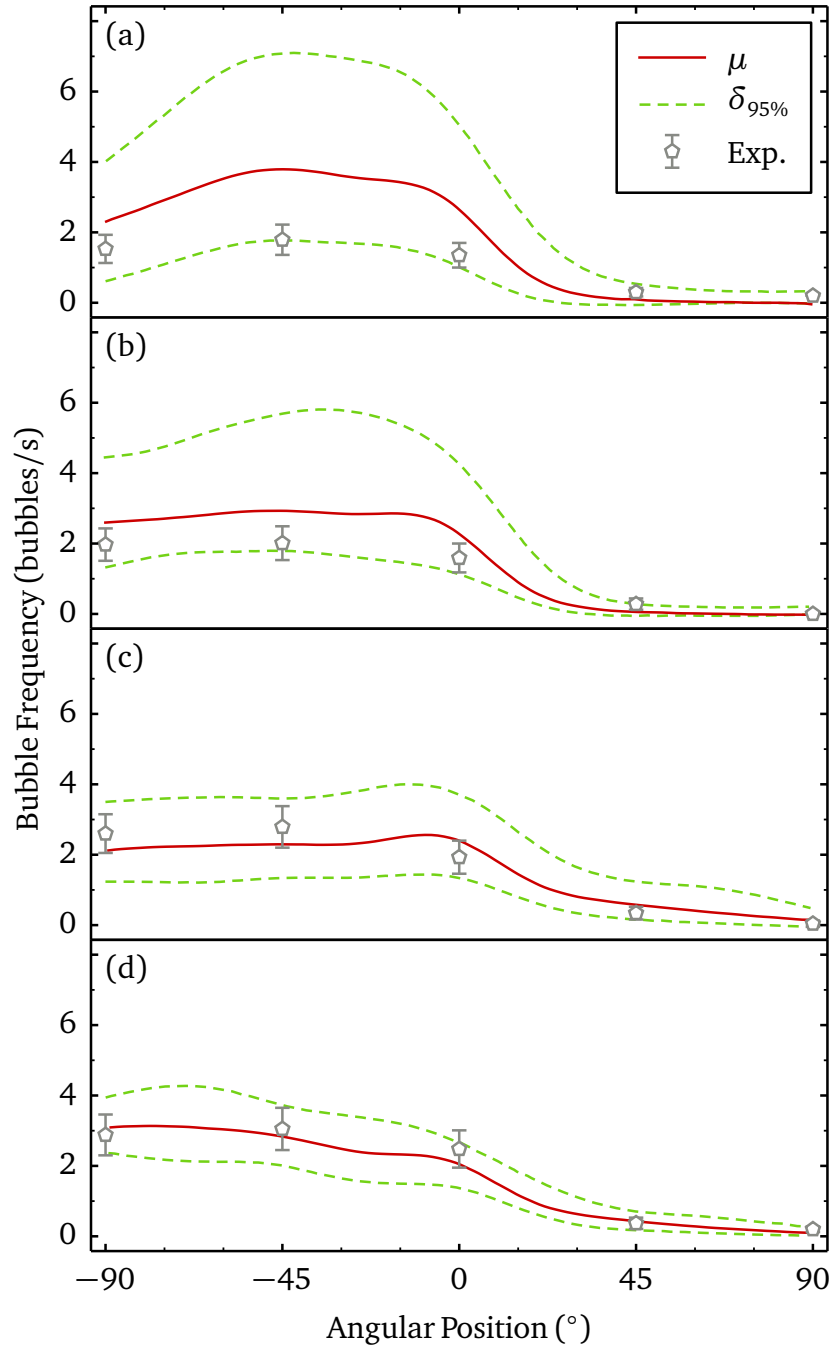


Figure 3-9: Out-of-sample bubble frequency predictions from the calibration model (including discrepancy) with 95% confidence bands for gas velocities: (a) $v_g = 5.5$, (b) $v_g = 7.0$, (c) $v_g = 11.0$, and (d) $v_g = 12.6$ cm/s; where μ is mean predicted bubble frequency, $\delta_{95\%}$ are 95% confidence bands, and Exp. is experimental results [58].

3.2 Gas-Particle Heat Transfer

Similar to the previous problem, there are many experiments which consider gas-particle flows around heated cylinders [58, 78–81]. Since we had already validated the hydrodynamics with Kim et al.’s system [58], it made most sense to validate the heat transfer with the same system. Kim et al. heated the center tube and observed the resulting local temperature profiles and heat transfer coefficients around the probe [58].

3.2.1 Setup

Using the same setup from Section 3.1, the center tube was set to a constant surface temperature of 60 °C. The physical parameters all remained the same, as listed in Table 3.1, with the addition of thermal properties. The thermal conductivity and specific heat capacity for the gas phase were set to 0.029 W/m·K and 1004 J/kg·K, respectively. The thermal conductivity and specific heat capacity for the solid phase were set to 0.2 W/m·K and 710 J/kg·K, respectively. The domain was initialized to 20 °C. Kim et al. considered several different inlet gas velocities; for this study we used an inlet gas velocity of 11 cm/s.

While a grid size of $10d_p$ is often cited as a sufficiently small grid for modeling gas-particle hydrodynamics, it does not hold true for heat transfer. This is largely due to the significant differences in the size of the fluid boundary layer and the thermal boundary layer. When the grid cells are too large the energy is diffused too quickly and results in over prediction of the heat transfer rate. Resolving the surface heat transfer requires significantly finer grids. To overcome this issue, we consider three locally refined grid sizes, where the smallest cells are $5d_p$, $2d_p$, and $1d_p$ (Figure 3-10) and the largest cells in the domain are $10d_p$.

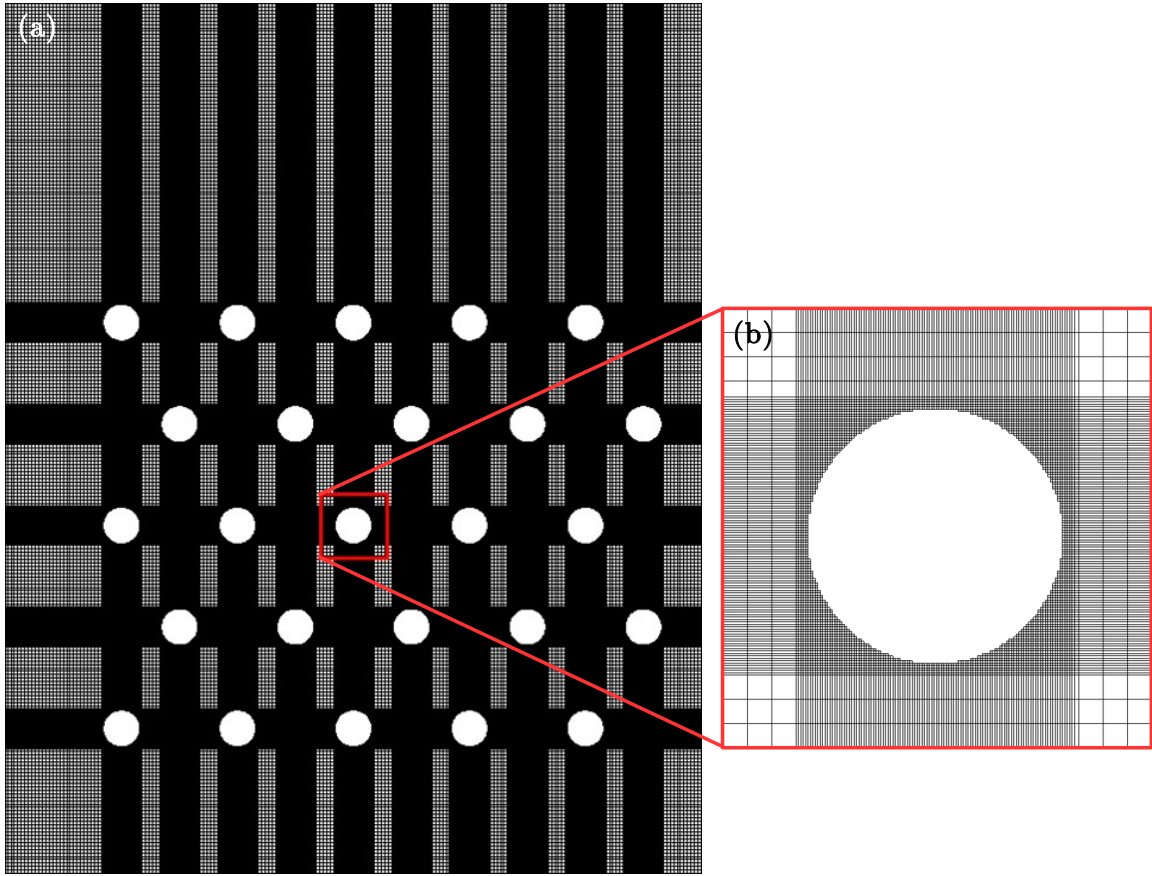


Figure 3-10: Refined mesh for Kim et al.'s system simulation, smallest grid cells are $1d_p$ and largest grid cells are $10d_p$: a) mesh of entire domain, b) close up of local refinement around cylinders.

3.2.2 Analysis

In experimental setups, it is common for the researcher to measure the heat transfer coefficient based on the power consumption from heating the cylinder (Q)

$$h = \frac{Q}{A_c \Delta T}, \quad (3.4)$$

where A_c is the cylinder area, and ΔT is the different between the cylinder temperature and the bulk temperature. However, in a simulation we can not directly measure the power consumption because the wall temperature is enforced by a boundary con-

dition. Instead we have to use local derivatives on the surface of the cylinder to calculate the rate of heat transfer [82, 83]

$$h = \frac{\phi_g k_g \frac{\partial T_g}{\partial x} + \phi_s k_s \frac{\partial T_s}{\partial x}}{T_c - T_{\text{bulk}}}, \quad (3.5)$$

where the derivatives are taken on the cylinder wall, and T_{bulk} is the average temperature of the bulk mixture. This can be written discretely as

$$h = \frac{\phi_g k_g \frac{\Delta T_g}{\Delta x} + \phi_s k_s \frac{\Delta T_s}{\Delta x}}{T_c - T_{\text{bulk}}}, \quad (3.6)$$

where ΔT is the difference between the wall boundary temperature and the nearest fluid cell, and Δx is the distance from the wall to the center of the nearest fluid cell.

3.2.3 Results

Using similar post-processing methods as Section 3.1.1, regions around the cylinder were identified as the corresponding probe locations for -90° , -45° , 0° , 45° , and 90° . The local heat transfer coefficients were calculated for each location with (3.6) and are shown in Figure 3-11 with the results from Kim et al. The results for all grid sizes show poor agreement with the literature data. The simulations consistently under predict the heat transfer and have trouble achieving the right profiles, regardless of magnitude. Even with a refined grid size of $1d_p$, we observe the highest local heat transfer coefficient is only 256 W/m·K, where as the average heat transfer coefficient for Kim et al. is around 400 W/m·K.

Snapshots of the temperature field for grid sizes $10d_p$, $2d_p$, and $1d_p$ are shown in Figure 3-12. We can see that as the grid cells get smaller, the heat transfer occurs more slowly and has time to heat up the surrounding area, whereas the large grid dissipates the heat too quickly due to the large distance it has to diffuse over (i.e., the length of one grid cell). Reviewing (3.6), it can be seen that the main contributors

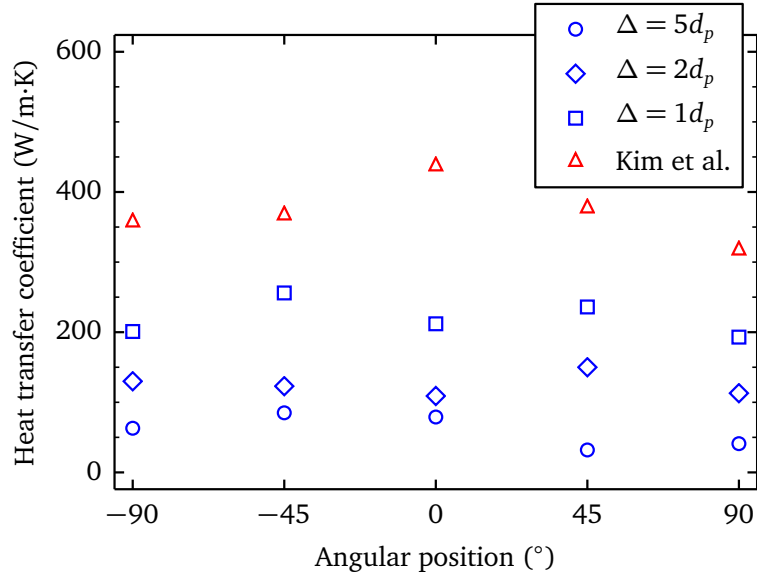


Figure 3-11: Local heat transfer coefficients from MFIX based on different grid sizes compared with data from Kim et al. with an inlet velocity of 11 cm/s [58].

to the heat transfer coefficient calculation are the temperature drop at the cylinder wall ΔT and the diffusion distance to the cell center Δx .

Because of these limiting factors in the heat transfer coefficient calculation, it is worth considering the theoretical limit achievable with this method. To maximize (3.6), we consider a cell next to the tube at maximum solids packing, $\phi_s = 0.64$ and $\phi_g = 0.36$. This maximizes the solids contribution, which typically has a signifi-

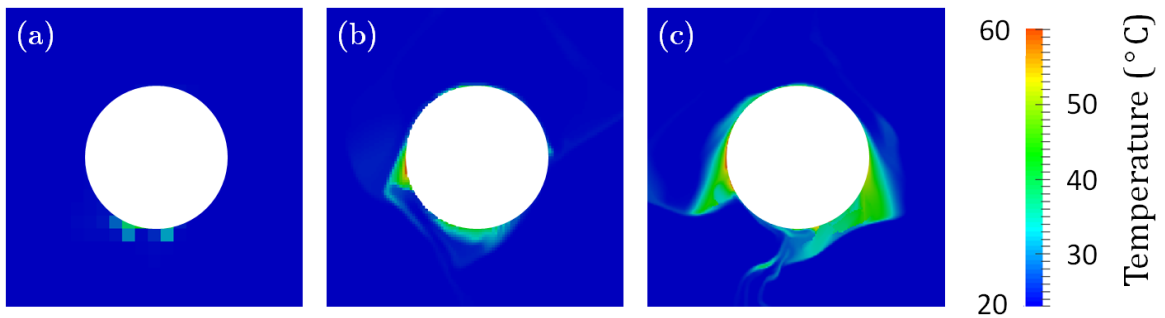


Figure 3-12: Temperature field around the central cylinder for different grid sizes: a) $10d_p$, b) $2d_p$, and c) $1d_p$.

cantly higher thermal conductivity than the gas phase. The maximum drop in heat transfer would be equal to the difference between the cylinder wall temperature and the bulk temperature, $\Delta T = T_c - T_{\text{bulk}}$. These assumptions simplify the equation to a function of material properties, which are constant, and the grid size

$$h = \frac{0.36k_g + 0.64k_s}{\Delta x}, \quad (3.7)$$

where $\Delta x = \Delta_{\text{grid}}/2$ since the finite difference is taken to the cell center. This function was plotted for varying grid cell sizes and compared with the Kim et al. average heat transfer coefficient (Figure 3-13). We see that for any grid cell larger than $1.3d_p$, the theoretical maximum is lower than the literature value. However, as Figure 3-11 showed, even a grid cell size of $1d_p$ was insufficient for predicting the local heat transfer coefficients. Using even smaller grid cells ($< 1d_p$) becomes computationally intractable, because not only does the number of grid cells increase at an $\mathcal{O}(n^2)$ rate as size changes, but the time steps must reduce to maintain stability of the system.

Because it not possible to accurately predict local heat transfer properties (using these numerical methods), we investigated the prediction of global heat transfer properties and the overall temperature field by developing a subgrid model for the unresolved cylinder-suspension heat transfer (Chapter 4).

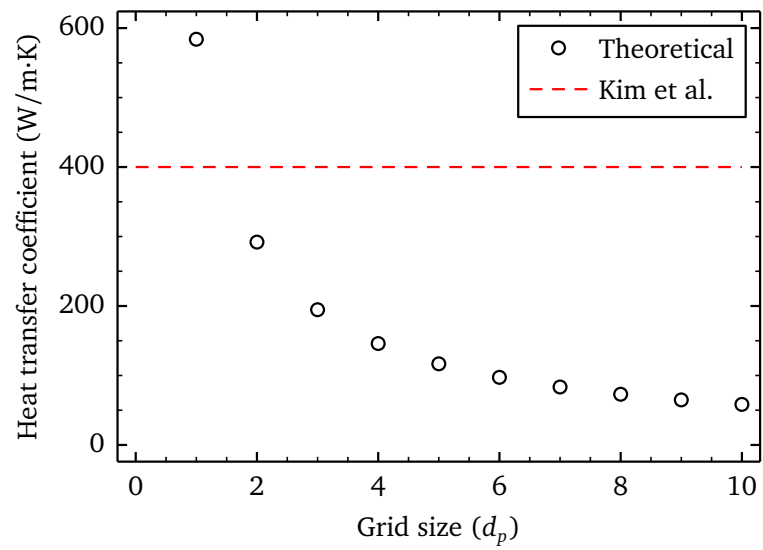


Figure 3-13: Theoretical maximum heat transfer coefficient attainable with (3.7) compared with Kim et al.'s average value [58].

Chapter 4

Subgrid Models

As demonstrated in Section 3.2, calculating accurate local heat transfer coefficients can be computationally intractable, requiring extremely fine meshes and small time steps. Even with modern super computers, solving a laboratory-scale system can take months with many processors working in parallel. This is the motivation behind developing subgrid models for coarse-grid heat transfer.

The proposed heat transfer subgrid model builds on- and is analogous to the subgrid model for drag developed by Sarkar et al. [14], where coarse-grid cylinder-suspension drag was calculated as a function of flow behavior and geometry configurations, and implemented through source terms in the momentum governing equations. Similarly, we constitute a coarse-grid cylinder-suspension heat transfer model in terms of the materials properties, flow conditions, and geometry configurations, and implement it via a source term in the energy governing equations. The result is an accurate, efficient method for simulating large-scale multiphase systems with heat transfer due to immersed geometry. However, it is worth noting that due to the nature of the coarse-grid, we sacrifice the ability to make local predictions of heat transfer coefficients (as reported by [58, 84]) for efficiency.

This chapter details the development and testing of the subgrid model. Section 4.1 describes the domain and simulation setup. Section 4.2 details the mathematical formulation of the filtering method. Sections 4.3 and 4.4 present the grid-cell-size and filter-size convergence studies, respectively. Section 4.5 describes the model develop-

ment and optimization and Section 4.6 details the model implementation in MFIX. The verification, validation, and uncertainty quantification of the model are covered in Sections Sections 4.7, 4.8, and 4.9, respectively.

4.1 Setup

The simulation domain is motivated by the system presented in Chapter 3 (left-hand side of Figure 4.1). Based on this system, we construct a smaller 2D unit cell sub-domain (right-hand side of Figure 4.1). This sub-domain is representative of the full system, that is, the periodic unit cell denotes a region in the interior of the bed away from the walls. By using a smaller sub-domain, the full range of possible flow conditions and geometric configurations can be simulated more efficiently. Hereinafter, domain will refer to the reduced 2D periodic unit cell unless explicitly noted otherwise.

To idealize the flow that occurs in the interior of a fluidized bed, the domain's boundaries are periodic, shown as black-dashed lines in Figure 1. A macroscopic flow is induced within the domain by imposing a pressure difference along the y-direction, opposite gravity. This pressure drop across the vertical periodic boundaries is defined as a surplus to the suspension pressure, i.e., the pressure needed to balance the weight of the gas-solid mixture, given by:

$$p_g = (\phi_g \rho_g + \phi_s \rho_s) g \ell \quad (4.1)$$

where p_g is the suspension gas pressure, ϕ is phase fraction, ρ is density, g is gravitational acceleration, ℓ is the length of the domain, and subscripts g and s denote gas and solid phases, respectively. The rate and direction of flow are controlled using the value of the gas pressure drop, Δp_g . When Δp_g is positive, the net suspension momentum is positive (i.e., upwards), against gravity, and conversely when Δp_g is negative the net momentum is negative. Thus, we are able to prescribe the various

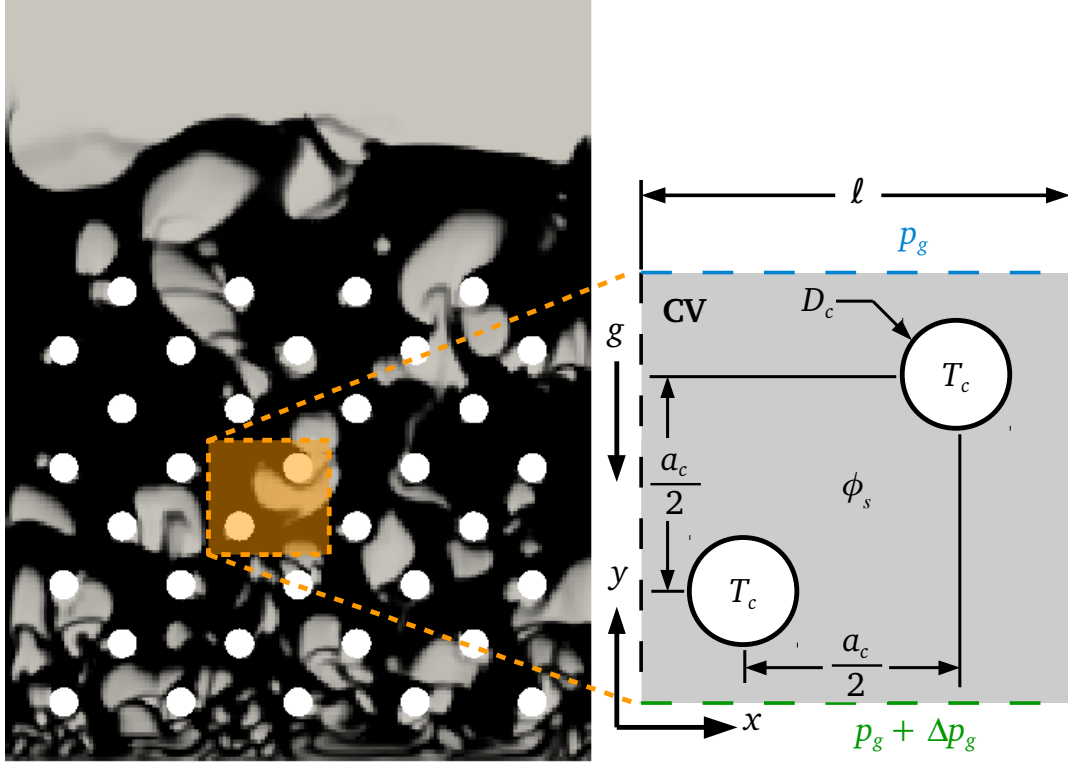


Figure 4.1: Laboratory-scale fluidized bed simulation (left) and periodic unit-cell domain (right), where D_c is cylinder diameter, a_c is cylinder spacing, T_c is cylinder surface temperature, ϕ_s is solids fraction, p_g is gas pressure, Δp is the gas pressure drop, \mathbf{g} is gravitational acceleration, $\ell = a_c$ is the length of the domain, and CV is the control volume, shown in gray.

flow velocities typically encountered in a large-scale device. Immersed horizontal heat transfer cylinders are present in the domain. The boundary conditions on the cylinder surfaces are defined as no-slip flow for both gas and solids, and a constant predefined surface temperature T_c (i.e., Dirichlet boundary condition). The curvature of the immersed cylinders is approximated using MFIX's Cartesian cut-cell feature [85], which truncates cells that intercept curvilinear boundaries, creating quadrilateral and triangular cut-cells.

The flow region is initialized as a stationary, homogeneous mixture of gas and solids with an initial suspension temperature of 20 °C. The gas phase is modeled as air

and the solid phase represents carbon-capture sorbent (based on physical properties). For the purpose of model derivation and error analysis, a generic source term \dot{Q}_s is appended to the solid phase governing energy equation (2.7) with the form

$$\dot{Q}_s = \phi_s \rho_s C_{p,s} \dot{\Pi}_s, \quad (4.2)$$

where $\dot{\Pi}_s$ is the heat generation rate. The value of the generation rate is arbitrary and does not affect the resulting model. Material properties are adapted from previous studies [24, 53] and are listed in Table 4.1. Additionally we define two characteristic values used to non-dimensionalize quantities: a length and a velocity. These characteristic values are based on the solids terminal velocity v_t , which has been shown to describe the hydrodynamics of the solids phase well in past studies [14, 16, 24, 86]. These characteristic values are also defined in Table 4.1.

In gas-solid flows, hydrodynamic grid-independent (statistically averaged) results are typically achieved using grid-cell sizes near 10 times the particle diameter d_p [20, 87]. As such, previous work on gas-particle sub-grid model development has employed fine-grid sizes of $16.667 d_p$ [16] and $8.333 d_p$ [14, 16, 20, 24]. However, as will be described in Section 4.3, accurate resolution of the heat transfer was only achieved with grid-cells no larger than $400 \mu\text{m}$, independent of particle size. As a result, this study uses a finer grid size of $400 \mu\text{m}$, with the exception of the cut cells which varied and had a minimum cell length of $100 \mu\text{m}$. MFIX employs an adaptive time step algorithm to maintain stability. The time steps were bounded between 10^{-10} and 10^{-3} seconds, with a mean time step of approximately 10^{-5} seconds.

Table 4.1: Material properties and parameters.

Parameter	Symbol	Value	Units
Gas phase			
Density	ρ_g	1.2	kg/m ³
Viscosity	μ_g	$18 \cdot 10^{-6}$	m ² /s ²
Thermal conductivity	k_g	0.024	W/m·K
Specific heat capacity	$C_{p,g}$	1000	J/kg·K
Solid phase			
Diameter	d_p	100	μm
Density	ρ_s	441	kg/m ³
Thermal conductivity	k_s	0.2	W/m·K
Specific heat capacity	$C_{p,s}$	1000	J/kg·K
Restitution coefficient	e	0.9	
Friction angle	θ	28.0	°
Generation rate	$\dot{\Pi}_s$	1	K/s
Characteristic values			
Length	$L^* = v_t^2/g$	0.00180	m
Velocity	$v^* = v_t$	0.133	m/s
Cylinder geometry			
Diameter	D_c	3	cm
Spacing	a_c	12	cm

4.2 Filtering Methods

Calculation of the effective cylinder-suspension heat transfer can be accomplished by filtering the governing energy equations over the simulation domain. The filtering approach outlined in this study is analogous to that used by Igci et al. [16], Sarkar et al. [14], and Agrawal et al. [24].

We define a top-hat filter function, $G(\mathbf{x})$, over the control volume, CV , such that

$$\int_{CV} G(\mathbf{x}) dV = 1. \quad (4.3)$$

This filter is then applied to the flow variables: phase volume fractions, velocities, and temperatures, to define new, filtered flow variables:

$$\bar{\phi}_i = \frac{1}{V_{CV}} \int_{CV} \phi_i dV, \quad (4.4)$$

$$\bar{\phi}_i \tilde{\mathbf{v}}_i = \frac{1}{V_{CV}} \int_{CV} \phi_i \mathbf{v}_i dV, \quad (4.5)$$

$$\bar{\phi}_i \tilde{T}_i = \frac{1}{V_{CV}} \int_{CV} \phi_i T_i dV, \quad (4.6)$$

where $i = g, s$, the overbar denotes the volume averages, and the overtilde denotes the Favre average weighted by respective phase fractions. The Reynolds decomposition for the flow variables can then be written in terms of these filtered quantities as:

$$\phi_i = \bar{\phi}_i + \phi'_i, \quad (4.7)$$

$$\mathbf{v}_i = \tilde{\mathbf{v}}_i + \mathbf{v}'_i, \quad (4.8)$$

$$T_i = \tilde{T}_i + T'_i, \quad (4.9)$$

where the prime denotes the spatial fluctuating components about the respective mean values.

To obtain the net cylinder-suspension heat transfer, we write the total energy of the system by summing (2.6) and (2.7), eliminating the interphase heat transfer terms

$$\begin{aligned}
& \frac{\partial}{\partial t} (\phi_g \rho_g C_{p,g} T_g + \phi_s \rho_s C_{p,s} T_s) + \nabla \cdot (\phi_g \rho_g C_{p,g} \mathbf{v}_g T_g + \phi_s \rho_s C_{p,s} \mathbf{v}_s T_s) \\
& = \nabla \cdot (\phi_g k_g \nabla T_g + \phi_s k_s \nabla T_s) + \dot{Q}_s.
\end{aligned} \tag{4.10}$$

Applying the filter $G(\mathbf{x})$ to Equation (4.10) yields

$$\begin{aligned}
& \frac{1}{V_{CV}} \int_{CV} \frac{\partial}{\partial t} (\phi_g \rho_g C_{p,g} T_g + \phi_s \rho_s C_{p,s} T_s) dV \\
& + \frac{1}{V_{CV}} \int_{CV} \nabla \cdot (\phi_g \rho_g C_{p,g} \mathbf{v}_g T_g + \phi_s \rho_s C_{p,s} \mathbf{v}_s T_s) dV \\
& = \frac{1}{V_{CV}} \int_{CV} \nabla \cdot (\phi_g k_g \nabla T_g + \phi_s k_s \nabla T_s) dV + \frac{1}{V_{CV}} \int_{CV} \dot{Q}_s dV
\end{aligned} \tag{4.11}$$

Substituting the values from (4.2) and (4.7)–(4.9) reduces (4.11) to

$$\frac{\partial}{\partial t} (\bar{\phi}_g \rho_g C_{p,g} \tilde{T}_g + \bar{\phi}_s \rho_s C_{p,s} \tilde{T}_s) = \frac{1}{V_{CV}} \oint_{S_c} (\phi_g k_g \nabla T_g + \phi_s k_s \nabla T_s) \cdot \hat{\mathbf{n}}_c dS + \bar{\phi}_s \rho_s C_{p,s} \dot{\Pi}_s \tag{4.12}$$

where S_c is the cylinder surface and $\hat{\mathbf{n}}_c$ is the normal vector to the cylinder surface, pointing outward. This simplification is made possible by the divergence theorem; the convective terms can be converted to two surface integrals: one over the periodic boundaries and the other over the cylinders. The surface integrals of the convective terms computed over the periodic boundaries are identically zero. If we analyze the system after it has reached pseudo steady-state the expression is further simplified as the transient term disappears. The remaining surface-integral about the cylinders represents the averaged or filtered volumetric suspension-cylinder heat transfer, defined as \bar{Q}_{sc} , for which we want to constitute a closure equation for

$$\bar{Q}_{sc} = -\bar{\phi}_s \rho_s C_{p,s} \dot{\Pi}_s. \quad (4.13)$$

We propose a standard convective heat transfer model for the filtered volumetric cylinder-suspension heat transfer rate

$$\bar{Q}_{sc} = \frac{\bar{h}_{sc} A_c (T_c - \tilde{T}_{\text{susp}})}{V_{CV}}, \quad (4.14)$$

where \bar{h}_{sc} is the filtered cylinder-suspension heat transfer coefficient, A_c is cylinder surface area, T_c is the cylinder surface temperature, and \tilde{T}_{susp} is the average suspension temperature, defined as

$$\tilde{T}_{\text{susp}} = \frac{1}{V_{CV}} \int_{CV} \phi_g T_g + \phi_s T_s \, dV. \quad (4.15)$$

With (4.13) and (4.14) we can calculate the filtered cylinder-suspension heat transfer coefficient, \bar{h}_{sc}

$$\bar{h}_{sc} = \frac{\bar{\phi}_s \rho_s C_{p,s} \dot{\Pi}_s V_{CV}}{A_c (T_c - \tilde{T}_{\text{susp}})}, \quad (4.16)$$

The cylinder-suspension heat transfer can then be non-dimensionalized by formulating a filtered cylinder-suspension Nusselt number,

$$\overline{\text{Nu}}_{cs} = \frac{\bar{h}_{sc} L^*}{k_s}, \quad (4.17)$$

where L^* is the characteristic length and k_s is the solids thermal conductivity (Table 4.1).

Using the propagation of error formula [88] we can formulate the standard deviation of the filtered cylinder-suspension Nusselt number as

$$\sigma_{\overline{\text{Nu}}_{cs}} = \sqrt{\left(\frac{\bar{\phi}_s \rho_s C_{p,s} \dot{\Pi}_s}{A_c (T_c - \tilde{T}_{\text{susp}})^2}\right)^2 \sigma_{\tilde{T}_{\text{susp}}}^2}. \quad (4.18)$$

where $\sigma_{\tilde{T}_{\text{susp}}}$ is the standard deviation of the filtered suspension temperature.

In this work, we seek to construct a correlation for $\overline{\text{Nu}}_{cs}$ for different material properties, flow conditions, and geometry configurations.

4.3 Grid Size Determination

A grid sensitivity study was performed to determine the appropriate cell size. Chapter 3.2 showed that even $1d_p$ was not sufficient for resolving local heat transfer coefficients however, because we are now calculating global heat transfer rates, we must perform another set of grid tests to determine the largest possible grid size for proceeding with the subgrid model development.

A campaign of 9 simulations was setup to study the convergence of results when varying the grid cell size. Three sizes of particle diameters were considered: 100, 200, and 300 μm . For each particle size, three grid cell sizes were considered: 200, 400, and 800 μm . All other material and simulation properties were identical for all simulations (Table 4.1). The simulations were run for 10 seconds, sufficient time for determining the pseudo steady-state filtered suspension temperature. Using (4.17) and (4.16) the filtered cylinder-suspension Nusselt number was calculated for each simulation and scaled to the [0,1] interval for each particle diameter (Figure 4-2).

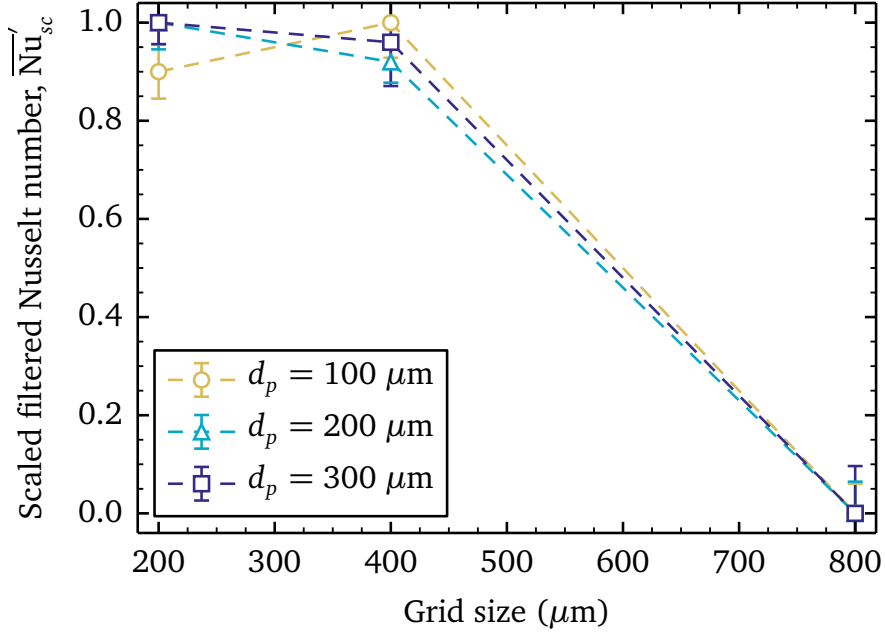


Figure 4-2: Scaled filtered Nusselt number vs. grid size for particle diameters: 100, 200, and 300 μm , with $\bar{\phi}_s = 0.3$ and $|\tilde{\mathbf{v}}_s| = 0.5$. Error bars denote 95% confidence intervals.

From this we see that grid independence is achieved for grid cell sizes around 400 μm . Unlike the hydrodynamics-only simulations, for this particular system, the appropriate grid cell size is not a function of particle size. This seems reasonable as the thermal boundary layer is generally a function of the Prandtl number, i.e., related to the thermal properties of the fluid. The remaining simulations in this study were performed using a grid size of 400 μm .

4.4 Filter Size Determination

The domain in Figure 4-1 represents the minimum filter size possible and is referred to as a unit cell. Using this unit cell we can construct filters of various sizes (Figure 4-3), with the restriction that they are integer multiples of the unit cell. It is important to ensure that the filter is large enough to capture the flow and heat transfer characteristics at all length scales. Conversely, we want to minimize the size to reduce

computation time. To determine the minimum acceptable filter size, we consider four different filter sizes: ℓ , 2ℓ , 3ℓ , and 4ℓ , where ℓ represents the smallest unit-cell size (Figure 4-3). Identical simulation conditions were used for each filter size (Table 4.1) and the simulations were run for 10 seconds, sufficient time for determining the pseudo steady-state filtered suspension temperature.

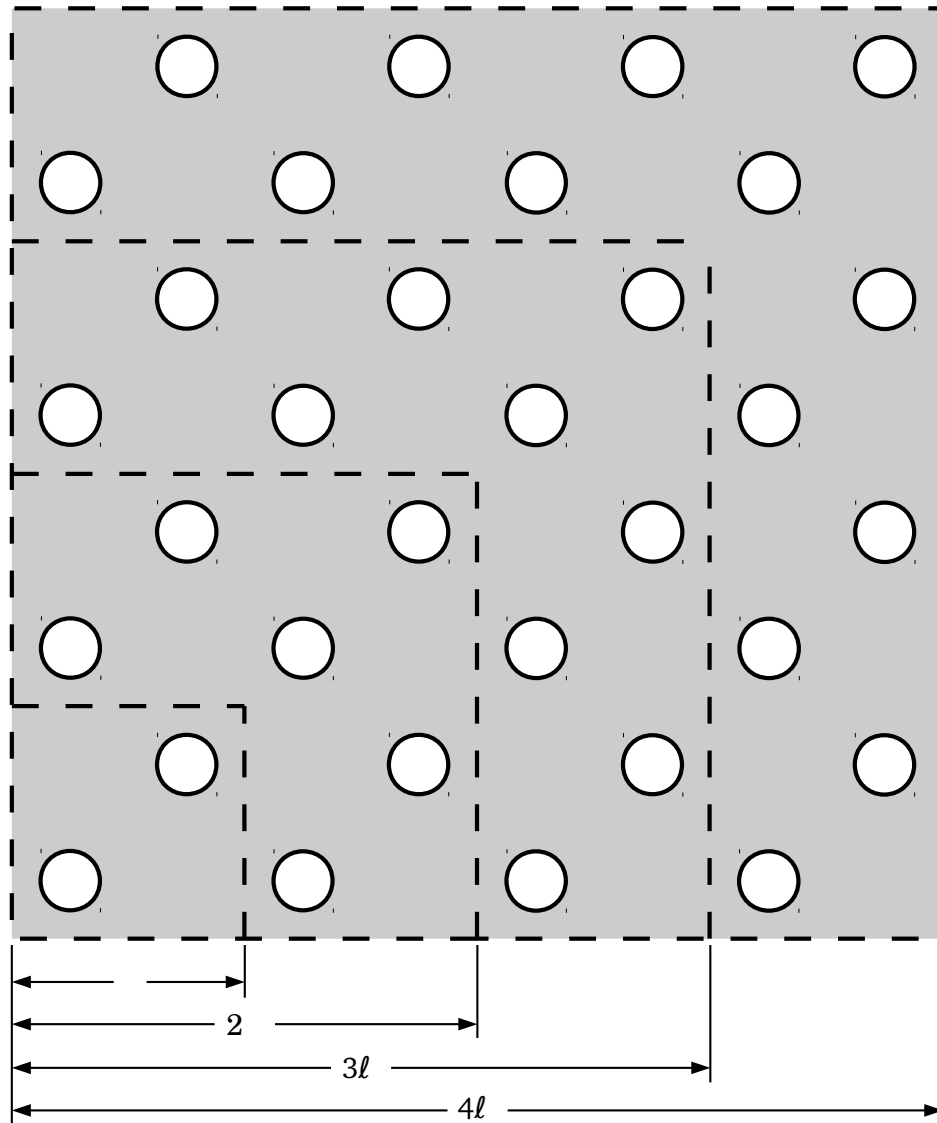


Figure 4-3: Filter domains considered to determine the optimal filter size, expressed as integer multiples of the unit-cell size ℓ , with $\bar{\phi}_s = 0.3$ and $|\tilde{\mathbf{v}}_s| = 0.5$ m/s.

The simulations were processed using the same method described in the grid study (Section 4.3). The results show no significant differences across all filter sizes, indicating that filter size independence is achieved at the smallest filter size, $L = \ell$ (Figure 4.4). For the remainder of the study, all simulations were run with domains of filter-size $L = \ell = a_c$.

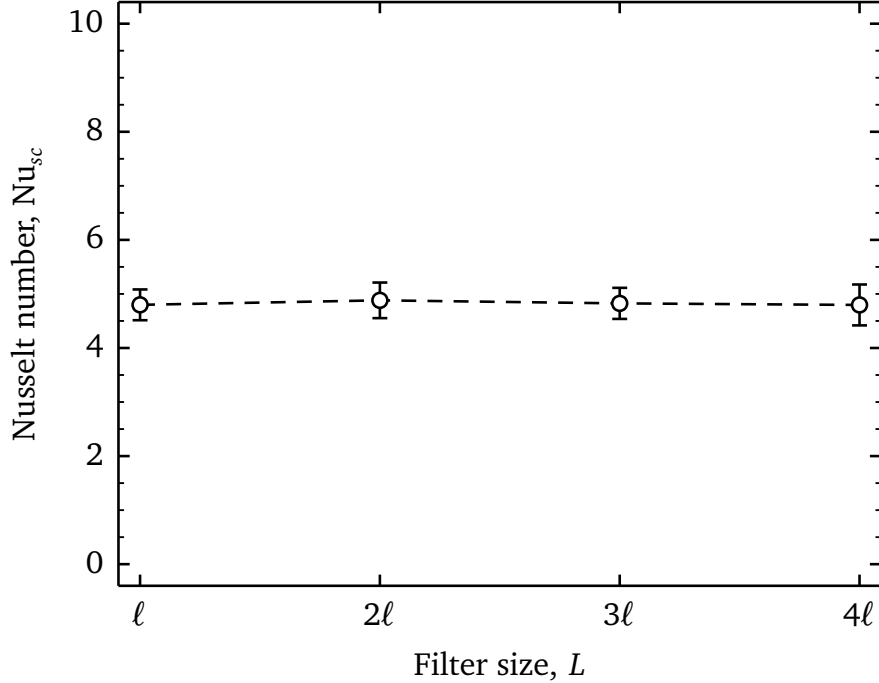


Figure 4.4: Nusselt number vs. filter size to determine minimum acceptable filter size, with $\bar{\phi}_s = 0.3$ and $|\tilde{\mathbf{v}}_s| = 0.5$. The error bars represent 95% confidence intervals.

4.5 Developing the Constitutive Model

To develop the sub-grid model, we first complete a dimensional analysis to determine the effective terms for formulation. Using the Buckingham-Pi theorem [89] with the set of variables $\{\bar{\phi}_s, |\tilde{\mathbf{v}}_s|, \rho_s, C_{p,s}, k_s, d_p, D_c, a_c, \bar{h}_{sc}\}$ and set of basis variables: $\{L^*, v_t, \rho_s, k_s\}$ results in the following dimensionless Pi groups:

$$\Pi_1 = \phi_s, \quad (4.19)$$

$$\Pi_2 = |\tilde{\mathbf{v}}_s|/v_t, \quad (4.20)$$

$$\Pi_3 = D_c/a_c, \quad (4.21)$$

$$\Pi_4 = \rho_s C_{p,s} v_t L^* / k_s = \overline{\text{Pe}}_{cs}, \quad (4.22)$$

$$\Pi_5 = \bar{h}_{sc} L^* / k_s = \overline{\text{Nu}}_{cs}, \quad (4.23)$$

where Π_2 is the dimensionless filtered solids velocity, Π_3 is the ratio of cylinder diameter to spacing, Π_4 is the filtered Peclet number, and Π_5 is the filtered cylinder-suspension Nusselt number. Note that we have chosen to exclude the gas viscosity, and the corresponding dimensionless Prandtl number ($\text{Pr}_g = C_{p,g} \mu_g / k_g$), from the list above. The cylinder-suspension heat transfer occurs primarily through the particles, and not through the gas and, therefore, the influence of the Prandtl number on $\overline{\text{Nu}}_{cs}$ is not important for particle-laden flows.

According to the Buckingham-Pi theorem, the Nusselt number can be written as a function of the other dimensionless Π groups. We choose to correlate $\overline{\text{Nu}}_{cs}$ using a decoupled expression of the form

$$\overline{\text{Nu}}_{cs} = f_1(\bar{\phi}_s) f_2(|\tilde{\mathbf{v}}_s|/v_t) f_3(D_c/a_c) f_4(\overline{\text{Pe}}_{cs}), \quad (4.24)$$

where f_1 , f_2 , f_3 , and f_4 are yet unknown functions of their respective arguments. To determine these functions, we vary the dimensionless groups over a physically relevant range (Table 4.2) while holding the others at constant values, similar to a factorial experimental design.

Table 4.2: Pi-group values for simulation campaign.

Variable	Values		
	Nominal	Minimum	Maximum
$\bar{\phi}_s$	0.3	0.01	0.6
D_c/a_c	0.25	0.1	0.4
$ \tilde{\mathbf{v}}_s /v_t$	3.8	0.6	7.0
$\overline{\text{Pe}}_{cs}$	530	370	1,330

First the solids fraction is varied between 0.01–0.6 to simulate the spectrum from very dilute to very dense systems. The Nusselt number dependence on solids fraction is significant (Figure 4.5). We see that the behavior is similar to a power law, and we propose the following model form

$$f_1(\bar{\phi}_s) \propto \bar{\phi}_s^{\beta_1}, \quad (4.25)$$

where β_1 is an exponent determined through nonlinear regression. Similar behavior is observed with previous models [14, 16, 24]. The model was generated using SciPy’s nonlinear regression called `curve_fit` [90]. The value of β_1 was found to be 0.125, which agrees well with the data (Figure 4.5). In the limit where the solid fraction goes to zero, a standard single-phase Nusselt number correlation may be used, detailed in Section 4.6.

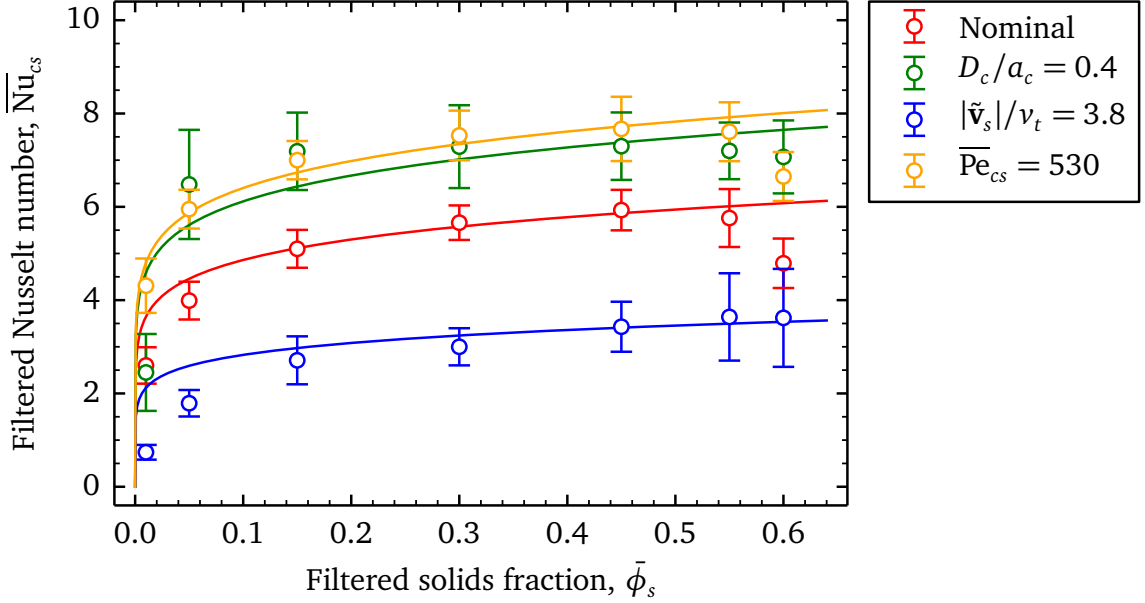


Figure 4-5: The Nusselt number vs. solids fraction for $D_c/a_c = 0.25$, $|\tilde{v}_s|/v_t = 3.8$, and $\overline{Pe}_{cs} = 530$, except as noted by the legend. Markers represent simulated data with $\pm\sigma_{\overline{Nu}_{cs}}$ error bars and the solid lines denote the model fit.

The ratio of cylinder diameter to spacing was varied between 0.1–0.4, a range often reported in textbooks and literature (see, for example, [91, 92]), by varying the cylinder spacing and holding the cylinder diameter at 3 cm. The effect of D_c/a_c on the Nusselt number was also well-correlated to a power-law and fitted using a polynomial model with an unknown power,

$$f_2 \left(\frac{D_c}{a_c} \right) \propto 1 + \beta_{2,1} \left(\frac{D_c}{a_c} \right)^{\beta_{2,2}}, \quad (4.26)$$

where $\beta_{2,1}$ and $\beta_{2,2}$ are determined through nonlinear regression. The values of $\beta_{2,1}$ and $\beta_{2,2}$ are found to be 2.94 and 1.76 respectively, which agrees well with the data (Figure 4-6), capturing the trend and passing through the error bars of the data. Furthermore the proposed form ensures that as the cylinder diameter increases so does the Nusselt number, and inversely as the cylinder spacing increases the term

decreases asymptotically. A similar relationship is observed in single phase flow [92].

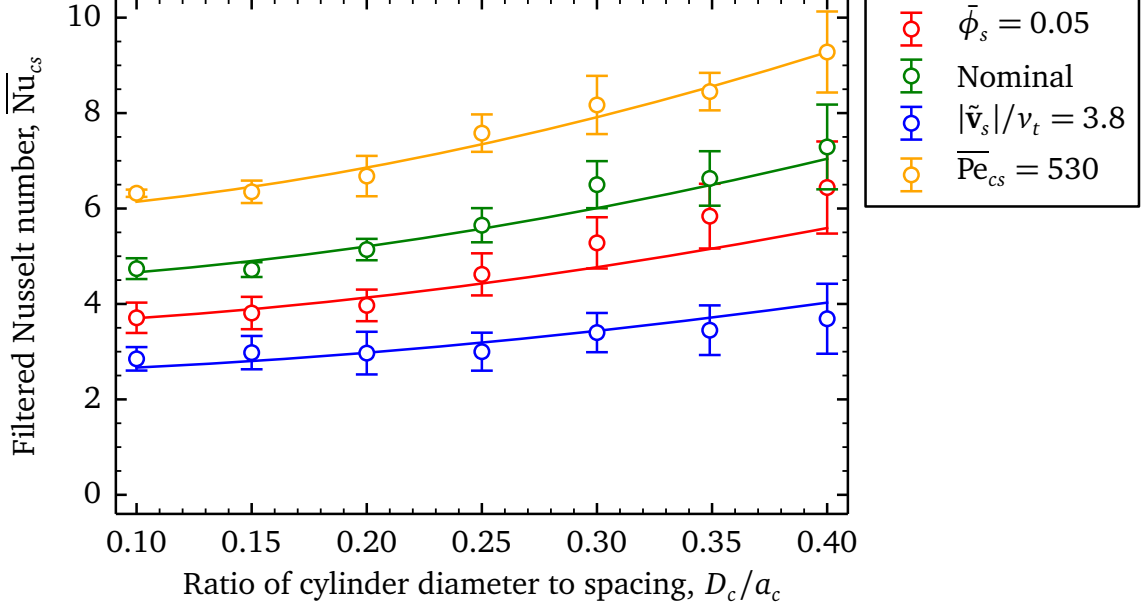


Figure 4-6: The Nusselt number vs. cylinder diameter-spacing ratio for $\bar{\phi}_s = 0.3$, $|\tilde{\mathbf{v}}_s|/v_t = 3.8$ and $\overline{\text{Pe}}_{cs} = 530$, except as noted by the legend. Markers represent simulated data with $\pm\sigma_{\overline{\text{Nu}}_{cs}}$ error bars and the solid lines denote the model fit.

The dimensionless filtered solids velocity was varied between 0.6–7.0 by varying the pressure drop to achieve a mean solids velocity of 0.1–1.0 m/s. We propose a power-law model, analogous to the Reynolds number term present in single-phase flow heat transfer correlations,

$$f_3 \left(\frac{|\tilde{\mathbf{v}}_s|}{v_t} \right) \propto \left(\frac{|\tilde{\mathbf{v}}_s|}{v_t} \right)^{\beta_3}, \quad (4.27)$$

where β_3 was found to be 0.341 through nonlinear regression. This form fits the data well and satisfies the limits of going to zero when net flow is zero (Figure 4-7).

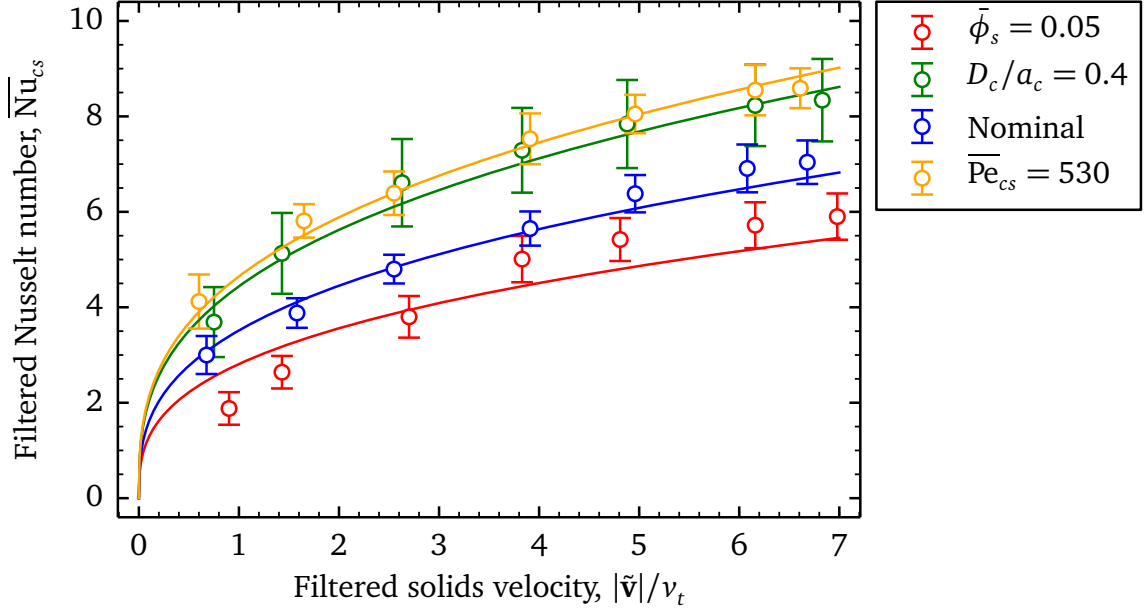


Figure 4.7: The Nusselt number vs. filtered solids velocity for $\bar{\phi}_s = 0.3$, $D_c/a_c = 0.25$, and $\bar{Pe}_{cs} = 530$, except as noted by the legend. Markers represent simulated data with $\pm\sigma_{\bar{Nu}_{cs}}$ error bars and the solid lines denote the model fit.

The filtered Peclet number was varied between 370–1,330, by varying the specific heat capacity between 700–2,500 J/kg \cdot K. The Nusselt number is fit well using a power law,

$$f_4(\bar{Pe}_{cs}) \propto \bar{Pe}_{cs}^{\beta_4}, \quad (4.28)$$

where β_4 is determined to be 0.353 through nonlinear regression (Figure 4.8). Thus, we find a relationship between the Nusselt number and thermal properties $\bar{Nu}_{s,c} \propto C_p k_s^{-1}$, which is similar to the Prandtl number term present in traditional single-phase heat transfer correlations.

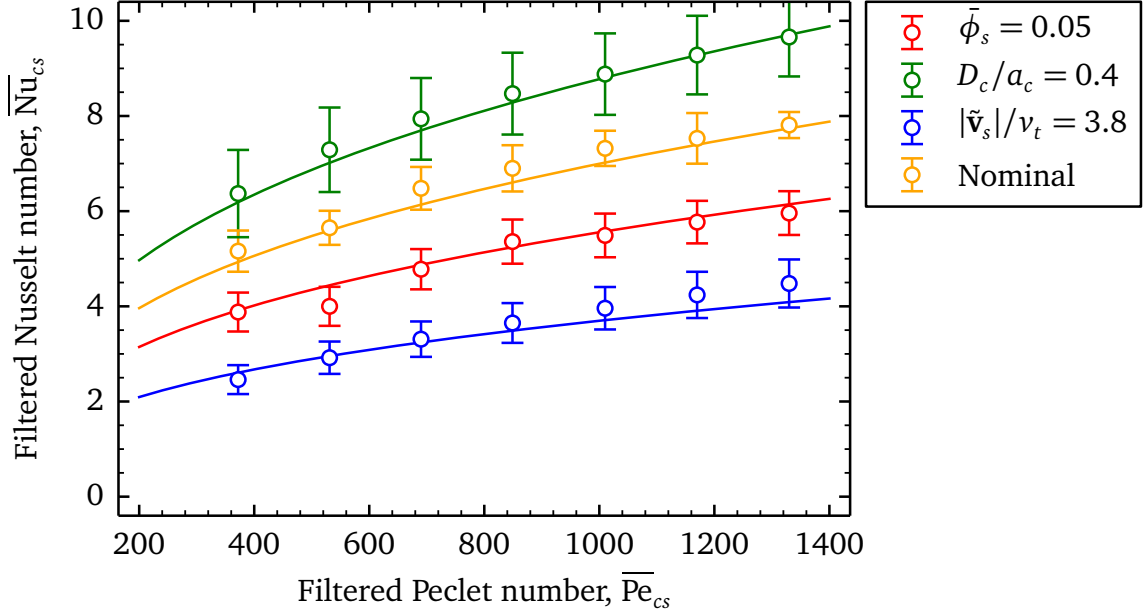


Figure 4-8: The Nusselt number vs. Peclet number for $\bar{\phi}_s = 0.3$, $D_c/a_c = 0.25$, and $|\tilde{\mathbf{v}}_s|/v_t = 3.8$, except as noted by the legend. Markers represent simulated data with $\pm\sigma_{\overline{\text{Nu}}_{cs}}$ error bars and the solid lines denote the model fit.

In summary, the individual function forms f_1 , f_2 , f_3 , and f_4 , are substituted back in (4.24) to provide the form of the closure model,

$$\overline{\text{Nu}}_{cs} \propto \bar{\phi}_s^{\beta_1} \left[1 + \beta_{2,1} \left(\frac{D_c}{a_c} \right)^{\beta_{2,2}} \right] \left(\frac{|\tilde{\mathbf{v}}_s|}{v_t} \right)^{\beta_3} \overline{\text{Pe}}_{cs}^{\beta_4}. \quad (4.29)$$

This equation is then fit with all of the data simultaneously to determine the final values for all unknowns and the proportionality factor,

$$\overline{\text{Nu}}_{cs} = 0.354 \bar{\phi}_s^{0.125} \left[1 + 2.94 \left(\frac{D_c}{a_c} \right)^{1.76} \right] \left(\frac{|\tilde{\mathbf{v}}_s|}{v_t} \right)^{0.341} \overline{\text{Pe}}_{cs}^{0.353}. \quad (4.30)$$

4.6 Implementation

The rate of heat transfer is largely driven by the flow conditions, as such for coarse grid simulations we must ensure that the hydrodynamics are correctly calculated to ensure the accuracy of the heat transfer model. We implement the Igci et al. gas-particle drag model [16] in regions where no cylinders are present and the Sarkar et al. cylinder-suspension drag model [14] in regions containing cylinders. When performing coarse grid simulations the grid cells are often $\mathcal{O}(\text{cm})$, too coarse to allow resolution of the immersed geometry. The cylinder-suspension drag model calculates the drag due to the immersed bodies by implementing a secondary, stationary solid phase, and modifying the governing equations. The stationary solid phase is modeled as a porous media and has a constant phase fraction equal to the volume ratio of the cylinders to the unit cell,

$$\bar{\Phi}_c = \frac{V_c}{V_{tot}} = \frac{\frac{\pi}{4}D_c^2}{\frac{1}{2}a_c^2}, \quad (4.31)$$

where $\bar{\Phi}_c$ is the cylinder's filtered phase fraction. With this, we calculate the corrected filtered phase-fractions, velocities, and temperatures for the gas and moving solid phase:

$$\bar{\Phi}_i = (1 - \bar{\Phi}_c)\bar{\phi}_i, \quad (4.32)$$

$$\tilde{\mathbf{V}}_i = \bar{\Phi}_i\tilde{\mathbf{v}}_i, \quad (4.33)$$

$$\tilde{\Theta}_i = \bar{\Phi}_i\tilde{T}_i. \quad (4.34)$$

Using (4.14) and (4.32)–(4.34), we can re-write the corrected governing energy equations,

$$\frac{\partial}{\partial t}(\bar{\Phi}_g \rho_g C_{p,g} \tilde{\Theta}_g) + \nabla \cdot (\bar{\Phi}_g \rho_g C_{p,g} \tilde{\mathbf{V}}_g \tilde{\Theta}_g) = \nabla \cdot (\bar{\Phi}_g k_g \nabla \tilde{\Theta}_g) + H_{gs} + \bar{Q}_{gc}, \quad (4.35)$$

$$\frac{\partial}{\partial t}(\bar{\Phi}_s \rho_s C_{p,s} \tilde{\Theta}_s) + \nabla \cdot (\bar{\Phi}_s \rho_s C_{p,s} \tilde{\mathbf{V}}_s \tilde{\Theta}_s) = \nabla \cdot (\bar{\Phi}_s k_s \nabla \tilde{\Theta}_s) - H_{gs} + \bar{Q}_{sc}. \quad (4.36)$$

In addition to the newly developed constitutive model for cylinder-suspension heat transfer, we also include a known heat transfer correlation in the gas-phase energy equation [92]. This allows for calculation of heat transfer in the freeboard where no solids may be present. It is implemented similarly to the cylinder-suspension model,

$$\bar{Q}_{gc} = \bar{h}_{gc} A_c (T_c - \bar{T}_g), \quad (4.37)$$

where \bar{h}_{gc} is the filtered gas-cylinder heat transfer coefficient and is calculated from the Nusselt correlation developed by Khan et al. [92]. It is important to note that both of these models operate on the uncorrected variables, $\bar{\phi}_i$, $\tilde{\mathbf{v}}_i$, and \tilde{T}_i .

For both source terms the area is calculated by the ratio of unit cell area to grid cell area,

$$A'_{c_i} = \frac{\Delta_x \Delta_y}{a_c^2} \pi D_c, \quad (4.38)$$

where A'_{c_i} is the area for a single computational cell and Δ_x and Δ_y are cell lengths in the x and y direction. Because the model has been developed, implemented, and tested in 2D, the area calculation is actually 1D (the circumference of the cylinder).

4.7 Verification

To ensure the new model performs well under a wide range of mixed conditions, we performed several verification tests comparing the model formulation to steady-state, high-resolution simulations (Section 4.7.1), and comparing the implemented model

Table 4.3: Model verification input parameters distributions.

Variable	Distribution	Units
$\bar{\phi}_s$	$\mathcal{U}(0.01, 0.6)$	
D_c	$\mathcal{U}(0.95, 4.5)$	cm
a_c	$\mathcal{U}(6, 12)$	cm
d_p	$\mathcal{U}(50, 350)$	μm
$C_{p,s}$	$\mathcal{U}(500, 4000)$	J/kg·K

with transient, high-resolution simulations (Section 4.7.2).

4.7.1 Model form

Using the same periodic unit-cell geometry from Section 4.5, we design a campaign of simulations to evaluate our heat transfer model for combinations of $\bar{\phi}_s$, D_c/a_c , $|\tilde{\mathbf{v}}_s|/v_t$, and $\overline{\text{Pe}}_{cs}$ values that were not included in the development of the model. To provide thorough coverage of the variables' state space, nearly orthogonal Latin hypercube (NOLH) sampling is used to design the set of 15 experiments [93, 94]. The NOLH values are sampled from the distributions listed in Table 4.3. The complete list of sampled values for the verification campaign are presented in Table 4.4.

Table 4.4: Model verification input parameters, sampled using nearly orthogonal Latin hypercube sampling [93, 94].

n	$\bar{\phi}_s$	D_c/a_c	$ \tilde{\mathbf{v}}_s /v_t$	$\overline{\text{Pe}}_{cs}$
1	0.6	0.396	2.07	4,880
2	0.56	0.173	0.653	60,200
3	0.53	0.4	1.85	9,850
4	0.49	0.417	0.0798	5,370,000
5	0.45	0.139	0.533	3,140,000
6	0.38	0.351	0.435	303,000
7	0.34	0.237	6.38	85.7
8	0.3	0.357	0.608	155,000
9	0.23	0.138	2.44	30,500
10	0.19	0.171	0.353	627,000
11	0.16	0.43	3.66	582
12	0.12	0.251	21.9	16.8
13	0.08	0.27	0.386	885,000
14	0.05	0.33	0.93	148,000
15	0.01	0.306	0.209	530,000

Each simulation was run for 10 seconds, and post processed to calculate the observed (i.e., MFIX simulation) and predicted (i.e., subgrid model equation (4.30)) filtered Nusselt numbers and their uncertainties (only calculated for the simulation results). Results are shown on a log-log plot (Figure 4.9) to fit the large range of data. Overall there is good agreement with the predicted values, with few outliers and no obvious correlations associated with them.

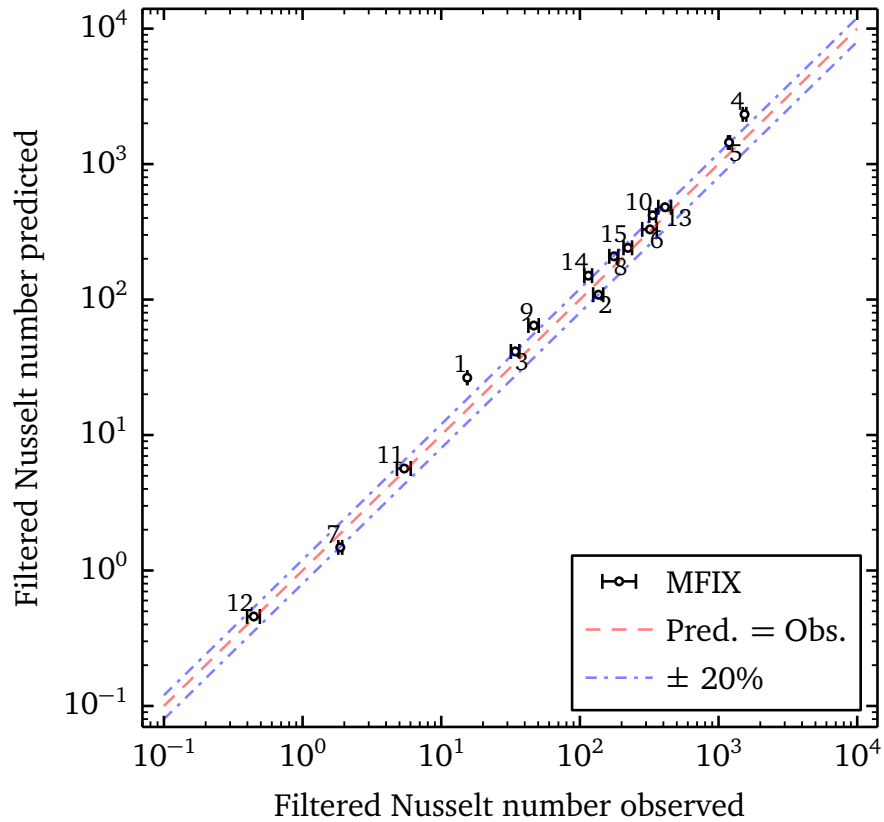


Figure 4-9: Model verification results showing predicted vs. observed filtered Nusselt numbers. Circles and numbers correspond to the parameter input combinations in Table 4.4. The light-red dashed line represents an exact match, and the light-blue dashed-dotted lines represent $\pm 20\%$ bands.

4.7.2 Implemented model

To verify the numerical integrity of the implemented subgrid model, we consider 2 small-scale test cases and compare the transient and steady state behaviors. The domains are similar to the domain described in Section 4.5. Highly-resolved simulations are used as the “control” simulations, while coarse-grid simulations are used to demonstrate the necessity of subgrid models. These domains are described in detail below.

Case 1: Simple cooling

The first case consists of a square periodic domain measuring $3\text{ cm} \times 3\text{ cm}$. Cylinders measuring 1 cm in diameter are spaced 1.5 cm apart within the domain (Figure 4.10). A mixture of 70% gas and 30% solids occupies the empty region in the system, initialized at $30\text{ }^\circ\text{C}$. The cylinder walls are held at a constant temperature of $20\text{ }^\circ\text{C}$. A pressure gradient Δp_g is imposed along the y-direction, opposing gravity, to drive the flow. This gradient is adjusted to achieve a mean flow velocity of 0.5 m/s. The system is simulated for 10 seconds, allowing it to reach 90% of thermal steady state. Material properties are reported in Table 4.5.

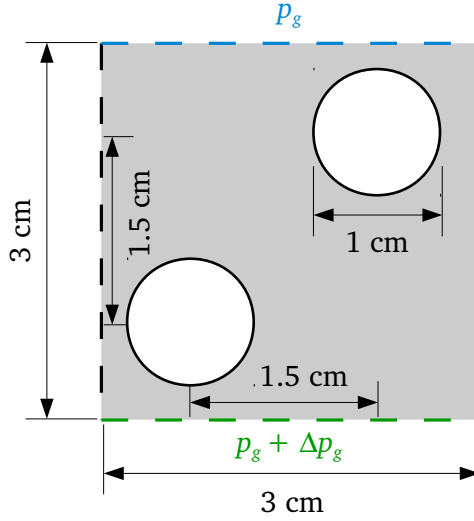


Figure 4-10: Simulation domain schematic for verification Case 1. Domain boundaries are periodic and a pressure gradient is imposed along the y-direction.

To demonstrate the effects of the grid-dependence and subgrid models, we consider three configurations: a) highly-resolved grid, $\Delta_{\text{grid}}^{\text{high-res.}}/d_p = 2$, where the cylinders and transport phenomena are fully resolved, b) coarse-grid, $\Delta_{\text{grid}}^{\text{coarse}}/d_p = 8$, where the cylinders are explicitly resolved; however, the physics are no longer converged, and c) coarse-grid with the subgrid model, $\Delta_{\text{subgrid}}^{\text{coarse}}/d_p = 8$, where the cylinders are modeled as an effective porous media and the transport phenomena are corrected using subgrid models. Figure 4-11 shows the meshes for the respective configurations.

The results are presented in Figure 4-12. The control case follows an expected

Table 4.5: Material properties for verification Case 1.

Parameter	Gas	Solids	Units
Density	1.3	441	kg/m ³
Viscosity	$1.8 \cdot 10^{-5}$		m ² /s ²
Diameter		200	μm
Thermal conductivity	0.024	0.2	W/m·K
Specific heat capacity	1150	2000	J/kg·K

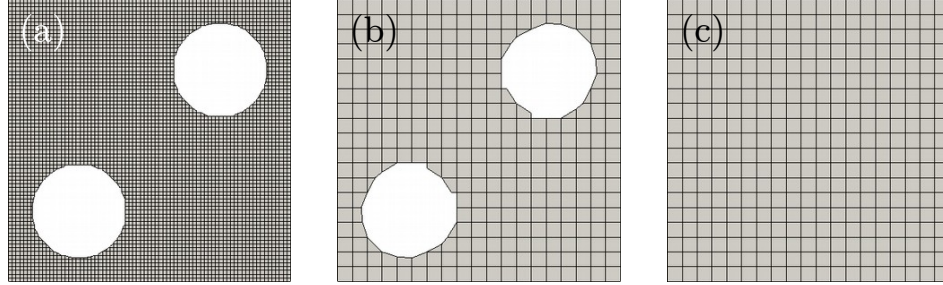


Figure 4.11: Simulation domains and meshes for verification Case 1: (a) high-resolution, “control” case, explicitly modeling the cylinders and fully resolving the heat transfer, $\Delta_{\text{grid}}^{\text{high-res.}}/d_p = 2$; (b) coarse-grid, explicitly modeling the cylinders, no longer fully resolving the heat transfer, $\Delta_{\text{grid}}^{\text{coarse}}/d_p = 8$; and (c) coarse-grid with subgrid model, $\Delta_{\text{subgrid}}^{\text{coarse}}/d_p = 8$.

exponential-decay cooling curve, reaching approximately 90% of steady-state by 10 seconds. When the grid is coarsened and no subgrid model is used, we observe significantly different transient behavior. While the system tends to the same steady-state (dictated by the cylinders’ temperature), the time-scale is significantly different, showing under-prediction of the heat transfer rates. Substituting the subgrid model for the cylinders, we are able to match the transient temperature profile of the high-resolution simulation very well within a 95% confidence interval, shown by the shaded regions.

The control system took 15 hours \times 16 processors = 240 CPU hours to simulate. The coarse-grid system only took 0.6 hours \times 4 processors = 2.4 CPU hours. And the subgrid system fell in between, taking 1 hour \times 4 processors = 4 CPU hours. The time difference between the coarse-grid and the subgrid system is negligible, but the difference in simulation results are very significant. We achieve almost identical results compared to the high-resolution simulation for 1/60 of the computation time.

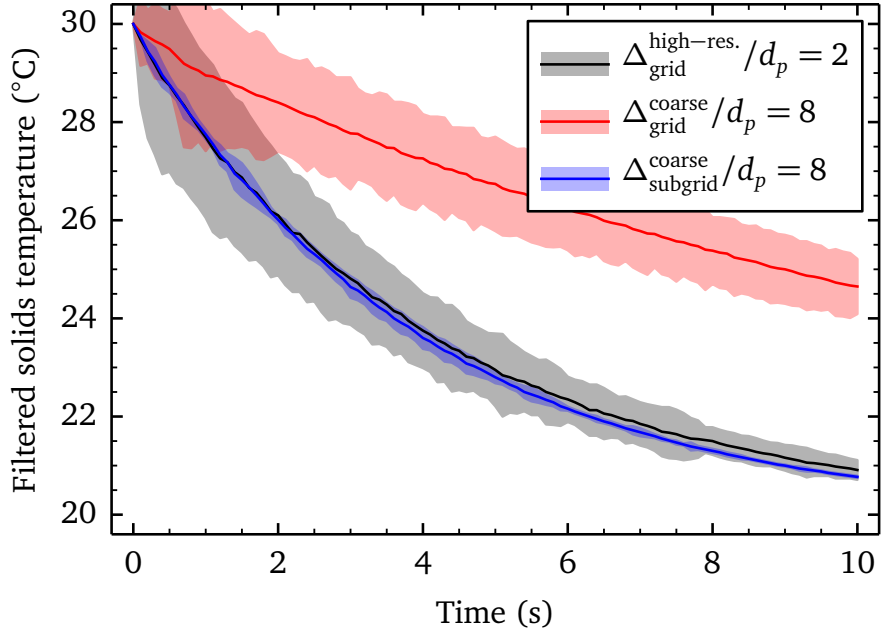


Figure 4-12: Temperature profiles from verification Case 1. Shaded regions represent 95% confidence regions.

Case 2: Cooling with heat generation

The second case uses a similar setup to Case 2 (Section 4.7.2). The domain measures $12 \text{ cm} \times 12 \text{ cm}$ with 3 cm diameter cylinders spaced 6 cm apart, held at $20 \text{ }^\circ\text{C}$. The domain is initialized with a 70/30% mixture of gas and solids, respectively, at $20 \text{ }^\circ\text{C}$. The pressure gradient is set to achieve a mean field velocity of 0.5 m/s. To simulate an exothermic gas-solids reaction, a generation term is added to the solids, heating the system at a rate of $\Pi_s = 1 \text{ }^\circ\text{C/s}$. Material properties are tabulated in Table 4.6.

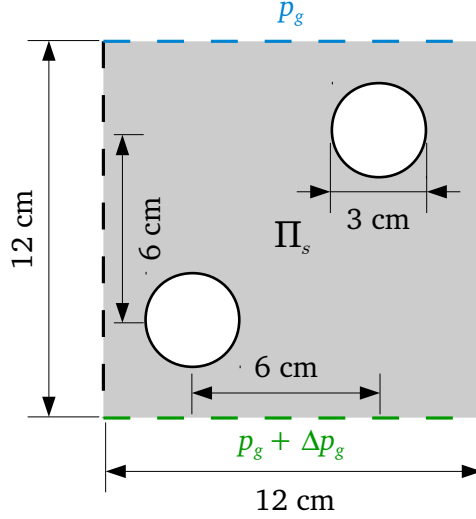


Figure 4-13: Simulation domain schematic for verification Case 2. Domain boundaries are periodic and a pressure gradient is imposed along the y-direction. Cylinder walls are held at $T_s = 20^\circ$ and a heat generation is added to the solids, $\Pi_s = 1K/s$.

Similar to Case 1, we consider three meshes for the system: a) high-resolution grid, $\Delta_{\text{grid}}^{\text{high-res.}}/d_p = 4$, b) coarse-resolution grid (with cylinders), $\Delta_{\text{grid}}^{\text{coarse}}/d_p = 32$, and c) coarse-resolution grid with subgrid model, $\Delta_{\text{subgrid}}^{\text{coarse}}/d_p = 32$, shown in Figure 4-14.

The results from Case 2 (Figure 4-15) are even more pronounced than those from Case 1 (Figure 4-12). The control system heats up due to the included generation term. After 50 seconds it has reached 99% steady state, equilibrating near 35°C . The coarse-grid simulation without a subgrid model, again, under predicts the cylinder-

Table 4.6: Material properties for verification Case 2.

Parameter	Gas	Solids	Units
Density	1.2	441	kg/m^3
Viscosity	$1.8 \cdot 10^{-5}$		m^2/s^2
Diameter		100	μm
Thermal conductivity	0.024	0.2	$\text{W/m}\cdot\text{K}$
Specific heat capacity	1000	1000	$\text{J/kg}\cdot\text{K}$

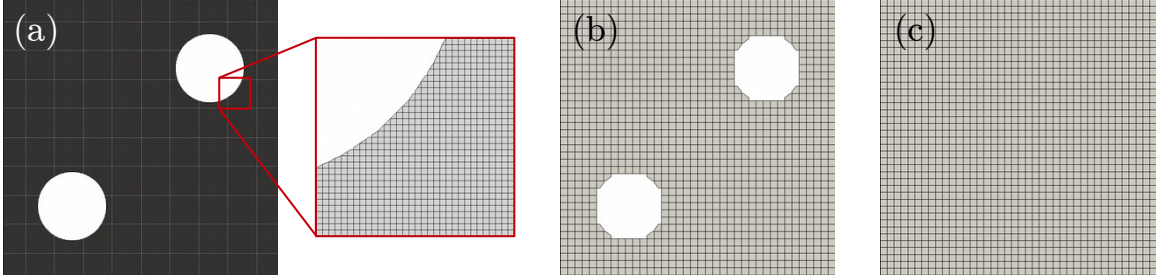


Figure 4-14: Simulation domains and meshes for verification case 2: (a) high-resolution, “control” case, explicitly modeling the cylinders and fully resolving the heat transfer, $\Delta_{\text{grid}}^{\text{high-res.}}/d_p = 4$; (b) coarse-grid, explicitly modeling the cylinders, no longer fully resolving the heat transfer, $\Delta_{\text{grid}}^{\text{coarse}}/d_p = 32$; and (c) coarse-grid with subgrid model, $\Delta_{\text{subgrid}}^{\text{coarse}}/d_p = 32$.

suspension heat transfer in the system. The domain continues to heat up and would take approximately 360 seconds to reach an equilibrium temperature of 93 °C. Comparitively, the subgrid model does an excellent job tracking the transient and steady state behavior, equilibrating near 38 °C, falling just outside the 95% confidence interval of the control simulation. The percent different between the two is approximately 20%. While this may seem like a large error, typical Nusselt correlations are often cited as only being accurate with $\pm 20\%$.

We observed similar performance gains compared to Case 1. The control system took 110 hours \times 16 processors = 1760 CPU hours to simulate. The coarse-grid system only took 2.9 hours \times 4 processors = 11.6 CPU hours. For this system, the subgrid system beat the coarse-grid model, taking only 1.6 hours \times 4 processors = 6.4 CPU hours. The subgrid system outperforms the coarse-grid system both in time and accuracy and achieves similar results compared to the high-resolution simulation for 1/275 of the computation time.

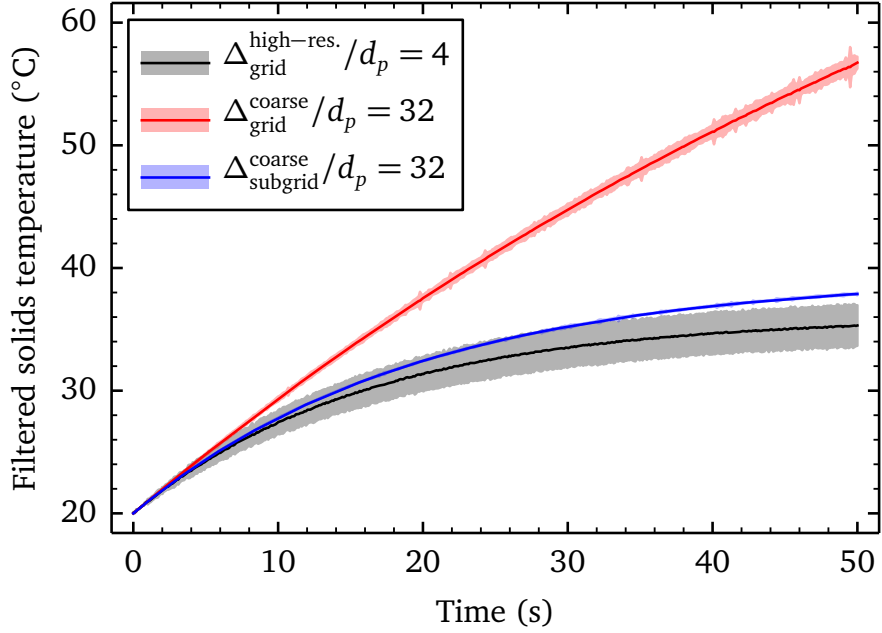


Figure 4-15: Temperature profiles from verification Case 2. Shaded regions represent 95% confidence regions.

It is important to note that due to the way the subgrid model is developed and implemented, the same filtered Nusselt number will always be returned for a given system (provided the input parameters: $\bar{\phi}_s$, D_c/a_c , $|\tilde{\mathbf{v}}_s|/v_t$, and $\overline{\text{Pe}}_{cs}$, remain constant). However, based on the previous results, it is obvious that without the subgrid models, the filtered Nusselt number is grid-dependent and can be unphysical. This is further demonstrated in Figure 4-16, where the subgrid value for $\overline{\text{Nu}}_{cs}$ remains constant across all grid sizes while the regular simulations show decreasing filtered Nusselt numbers as the grid size increases.

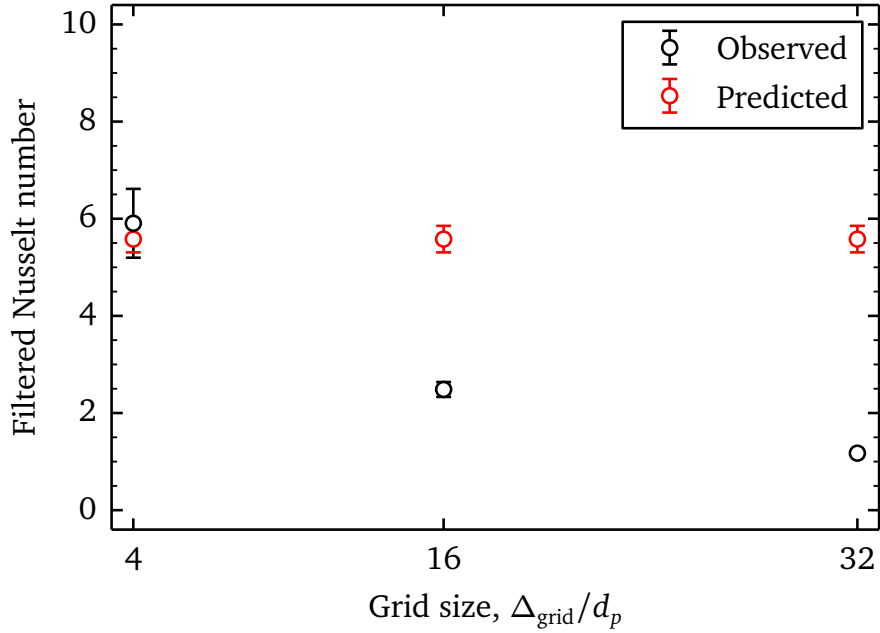


Figure 4-16: Filtered Nusselt number vs grid size for Case 2, comparing the subgrid model prediction versus the observed (simulated) values.

4.8 Validation

To ensure the subgrid models function well in general applications (as opposed to small, periodic domains) we consider two large scale validation cases, borrowed from Sarkar et al. [15]: a bubbling fluidized bed and a turbulent fluidized bed. The geometry, operating conditions (Table 4.7), and material properties (Table 4.8) were replicated from Sarkar et al., with the exception of the heat transfer conditions and properties, which were not considered in Sarkar et al.’s work. The bubbling bed is set up as active cooling, with a heated gas inlet at 30 °C along the bottom and a constant cylinder temperature of 20 °C. Conversely, the turbulent bed is set up as active heating, where the gas-inlet is cool (20 °C) and the cylinders are held at 30 °C. The different flow regimes (i.e., gentle bubbling vs. turbulent) coupled with the different heating/cooling configurations provide extreme cases for validation.

Table 4.7: Geometry, initial conditions, and boundary conditions for the bubbling and turbulent bed validation cases.

Parameter	Bubbling	Turbulent	Units
Width \times height	1.2×1.0	0.9×1.8	m
Cylinder diameter	0.03	0.03	m
Cylinder spacing	0.1	0.1	m
Cylinder temperature	20	30	$^{\circ}\text{C}$
Initial bed height	0.7	1.3	m
Initial solids fraction	50	20	%
Initial bed temperature	20	30	$^{\circ}\text{C}$
Gas inlet velocity	0.022	0.19	m/s
Gas inlet temperature	30	20	$^{\circ}\text{C}$
Outlet pressure	101	101	kPa
Cell size (high-res.)	600	600	μm
Subgrid cell sizes	4.8, 9.6 19.2, 38.4	4.8, 9.6 19.2, 38.4	cm

Table 4.8: Material properties for the bubbling and turbulent bed validation cases.

Parameter	Gas	Solids	Units
Density	1.142	441	kg/m^3
Viscosity	$2 \cdot 10^{-5}$		m^2/s^2
Diameter		100	μm
Terminal velocity		0.27	m/s
Thermal conductivity	0.026	0.2	$\text{W}/\text{m}\cdot\text{K}$
Specific heat capacity	1040	830	$\text{J}/\text{kg}\cdot\text{K}$

4.8.1 Bubbling bed

The bubbling bed case was simulated for 100 seconds for all grid sizes. The initial state of the systems can be seen in Figure 4.18. Time-averaged temperature fields are shown in Figure 4.19. The elapsed time and required resources for the simulations are listed in Table 4.9. The high-resolution model took more than 10,000 times longer to simulate, compared to the slowest subgrid system; however, we noticed large discrepancies between the two systems when near the inlet boundary.

Table 4.9: Simulation benchmark timing for the bubbling bed case.

System	Hours	Processors	CPU Hours
$\Delta_{\text{grid}}^{\text{high-res.}}/d_p = 4$	900	63	56,500
$\Delta_{\text{subgrid}}^{\text{coarse}}/d_p = 32$	2.0	16	32.0
$\Delta_{\text{subgrid}}^{\text{coarse}}/d_p = 64$	1.9	4	7.6
$\Delta_{\text{subgrid}}^{\text{coarse}}/d_p = 128$	0.9	4	3.6
$\Delta_{\text{subgrid}}^{\text{coarse}}/d_p = 256$	0.5	4	2.0

The temperature field was averaged over time and then again across the horizontal direction to produce a temperature profile along the vertical direction. These profiles were compared across all systems to quantify the accuracy of the subgrid model (Figure 4.20). We see the subgrid systems all follow a similar trend: near the boundary the temperature is higher and it decays as we move away from the boundary until we reach approximately $y = 0.2$ m, at which point the remaining profile is constant. This differs from the high-resolution which has a much faster decay rate. The high-resolution system has a high temperature near the boundary, but by $y = 0.02$ m the profile is no longer changing. This discrepancy is attributed to the implementation of the boundary condition.

MFIX implements boundary conditions via ghost cells. That is, there is a hidden

layer of grid cells surrounding the entire domain to enforce the boundary conditions. For example, hot air ($T_g = 30\text{ }^\circ\text{C}$) is being injected into the bottom of the system. To satisfy the boundary condition of the temperature, the average temperature of the ghost-cell and the grid-cell next to the wall must be equal to the boundary condition. As a result we observe fast “diffusion” of heat to the first row of grid cells. This energy is passed between phases and moves through the system, eventually being dissipated; however, because of the physical size of the grid cells, the dissipation covers a larger distance (e.g., 0.2 m vs. 0.02 m).

The other observable discrepancy is also related to the boundary condition: the larger the subgrid cells, the lower the temperature value at the cell next to the boundary. The high-resolution model is closest to the boundary condition ($T_g = 30\text{ }^\circ\text{C}$) and as the grid is coarsened, the value in wall-cell decreases. This is also believed to be a product of the grid size, where large grid cells will have a lower temperature change for a given amount of energy, compared to a smaller grid cell as it can spread the energy out.

Both of these discrepancies are unavoidable as they are byproducts of the numerical methods and the subgrid size. However, the second discrepancy can be minimized by using local grid refinement along the boundaries. Figure 4-17 shows an example of the $\Delta_{\text{subgrid}}^{\text{coarse}}/d_p = 128$ system with the wall-cell continuously split in half until the wall-cell was $\Delta_{\text{subgrid}}^{\text{wall}}/d_p = 4$. This system was run for 100 seconds, taking only slightly longer than its’ unrefined counterpart, 0.9 vs. 0.8 CPU hours. The temperature profile results are shown in Figure 4-21. The temperature profile of the refined mesh show significantly better agreement with the finer coarse grid: achieving a higher wall-cell temperature and dissipating the heat earlier, by approximately 0.15 m.

While these discrepancies may seem large, it is important to remember the goal of this model: to simulate large-scale systems for design optimization. These methods

will certainly allow rapid prototyping of designs and exploration of variables, with minimal data loss.

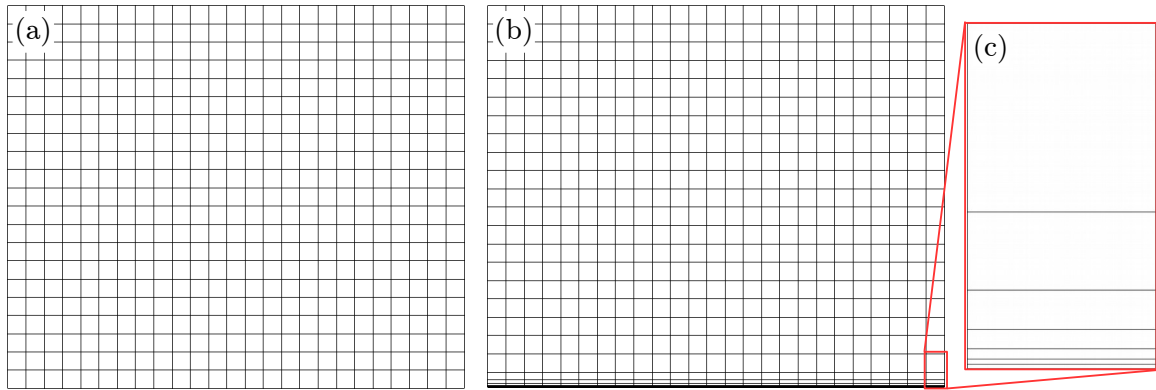


Figure 4-17: Local grid refinement along the boundary to capture the inlet conditions.

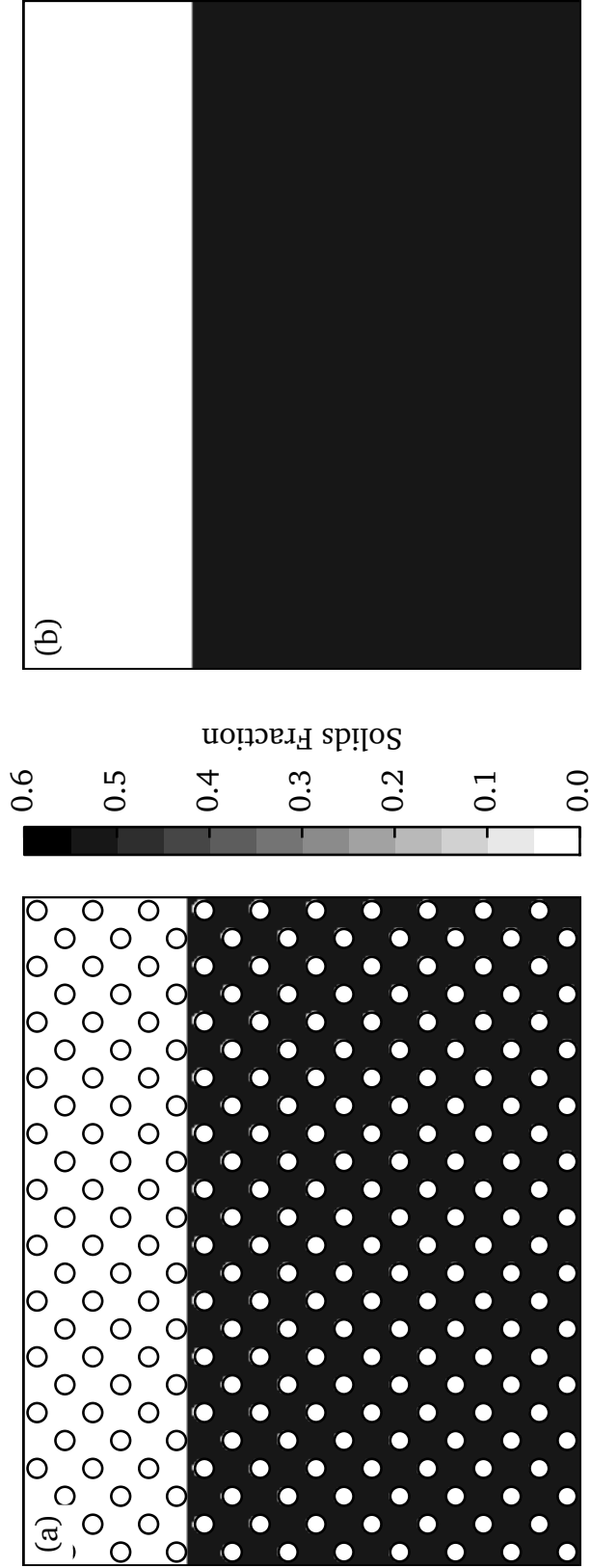


Figure 4-18: Initial bed height (solids fraction) for a) high-resolution case, $\Delta_{\text{grid}}^{\text{high-res.}}/d_p = 4$ and b) coarse subgrid case, $\Delta_{\text{subgrid}}^{\text{coarse}}/d_p = 128$.

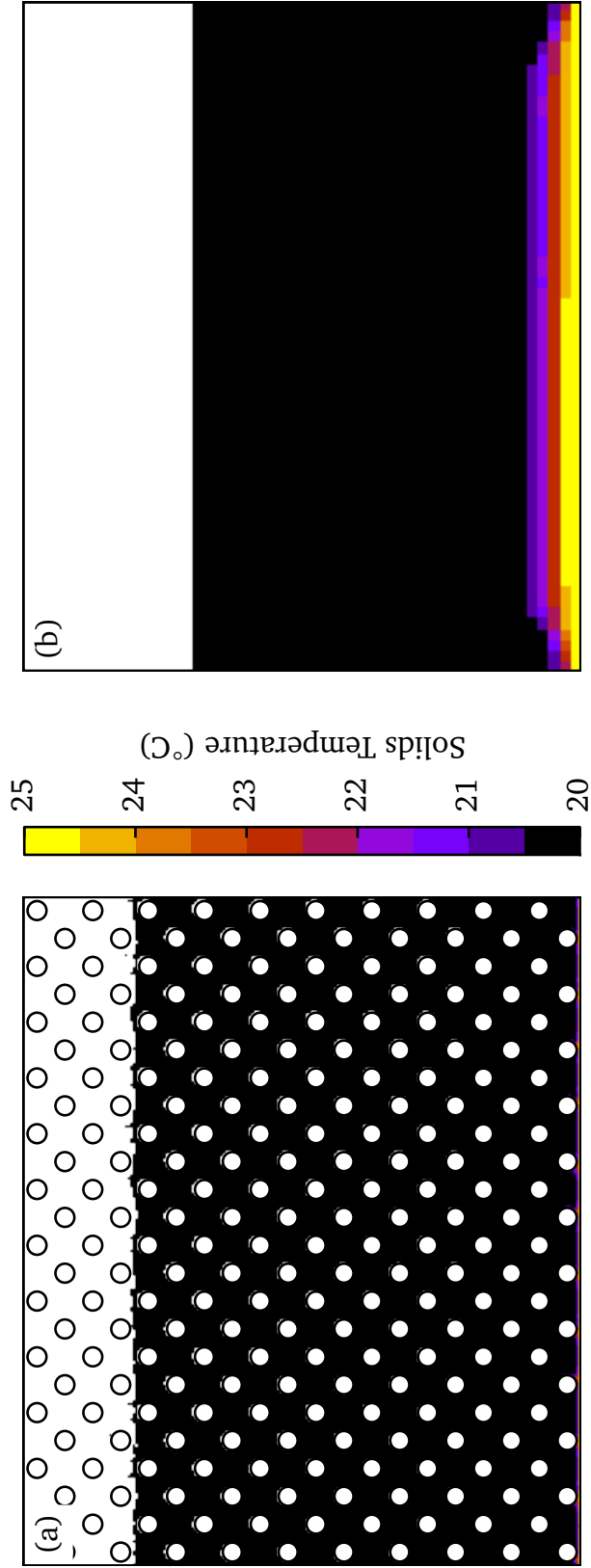


Figure 4.19: Average temperature fields for a) high-resolution case, $\Delta_{\text{grid}}^{\text{high-res.}}/d_p = 4$ and b) coarse subgrid case, $\Delta_{\text{subgrid}}^{\text{coarse}}/d_p = 128$.

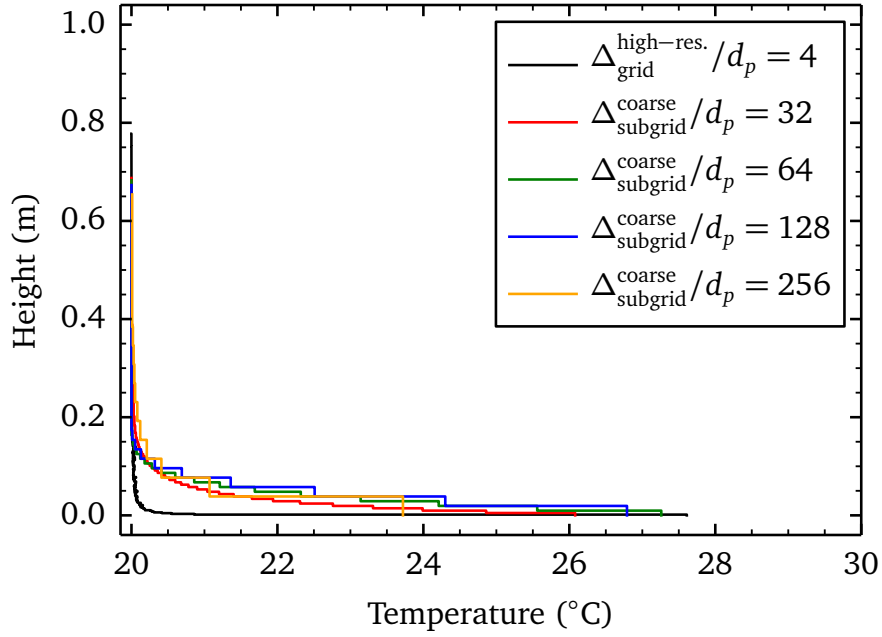


Figure 4-20: Temperature profiles for the bubbling bed along the height, averaged across the width for 100 seconds of simulation.

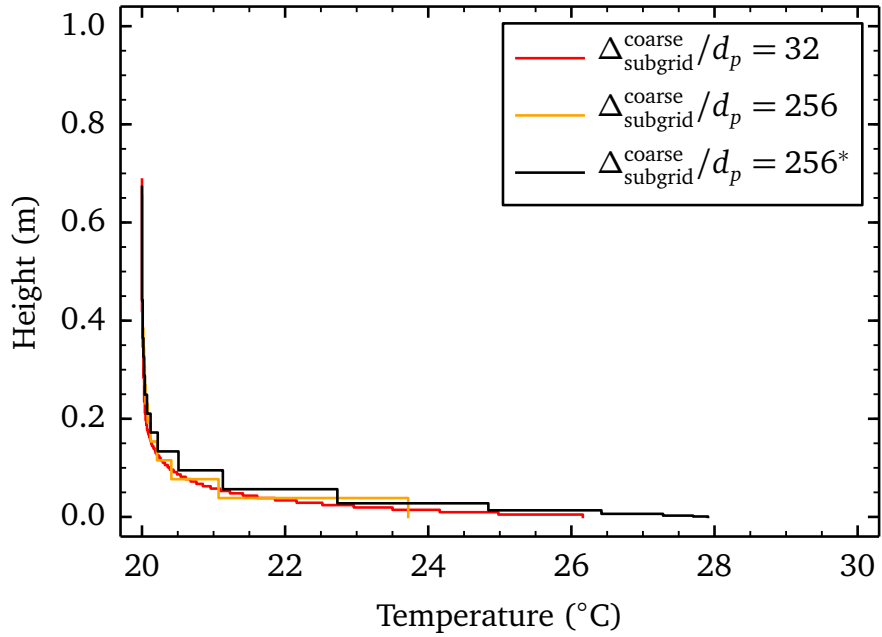


Figure 4-21: Temperature profiles for the bubbling bed along the height, averaged across the width for 100 seconds of simulation. The asterisk denotes the use of local grid-refinement near the inlet boundary.

4.8.2 Turbulent bed

The turbulent bed case was also simulated for 100 seconds; however, due to computational resources and time limitations, the high-resolution case could only be simulated for 20 seconds. The increased Simulation run times are tabulated in Table 4.10. The high-resolution system takes approximately 80 times longer to simulate than the smallest subgrid system, and about 138,000 times longer than the coarse subgrid system. Figure 4.22 shows the initial conditions and the temporally averaged (over 20 seconds) temperature field for the high-resolution and the subgrid system ($\Delta_{\text{subgrid}}^{\text{coarse}}/d_p = 128$). Similar to the bubbling bed case, we observe discrepancies near the boundary.

The temperature profiles averaged over the first 20 seconds show excellent agreement between the high-resolution system and all subgrid systems (Figure 4.23). The wall-cells at the boundary exhibit different behavior than those in the bubbling bed case. The high-resolution system wall-cells tend toward the boundary condition ($T_g = 20\text{ }^\circ\text{C}$), while the subgrid wall-cells tend toward the boundary condition as the grid is coarsened, contrary to the bubbling bed case.

The subgrid systems were then averaged over the entire 100 seconds to compare steady-state profiles in a turbulent regime (Figure 4.24). An additional subgrid system with local grid-cell refinement near the inlet boundary was included for comparison. With the refined system we see a much better agreement with the boundary condition, with the wall cells very near $20\text{ }^\circ\text{C}$. However, a new discrepancy is also evident from this figure: the bed height (denoted by the maximum height of the profile) for the $\Delta_{\text{subgrid}}^{\text{coarse}}/d_p = 64$ system is significantly lower than the other profiles. This is also visible in Figure 4.23. This difference is related to the subgrid model for the cylinder-suspension drag, not the heat transfer model, but it could be the cause of some of the other discrepancies identified. The subgrid drag model may have additional limitations that are unknown or have not been explored at this point in time.

Similar to the bubbling bed, this validation case really exemplifies the need for subgrid models for heat transfer. By reducing the simulation time by over 100,000 times, the simulation can be run on a workstation within a few hours and return accurate results.

Table 4.10: Simulation timing for the turbulent bed case.

System	Hours	Processors	CPU Hours
$\Delta_{\text{grid}}^{\text{high-res.}}/d_p = 4$	4,580 ¹	72	330,000
$\Delta_{\text{subgrid}}^{\text{coarse}}/d_p = 64$	19	16	304
$\Delta_{\text{subgrid}}^{\text{coarse}}/d_p = 128$	1.0	4	4.0
$\Delta_{\text{subgrid}}^{\text{coarse}}/d_p = 256$	0.5	4	2.0

¹Because the system was only simulated for 20 seconds, the computation time was adjusted (extrapolated to 100 seconds) to remain comparable with the other systems.

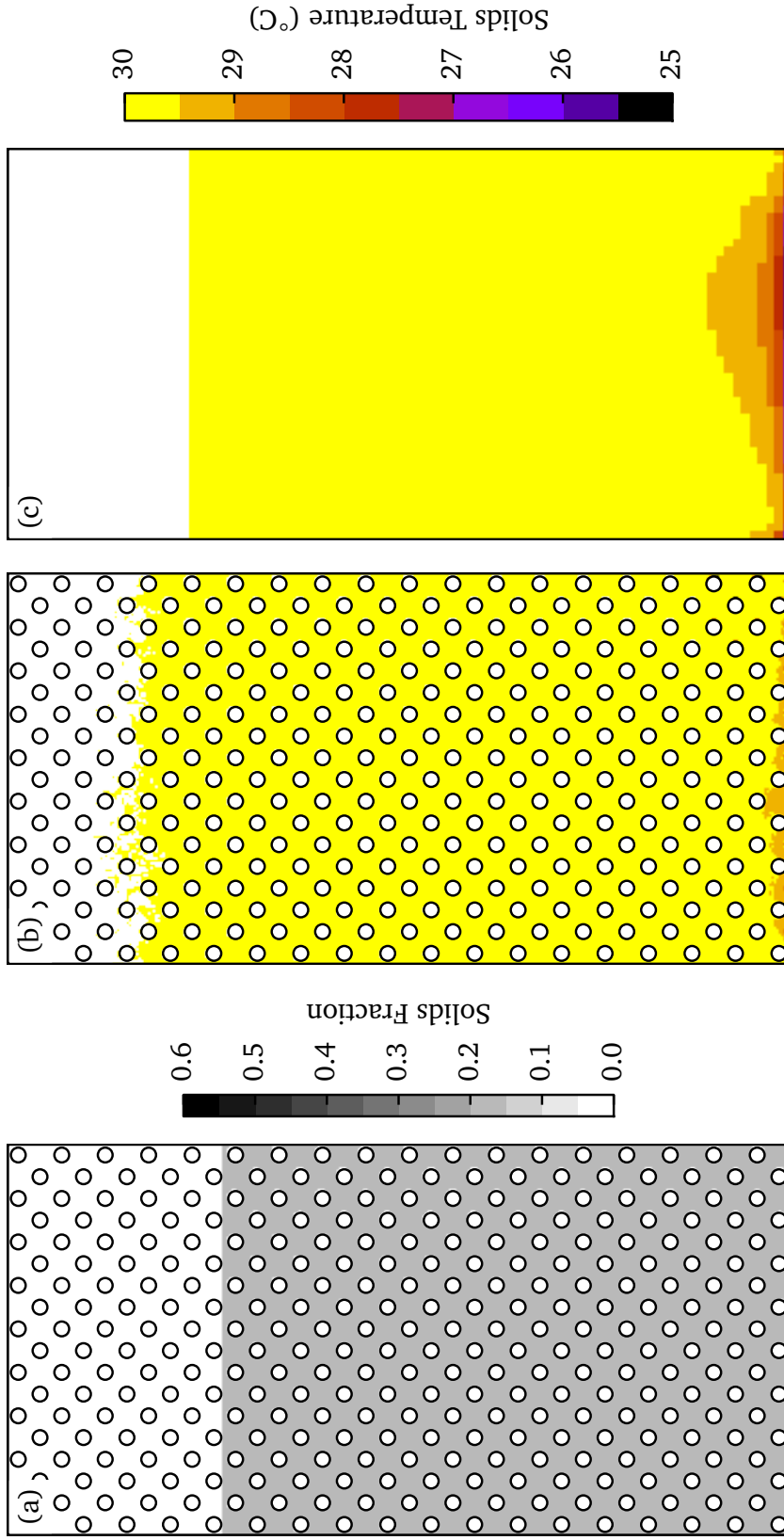


Figure 4-22: Turbulent bed simulation: a) initial bed height (solids fraction) for the high-resolution case, $\Delta_{\text{grid}}^{\text{high-res.}}/d_p = 4$, b) average temperature field for the high-resolution case, and c) average temperature field for the subgrid model, $\Delta_{\text{subgrid}}^{\text{coarse}}/d_p = 128$.

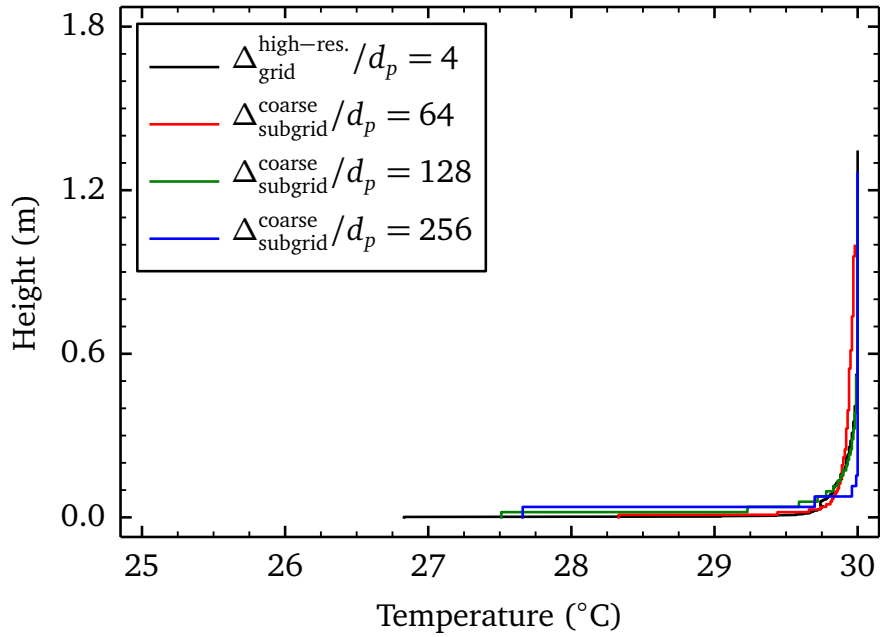


Figure 4-23: Temperature profiles for the turbulent bed along the height, averaged across the width for 20 seconds of simulation.

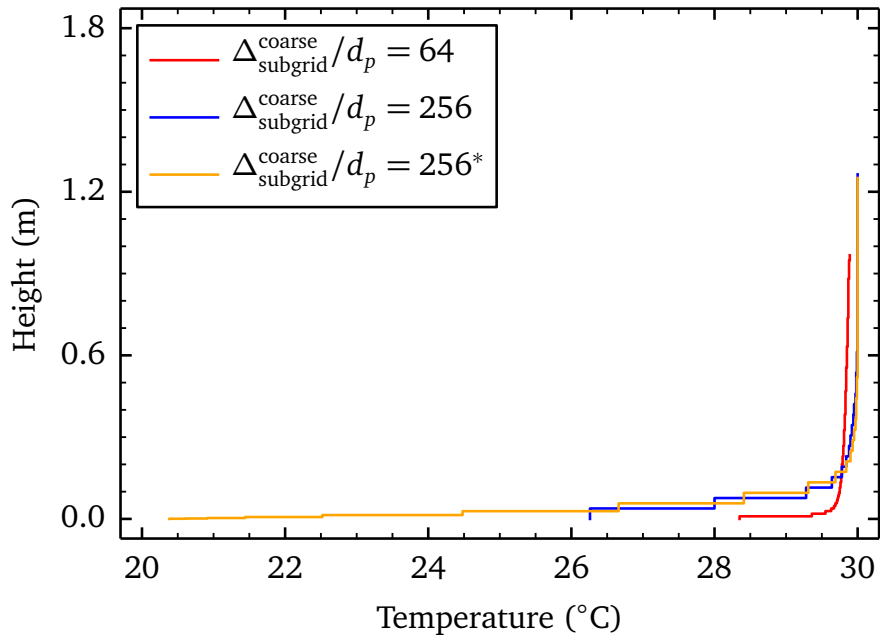


Figure 4-24: Temperature profiles for the turbulent bed along the height, averaged across the width for 100 seconds of simulation. The asterisk denotes the use of local grid-refinement near the inlet boundary.

4.9 Uncertainty Quantification

Quantifying the uncertainties and errors in the subgrid model requires a slightly different approach than that used in Chapter 3 because there is no experimental data available for the periodic sub-system we constructed. That eliminates the possibility of performing a calibration of the parameters; however, we can still quantify the sensitivity of the model and the prediction errors.

4.9.1 Sensitivity analysis

Similar to Section 3.1, we use a variance-based sensitivity analysis to estimate the effects of each parameter. First-order and total-effect Sobol indices [95, 96] are calculated using the Python package SALib [97]. Saltelli’s cross sampling method [98] is applied to uniform distributions for each variable, resulting in 50,000 parameter sets [97]. These sets are evaluated and their variance contributions calculated. The parameter distributions and resulting Sobol indices are listed in Table 4.11.

These results can be interpreted in the same manner as those presented in Section 3.1: the first-order indices indicated the amount of variance in the output that can be attributed to varying each parameter individually. Because there is no interaction between parameters, the first-order indices sum to 1. The total-effect indices

Table 4.11: First-order and total-effect Sobol indices measuring model sensitivity to parameters.

Parameter	Distribution	Sobol Indices	
		First-Order	Total-Effect
$\bar{\phi}_s$	$\mathcal{U}(0, 0.64)$	0.0614	0.0718
D_c/a_c	$\mathcal{U}(0, 0.5)$	0.249	0.275
$ \tilde{\mathbf{v}}_s /v_t$	$\mathcal{U}(0, 1.0)$	0.311	0.369
$\overline{\text{Pe}}_{cs}$	$\mathcal{U}(0, 2000)$	0.308	0.356

measure the total variance for a given parameter including interaction effects and as a result have a sum greater than 1. Because our results show minor differences between the first-order and total-effect indices, we can conclude that there are not significant interaction effects that are not being captured by the model. The ratio of cylinder diameter to spacing, dimensionless velocity, and Peclet number all have similar variances, contributing equally to the model variance, while the phase fraction accounts for only 6% of the model variation. This can be explained with Figure 4.5, where there is little change in Nusselt number once solids fraction is greater than 5%. However, the behavior below 5% solids is critical to accurate predictions in dilute regions, and as such, the solids fraction parameter can not be considered insignificant.

4.9.2 Model-prediction error

The proposed model from Section 4.5 can provide a point estimate for the filtered Nusselt number based on the input parameters; however, the model was regressed to minimize the squared residuals (noise). This noise can provide information about the error for a given point estimate. We use two methods to quantify this error and build confidence intervals around our subgrid model predictions: using MATLAB's non-linear prediction confidence interval function, `nlpredci`, and a bootstrapping method using SciPy's non-linear regression function `curve_fit` [90].

MATLAB's `nlpredci` function uses the non-linear regression model information, including the regression coefficient, residuals, and variance-covariance matrix to build confidence intervals. Figures 4.25–4.27 show 95% confidence intervals using this approach as blue dashed lines.

Secondary confidence regions were constructed using a bootstrap method. The original data was sampled at 80% of its' size to create a new data set. This new data set was regressed to the same form of the model (4.29) and plotted. These steps were repeated 1000 times (bootstrap realizations) to create an ensemble of solutions,

shown in Figures 4.25–4.27 as solid gray lines.

The results show excellent agreement between the two methods of confidence interval construction. If we denote these regions as the error in our predictions, then we can quantify that our filtered Nusselt number predictions are accurate within $\pm 5\text{--}15\%$ of the predicted value. This percent error compares well with errors reported in experimental and numerical calculations of Nusselt numbers/heat transfer coefficients [99–105].

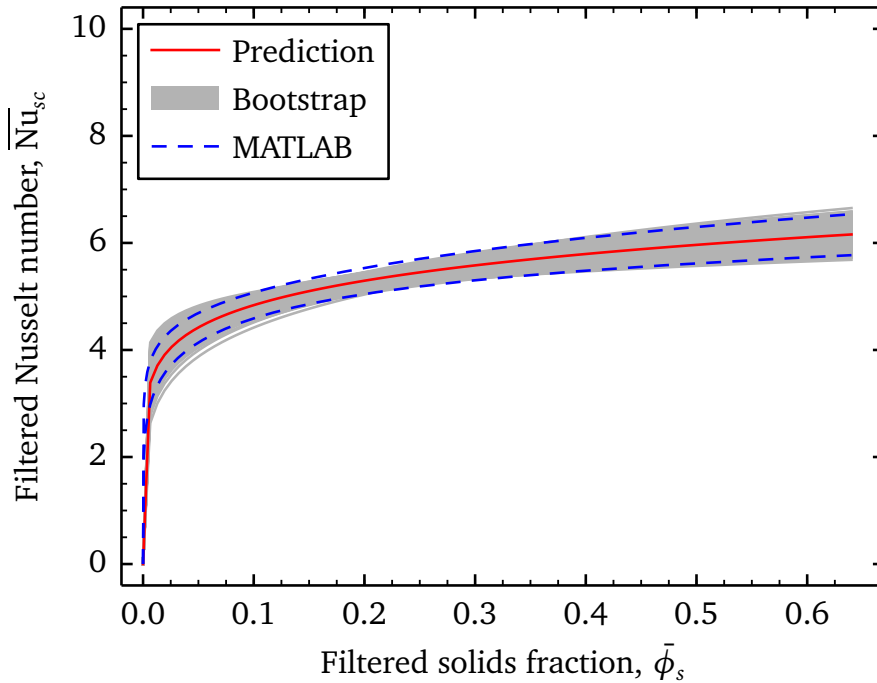


Figure 4.25: Filtered Nusselt number vs filtered solids fraction. Mean predicted values are shown as a red solid line with corresponding 95% confidence intervals shown as blue dashed lines (MATLAB). The ensemble of grey lines represents 1000 bootstrap realizations.

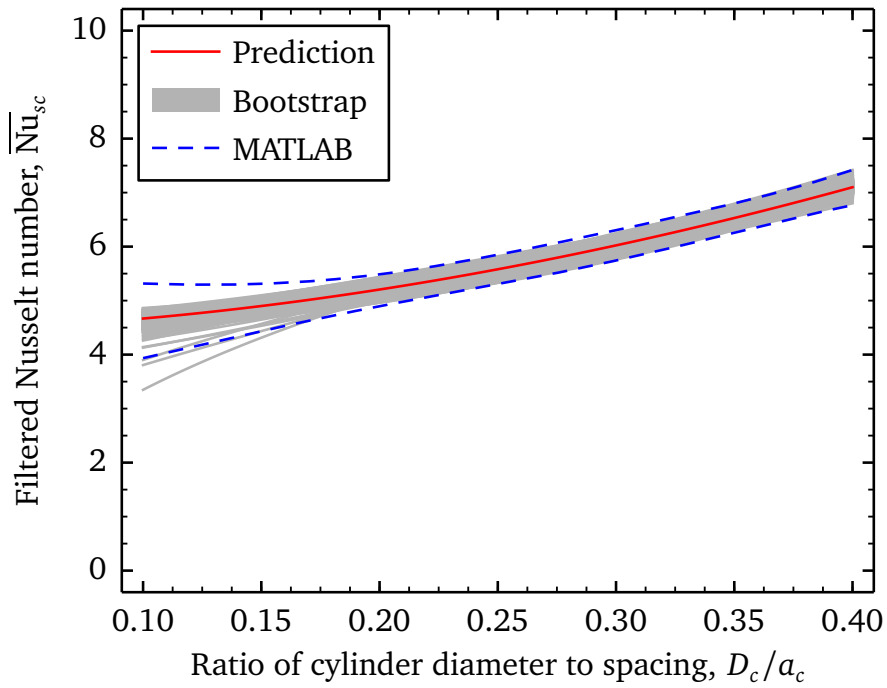


Figure 4·26: Filtered Nusselt number vs ratio of cylinder diameter to spacing. Mean predicted values are shown as a red solid line with corresponding 95% confidence intervals shown as blue dashed lines (MATLAB). The ensemble of grey lines represents 1000 bootstrap realizations.

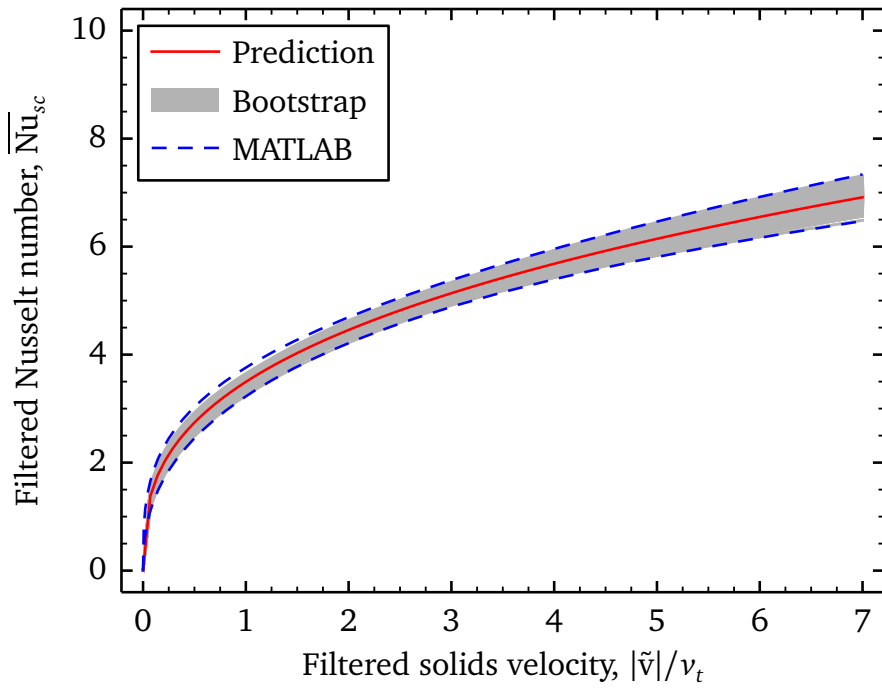


Figure 4-27: Filtered Nusselt number vs dimensionless filtered suspension velocity. Mean predicted values are shown as a red solid line with corresponding 95% confidence intervals shown as blue dashed lines (MATLAB). The ensemble of grey lines represents 1000 bootstrap realizations.

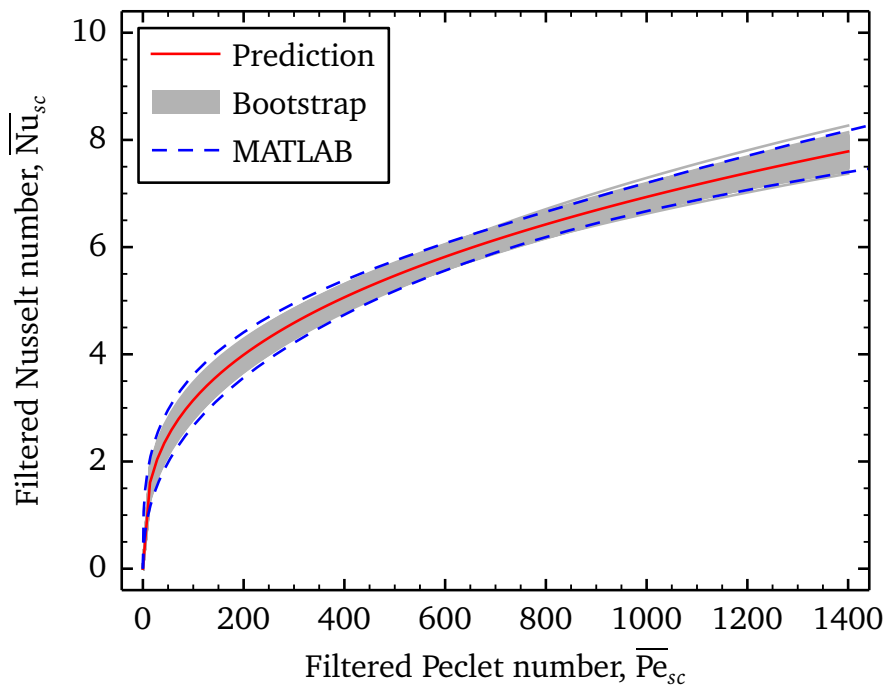


Figure 4.28: Filtered Nusselt number vs solids Peclet number. Mean predicted values are shown as a red solid line with corresponding 95% confidence intervals shown as blue dashed lines (MATLAB). The ensemble of grey lines represents 1000 bootstrap realizations.

Chapter 5

Carbon Capture System

With the unit problems validated, subgrid models developed, and validation of the laboratory-scale carbon capture unit finished [106], the next step in the hierarchy is a pilot-scale, 1 MW, fully reacting, carbon capture system (Chapter 3). Research on this system has been ongoing between Pacific Northwest National Laboratory and the National Energy Technology Laboratory, who have attempted to simulate the reactor using process models and CFD with an crude ad-hoc heat transfer model. For brevity, most details have been omitted but are available [107]; however, basic geometry and physical properties are described in Section 5.1.

5.1 Setup

The 1 MW carbon capture system measures 1.332 m wide by 6.884 m tall by 1.221 m deep (Figure 5-1a). For simplicity, we consider a 2D slice approximation of the system (Figure 5-1b/c). The system starts as an empty reactor with flue gas entering along the bottom. A mixture of neutral gas and fresh sorbent is constantly injected at the top of the downchute on the left. As time evolves the system fills up and reaches a side outlet, achieving a pseudo steady-state. As the fresh sorbent mixes with the flue gas, the CO_2 is adsorbed onto the particles and heat is given off, heating the surrounding gas-particle mixture. The system is simulated for 500 seconds and the hydrodynamics, heat transfer, and mass transfer rates are all investigated.

The geometry and basic boundary conditions are listed in Table 5.1. Due to the

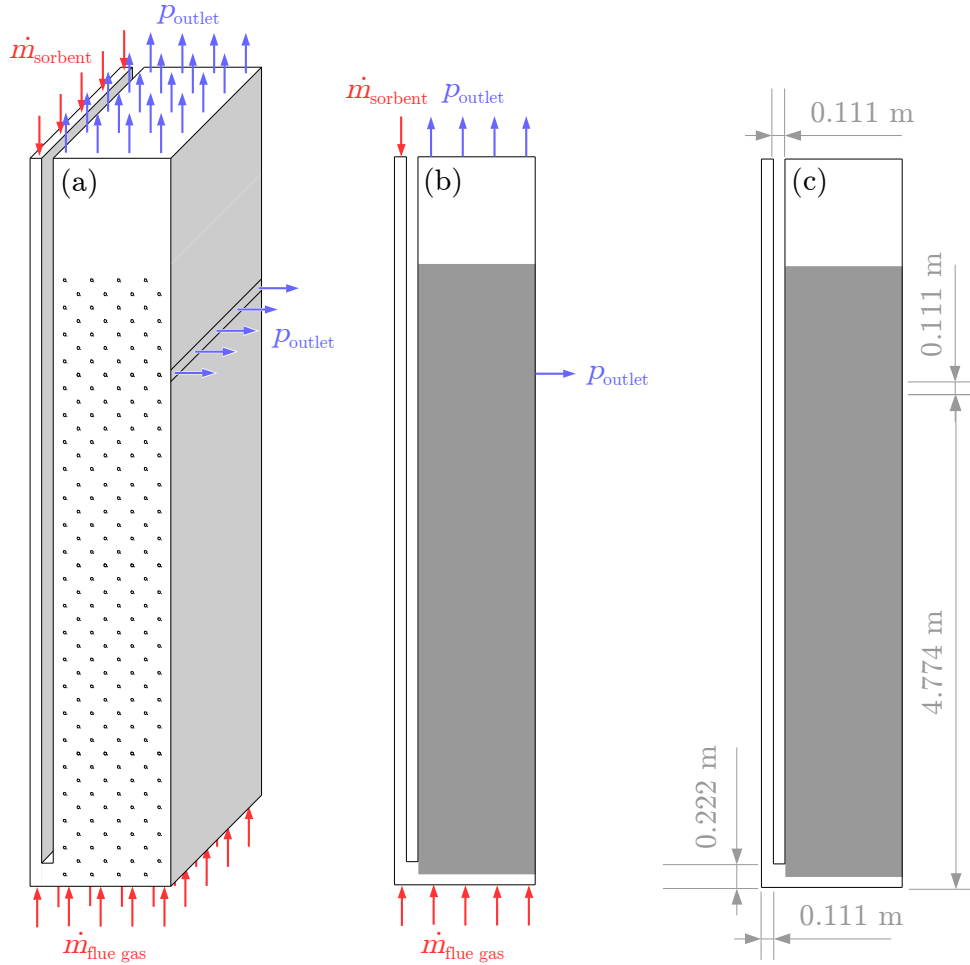


Figure 5-1: 1 MW carbon capture reactor: a) 3D geometry showing boundary conditions and immersed geometry, b) 2D slice approximation showing effective cylinder area, and c) dimensions of downchute and pressure outlet.

size of the system it is not possible to simulate a high-resolution version; we can only compare with the existing simulation results from previous attempts. Our model uses the subgrid model with a grid size of 3.7 cm, resulting in a mesh of 36×186 cells.

Some material properties are provided in Table 5.2; however, because it is a fully reacting system, the gas phase is a mixture of CO_2 , nitrogen (N_2), water vapor (H_2O), and oxygen (O_2), and thus some properties, such as density and heat capacity are constantly changing depending on the makeup. Similarly, the solid phase has 6 pos-

Table 5.1: Geometry and boundary conditions for the 1 MW carbon capture system.

Parameter	Value	Units
Width \times height	1.332×6.882	m
Cylinder diameter	0.01	m
Cylinder spacing	0.11	m
Cylinder temperature	32	$^{\circ}\text{C}$
Sorbent inlet mass flow rate	2.54	kg/s
Sorbent carrier-gas inlet mass flow rate	0.0066	kg/s
Sorbent/gas mixture inlet temperature	59	$^{\circ}\text{C}$
Flue gas inlet mass flow rate	0.6	kg/s
Flue gas inlet temperature	59	$^{\circ}\text{C}$
Outlet pressure	101	kPa
Cell size	3.7	cm

Table 5.2: Material properties for the 1 MW carbon capture system.

Parameter	Gas	Solids	Units
Density	varying	484	kg/m^3
Viscosity	$1.8 \cdot 10^{-5}$		m^2/s^2
Diameter		118	μm
Thermal conductivity	0.026	0.2	$\text{W}/\text{m}\cdot\text{K}$
Specific heat capacity	varying	varying	$\text{J}/\text{kg}\cdot\text{K}$

sible species: silicon dioxide, polyethyleneimines, carbamate ions, protonated amine, bicarbonate ions, and physisorbed water. The chemical reactions are described in detail in [107].

5.2 Results

Previous attempts to model the 1 MW reactor employed an ad-hoc model for the heat transfer via a stationary porous media the size of the tube bank, with porosity equal to the would-be area occupied by cylinders. The properties of the porous media

mimicked iron, with two important distinctions: the particle diameter was set equal to the cylinder diameter and a very large heat capacity was set to prevent heat transfer to the porous media. A constant temperature of 32 °C was set throughout the porous media. The results of this study are shown in Figure 5-2.

It is immediately obvious that this heat transfer model is insufficient. The porous media prevents mixing and over-predicts heat transfer rates, holding the entire region almost exactly at the boundary temperature, 32 °C, with no noticeable fluctuations. While it may be a computationally efficient method, it provides physically inaccurate results.

Using the same setup, we simulated the system with the subgrid heat transfer model. Because the subgrid model takes into account the local fluctuations of material properties and flow conditions, it provides more realistic, inhomogeneous flow fields, as shown in Figure 5-3b. We see that the flue gas enters the system and reacts immediately with the sorbent on the bottom of the reactor, generating heat that is dissipated moving upward through the bed. Additionally, we can see from Figure 5-3c that the adsorption process is working as designed, where most of the CO₂ is being adsorbed.

To evaluate the overall performance of the system, we averaged the field data over the 200–500 second interval (pseudo steady-state). The results show excellent behavior of the subgrid model (Figure 5-4b), where a smooth axial profile shows the active cooling in effect. The same averaging was applied to the solids fraction and CO₂ species fractions (Figure 5-4a and Figure 5-4c).

Lai et al. [107] reported abnormally high CO₂ capture rates: upwards of 99% of the CO₂ entering the system was being captured in the bed. Meanwhile, a process model of the same system was reporting capture rates around 80%. With our subgrid model, the initial simulations were still predicting 99% capture rates. However, it was

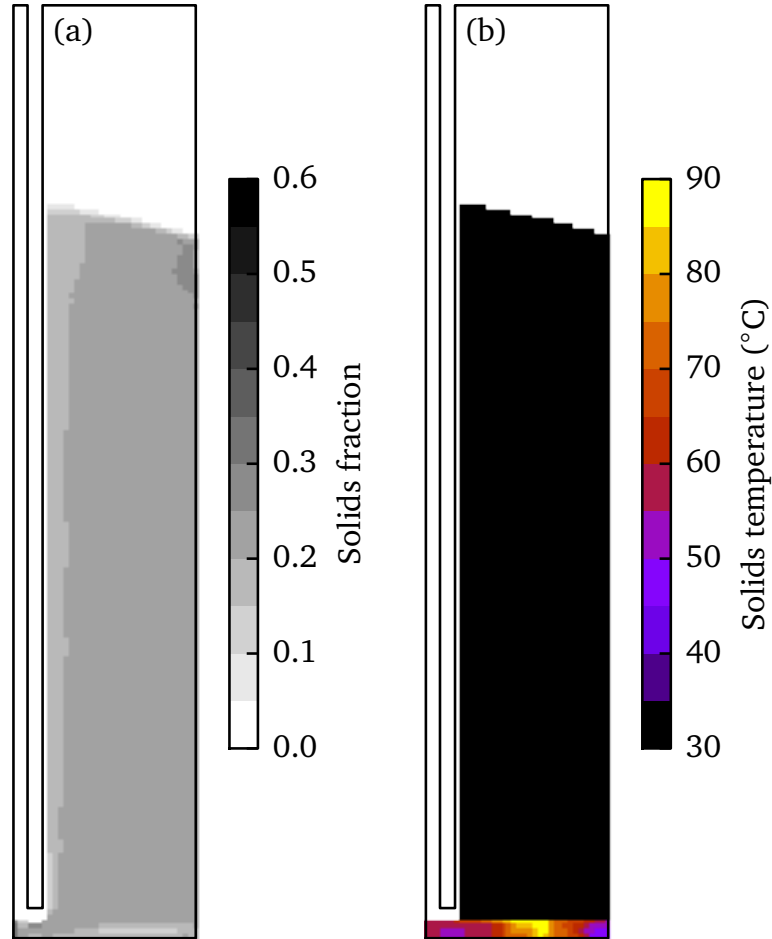


Figure 5.2: Snapshot of a) solids fraction and b) solids temperature fields in a 1 MW solid-sorbent carbon capture (using an ad-hoc heat transfer model [107]) after 500 seconds.

discovered that the simulation was sensitive to the initial loading of polyethyleneimine. When the initial loading was lowered from 20%, more realistic capture rates were observed, e.g., 10% loading resulted in a capture rate of 90%. This work is ongoing in collaboration with the process modelers to quantify the error in both models.

The ad-hoc heat transfer model took $1.3 \text{ hours} \times 16 \text{ processors} = 21 \text{ CPU hours}$ to simulate, while the subgrid model took $6.7 \text{ hours} \times 16 \text{ processors} = 107 \text{ CPU hours}$. Though the subgrid model is approximately five times slower than the ad-hoc model, the overall time scale (21 vs 108 CPU hours) is sufficiently small that the differ-

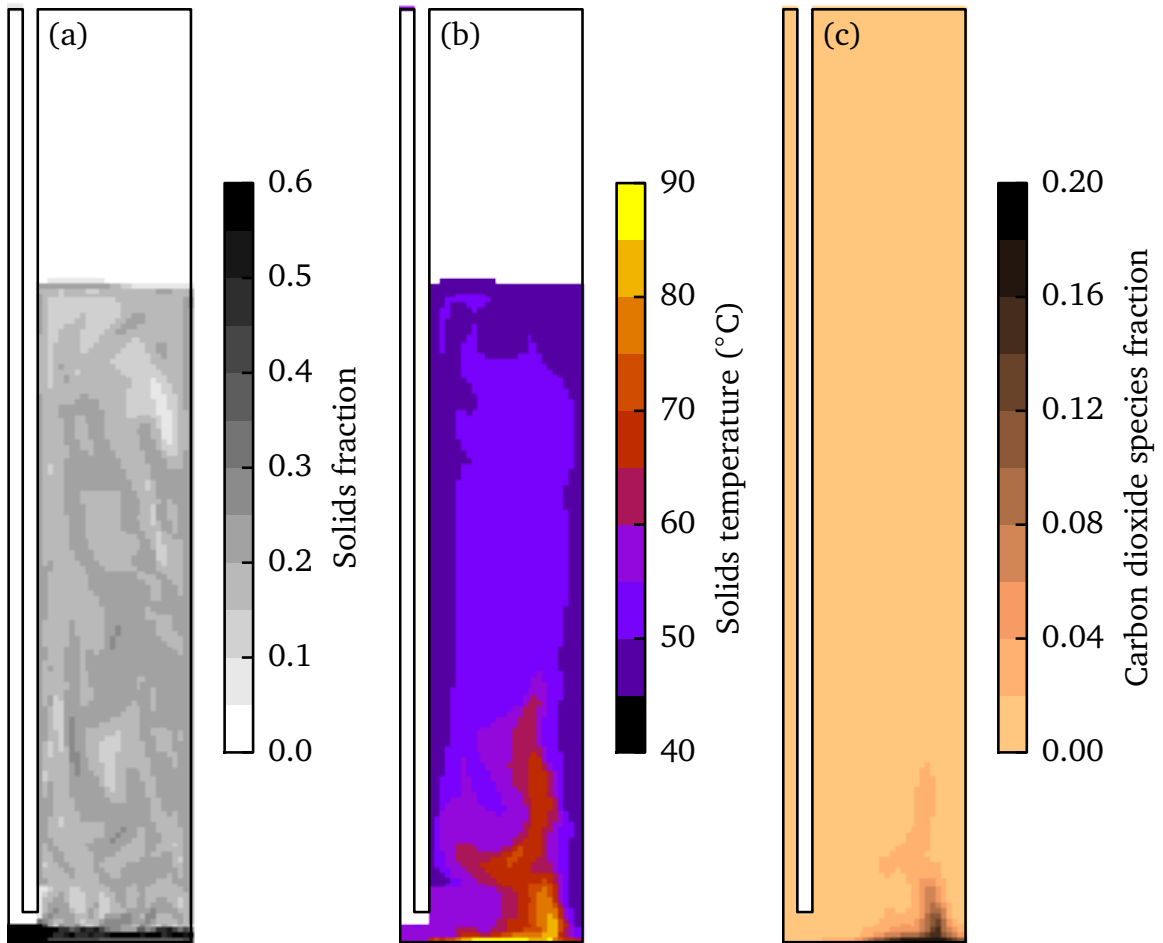


Figure 5.3: Snapshot of a) solids fraction, b) solids temperature, and c) carbon dioxide species fraction fields in a 1 MW solid-sorbent carbon capture (using the subgrid heat transfer model) after 500 seconds.

ences are negligible, especially when considering the advantages of physically realistic results.

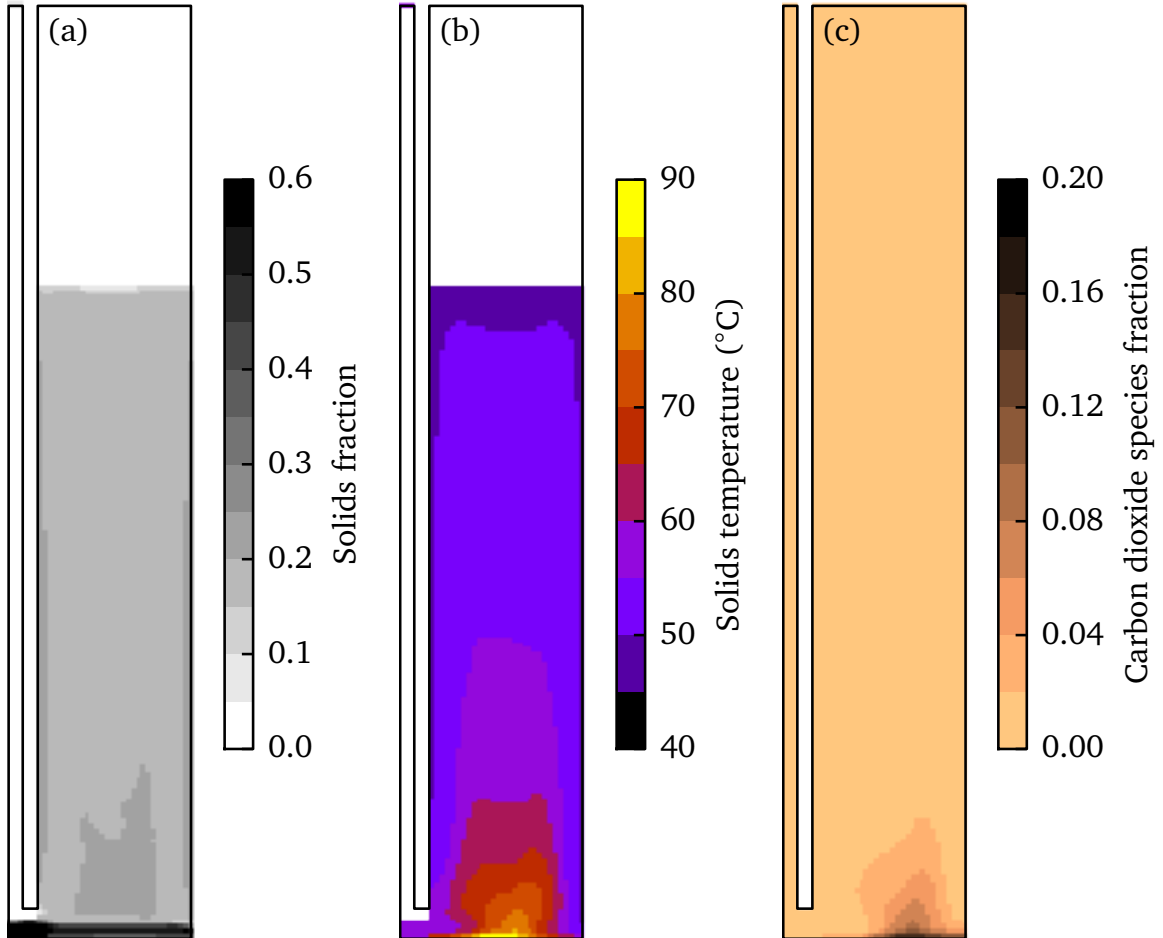


Figure 5-4: Average a) solids fraction, b) solids temperature, c) and carbon dioxide species fraction fields in a 1 MW solid-sorbent carbon capture (using the subgrid heat transfer model). Data was averaged from 200–500 seconds.

Chapter 6

Conclusions

6.1 VVUQ Framework for CFD

A framework for the verification, validation, and uncertainty quantification for expensive, multiscale, computer models was developed. The statistical methods were applied to a specific case of a fluidized bed as an example; however, the method was presented such that it can be applied to any system. The framework consists of 7 steps: 1) identify model parameters of interest, 2) determine prior distributions, 3) design numerical experiments, 4) complete numerical experiments and tabulate data, 5) perform sensitivity analysis, 6) using the calibration procedure, explore the parameter state-space with MCMC by evaluating the emulator tens of thousands of times to generate posterior distributions, and 7) cross validate the model by providing out-of-sample predictions with confidence bands.

Using this statistical framework, the hydrodynamics of a bubbling fluidized bed with immersed horizontal tubes was studied to quantify the uncertainty associated with CFD model input parameters. From this conclusions could be drawn about the optimal parameter values for operation. This framework was intended to also consider heat transfer in the same system; however, due to numerical limitations, it was not possible. The results from these studies were used to model the DOE National Energy Technology Laboratory's experimental bench-scale carbon capture system, the C2U [8, 108].

6.2 Subgrid Models

Using traditional filtering methods, a subgrid model for predicting heat transfer in gas-particle flows with immersed horizontal heat transfer cylinders was developed. The model is analogous to existing single-phase heat transfer correlations but includes the effects of the solids phase (i.e., density, particle diameter, thermal conductivity, specific heat capacity, solids fraction, and velocity). The model went through verification, validation, and uncertainty quantification. It showed excellent agreement with the verification and validation tests. The uncertainty quantification determined the accuracy of the model predictions were similar to standard single-phase Nusselt correlations. Computational-time savings were observed anywhere from 60 to 100,000 times faster, depending on the size of the system and grid, and the included physics.

Similar to the VVUQ framework, the model development framework was presented such that it could be adapted to suit different multiphase and/or multiphysics problems.

6.3 Future Work

The subgrid model developed in this research considered only flow across horizontal cylinders; however, multiphase flow can be quite abrasive and cause pitting and degradation on the cylinders in a horizontal configuration. This is usually avoided by using vertical cylinders. While the flow behavior changes (there is more channeling and less bifurcation), good mixing and high heat- and mass-transfer rates can still be achieved.

Extending this model to consider vertical cylinders configurations would be very valuable. However, simulating such a system requires small, periodic, 3D domains (due to the nature of simulating vertical cylinders). These simulations can be computationally intensive, and as a result were not completed and included in this work.

Additionally, this framework could be readily applied to mass transfer. Similar to drag and heat transfer, using coarse grids likely under-predicts the rate of mass transfer. By using a subgrid filtering approach it should be possible to constitute a mass transfer correlation to predict the unresolved physics.

Appendix A

Simulation Data

The input data used to generate the results for the non-linear regression to form the subgrid model are listed in Table A.1.

Table A.1: Data used to generate the subgrid model.

$\bar{\phi}_s$	D_c/a_c	$ \tilde{\mathbf{v}}_s /v_t$	$\overline{\text{Pe}}_{cs}$	$\overline{\text{Nu}}_{cs}$	$\bar{\phi}_s$	D_c/a_c	$ \tilde{\mathbf{v}}_s /v_t$	$\overline{\text{Pe}}_{cs}$	$\overline{\text{Nu}}_{cs}$
0.05	0.10	3.68	531	3.71	0.30	0.10	0.83	531	2.85
0.05	0.15	3.83	531	3.81	0.30	0.15	0.75	531	2.98
0.05	0.20	3.60	531	3.97	0.30	0.20	0.68	531	2.97
0.05	0.25	3.75	531	4.62	0.30	0.25	0.68	531	3.00
0.05	0.30	3.91	531	5.28	0.30	0.30	0.68	531	3.40
0.05	0.35	3.68	531	5.84	0.30	0.35	0.83	531	3.45
0.05	0.40	3.83	531	6.44	0.30	0.40	0.75	531	3.69
0.30	0.10	3.98	531	4.74	0.60	0.25	3.91	531	4.79
0.30	0.15	3.60	531	4.72	0.55	0.25	3.83	531	5.76
0.30	0.20	3.75	531	5.14	0.45	0.25	3.75	531	5.93
0.30	0.25	3.91	531	5.65	0.30	0.25	3.91	531	5.66
0.30	0.30	3.91	531	6.50	0.15	0.25	3.91	531	5.10
0.30	0.35	3.68	531	6.63	0.05	0.25	3.68	531	3.99
0.30	0.40	3.83	531	7.29	0.01	0.25	3.75	531	2.60
0.30	0.10	3.91	1170	6.32	0.60	0.40	3.60	531	7.07
0.30	0.15	3.68	1170	6.35	0.55	0.40	6.76	531	7.20
0.30	0.20	3.68	1170	6.68	0.45	0.40	3.83	531	7.30

$\bar{\phi}_s$	D_c/a_c	$ \tilde{\mathbf{v}}_s /v_t$	$\bar{\text{Pe}}_{cs}$	$\bar{\text{Nu}}_{cs}$	$\bar{\phi}_s$	D_c/a_c	$ \tilde{\mathbf{v}}_s /v_t$	$\bar{\text{Pe}}_{cs}$	$\bar{\text{Nu}}_{cs}$
0.30	0.25	3.91	1170	7.58	0.30	0.40	3.83	531	7.29
0.30	0.30	3.91	1170	8.17	0.15	0.40	3.75	531	7.19
0.30	0.35	3.68	1170	8.45	0.05	0.40	3.83	531	6.48
0.30	0.40	3.75	1170	9.28	0.01	0.40	3.98	531	2.45
0.60	0.25	4.13	1170	6.65	0.30	0.25	1.65	1170	5.81
0.55	0.25	3.83	1170	7.61	0.30	0.25	2.55	1170	6.39
0.45	0.25	3.83	1170	7.67	0.30	0.25	3.91	531	5.65
0.30	0.25	3.91	1170	7.53	0.30	0.25	4.96	531	6.38
0.15	0.25	3.68	1170	7.00	0.30	0.25	6.08	531	6.91
0.05	0.25	3.68	1170	5.95	0.30	0.25	6.68	531	7.04
0.01	0.25	3.75	1170	4.31	0.30	0.25	0.68	531	3.00
0.60	0.25	0.83	531	3.62	0.30	0.25	1.58	531	3.88
0.55	0.25	0.83	531	3.64	0.30	0.25	2.55	531	4.80
0.45	0.25	0.75	531	3.43	0.05	0.25	3.83	372	3.88
0.30	0.25	0.68	531	3.00	0.05	0.25	3.68	531	4.00
0.15	0.25	0.83	531	2.71	0.05	0.25	3.83	690	4.78
0.05	0.25	0.68	531	1.79	0.05	0.25	3.83	849	5.36
0.01	0.25	0.68	531	0.74	0.05	0.25	3.83	1010	5.49
0.05	0.25	3.83	531	5.01	0.05	0.25	3.75	1170	5.77
0.05	0.25	4.81	531	5.42	0.05	0.25	3.68	1330	5.96
0.05	0.25	6.16	531	5.72	0.30	0.40	3.83	372	6.37
0.05	0.25	6.98	531	5.90	0.30	0.40	3.83	531	7.29
0.05	0.25	0.90	531	1.88	0.30	0.40	3.83	690	7.94
0.05	0.25	1.43	531	2.64	0.30	0.40	3.83	849	8.47
0.05	0.25	2.70	531	3.80	0.30	0.40	3.83	1010	8.88
0.30	0.40	0.75	531	3.69	0.30	0.40	3.83	1170	9.28
0.30	0.40	1.43	531	5.13	0.30	0.40	3.83	1330	9.66

$\bar{\phi}_s$	D_c/a_c	$ \tilde{\mathbf{v}}_s /v_t$	$\overline{\text{Pe}}_{cs}$	$\overline{\text{Nu}}_{cs}$	$\bar{\phi}_s$	D_c/a_c	$ \tilde{\mathbf{v}}_s /v_t$	$\overline{\text{Pe}}_{cs}$	$\overline{\text{Nu}}_{cs}$
0.30	0.40	2.63	531	6.61	0.30	0.25	3.91	372	5.16
0.30	0.40	3.83	531	7.29	0.30	0.25	3.91	531	5.65
0.30	0.40	4.88	531	7.84	0.30	0.25	3.91	690	6.48
0.30	0.40	6.16	531	8.23	0.30	0.25	3.83	849	6.90
0.30	0.40	6.83	531	8.34	0.30	0.25	3.91	1010	7.32
0.30	0.25	3.91	1170	7.53	0.30	0.25	3.91	1170	7.53
0.30	0.25	4.96	1170	8.05	0.30	0.25	3.91	1330	7.81
0.30	0.25	6.16	1170	8.55	0.30	0.25	0.60	372	2.46
0.30	0.25	6.61	1170	8.59	0.30	0.25	0.60	531	2.92
0.30	0.25	0.60	1170	4.12	0.30	0.25	0.60	690	3.31
0.30	0.25	0.60	849	3.65	0.30	0.25	0.60	1010	3.96
0.30	0.25	0.60	1170	4.24	0.30	0.25	0.60	1330	4.48

Appendix B

Source Code

The FORTRAN source code for the MFIX implementation of the subgrid model for cylinder-gas heat transfer [92] is included below:

```

IF (FLUID_AT(IJK)) THEN
  APO = ROP_GO(IJK)*C_PG(IJK)*VOL(IJK)*ODT
  S_P(IJK) = APO + S_RPG(IJK)*VOL(IJK)
  S_C(IJK) = APO*T_GO(IJK)-HOR_G(IJK)*VOL(IJK)+S_RCG(IJK)*VOL(IJK)
! Lane sub-grid models - 07/2015
  IF (SG_CYL_ENERGY) THEN
    IF (EP_S(IJK,1) <= DIL_EP_S .AND. EP_S(IJK,2) > ZERO) THEN
      ! Variables for Nusselt number calculation
      EP_G_STAR = EP_G(IJK)/(1.0-EP_S(IJK,2))
      V_G_MAG = SQRT(U_G(IJK)**2 + V_G(IJK)**2 + W_G(IJK)**2)
      RE_CG = RO_g(IJK)*V_G_MAG*SG_CYL_D/MU_G(IJK)
      PR_CG = C_PG(IJK)*MU_G(IJK)/K_G(IJK)
      ! Nusselt number and heat transfer coefficient
      NU_CG = (0.289 + 2.53*(SG_CYL_D/SG_CYL_A)**1.65) &
        * RE_CG**0.564 * PR_CG**0.430
      H_CG = NU_CG*K_G(IJK)/SG_CYL_D
      ! Area calculation and correction
      L_R = DX(I)*DY(J)/SG_CYL_A**2 ! Length-scaling ratio
      A_C = 2.0*PI*(L_R*SG_CYL_D) ! 2D/3D Correction factor
      ! Source term
      Q_CG = EP_G_STAR*H_CG*A_C*(SG_CYL_T-T_G(IJK))
      S_C(IJK) = S_C(IJK) + Q_CG
    ENDIF
  ENDIF
  IF(USE_MMS) S_C(IJK) = S_C(IJK) + MMS_T_G_SRC(IJK)*VOL(IJK)
ELSE
  S_P(IJK) = ZERO
  S_C(IJK) = ZERO
ENDIF

```

The FORTRAN source code for the MFIX implementation of the subgrid model for cylinder-suspension heat transfer is included below:

```

IF (FLUID_AT(IJK)) THEN
  APO = ROP_SO(IJK,M)*C_PS(IJK,M)*VOL(IJK)*ODT
  S_P(IJK) = APO + S_RPS(IJK,M)*VOL(IJK)
  S_C(IJK) = APO*T_SO(IJK,M) - HOR_S(IJK,M)*VOL(IJK) &
    + S_RCS(IJK,M)*VOL(IJK)
  IF (SG_CYL_ENERGY) THEN
    IF (EP_S(IJK,1) > DIL_EP_S .AND. EP_S(IJK,2) > ZERO) THEN
      ! Variables for Nusselt number calculation
      EP_G_STAR = EP_G(IJK)/(1.0-EP_S(IJK,2))
      EP_S_STAR = EP_S(IJK,1)/(1.0-EP_S(IJK,2))
      V_T = D_P(IJK,1)**2*GRAVITY*(RO_S(IJK,1)-RO_G(IJK)) &
        /(18.0*MU_G(IJK))
      L_STAR = V_T**2/GRAVITY
      V_S_STAR = SQRT(U_S(IJK,1)**2 + V_S(IJK,1)**2 &
        + W_S(IJK,1)**2)/V_T
      PE_CS = RO_S(IJK,1)*C_PS(IJK,1)*V_T*L_STAR/K_S(IJK,1)
      ! Nusselt number and heat transfer coefficient
      NU_CS = 0.354 * EP_S_STAR**0.125 * V_S_STAR**0.341
        * (1.0 + 2.94*(SG_CYL_D/SG_CYL_A)**1.76) * PE_CS**0.353
      H_CS = NU_CS*K_S(IJK,1)/L_STAR
      ! Area calculation and correction
      L_R = (DX(I)*DY(J))/SG_CYL_A**2
      A_C = 2.0*PI*(L_R*SG_CYL_D) ! 2D/3D Correction factor
      ! Source term
      T_SUSP = EP_G_STAR*T_G(IJK) + EP_S_STAR*T_S(IJK,1)
      Q_CS = H_CS*A_C*(SG_CYL_T - T_SUSP)
      S_C(IJK) = S_C(IJK) + Q_CS
    ENDIF
  ENDIF
  VXGAMA(IJK,M) = GAMA_GS(IJK,M)*VOL(IJK)
  EPS(IJK) = EP_S(IJK,M)
  IF(USE_MMS) S_C(IJK) = S_C(IJK) + MMS_T_S_SRC(IJK)*VOL(IJK)
ELSE
  S_P(IJK) = ZERO
  S_C(IJK) = ZERO
  VXGAMA(IJK,M) = ZERO
  EPS(IJK) = ZERO
  IF(USE_MMS) EPS(IJK) = EP_S(IJK,M)
ENDIF

```


Bibliography

- [1] Robert Herman and Ilya Prigogine. A two-fluid approach to town traffic. *Science*, 204(4389):148–151, April 13 1979.
- [2] S. Benyahia, M. Syamlal, and T. J. Obrien. Summary of MFIX Equations, from https://mfix.net1.doe.gov/download/mfix/mfix_current_documentation/MFIXEquations2012-1.pdf, January 2012.
- [3] H. G. Weller. A tensorial approach to computational continuum mechanics using object-oriented techniques. *Computers in Physics*, 12(6):620, November 1998.
- [4] L. X. Zhou, Y. Zhang, and J. Zhang. Simulation of swirling coal combustion using a full two-fluid model and an AUSM turbulence-chemistry model. *Fuel*, 82(8):1001–1007, May 2003.
- [5] S M A Noori Rahim Abadi, R. Kouhikamali, and K. Atashkari. Two-fluid model for simulation of supersonic flow of wet steam within high-pressure nozzles. *International Journal of Thermal Sciences*, 96:173–182, October 2015.
- [6] Deoras Prabhudharwadkar, Martin A. Lopez de Bertodano, Takashi Hibiki, and John R. Buchanan Jr. Assessment of subcooled boiling wall boundary correlations for two-fluid model CFD. *International Journal of Heat and Mass Transfer*, 79:602–617, December 2014.
- [7] Pandaba Patro and Sukanta K. Dash. Two-fluid modeling of turbulent particle-gas suspensions in vertical pipes. *Powder Technology*, 264:320–331, September 2014.
- [8] Guangli He, Pingwen Ming, Zongchang Zhao, Abuliti Abudula, and Yu Xiao. A two-fluid model for two-phase flow in PEMFCs. *Journal of Power Sources*, 163(2):864–873, January 1 2007.
- [9] A. Munjiza, D. R. J. Owen, and N. Bicanic. A combined finite-discrete element method in transient dynamics of fracturing solids. *Engineering Computations*, 12(2):145–174, 1995.
- [10] Maitraye Sen, Dana Barrasso, Ravendra Singh, and Rohit Ramachandran. A multi-scale hybrid CFD-DEM-PBM description of a fluid-bed granulation process. *Processes*, 2(1):89–111, January 21 2014.

- [11] Handan Liu, Danesh K. Tafti, and Tingwen Li. Hybrid parallelism in MFIX CFD-DEM using OpenMP. *Powder Technology*, 259:22–29, June 2014.
- [12] Liancheng Guo, Koji Morita, Hirotaka Tagami, and Yoshiharu Tobita. Validation of a 3D hybrid CFD-DEM method based on a self-leveling experiment. In *Proceedings of the 22nd International Conference on Nuclear Engineering - 2014*. Paper No. ICONE22-30618. New York: American Society of Mechanical Engineers, 2014. doi:10.1115/ICONE22-30618, July 7, 2014.
- [13] Heng Xiao and Jin Sun. Algorithms in a robust hybrid CFD-DEM solver for particle-laden flows. *Communications in Computational Physics*, 9(02):297323, February 2011.
- [14] A. Sarkar, X. Sun, and S. Sundaresan. Sub-grid drag models for horizontal cylinder arrays immersed in gas-particle multiphase flows. *Chemical Engineering Science*, 104:399–412, December 18 2013.
- [15] A. Sarkar, X. Sun, and S. Sundaresan. Verification of sub-grid filtered drag models for gas-particle fluidized beds with immersed cylinder arrays. *Chemical Engineering Science*, 114:144–154, July 26 2014.
- [16] Y. Igci, A. T. Andrews, S. Sundaresan, S. Pannala, and T. O’Brien. Filtered two-fluid models for fluidized gas-particle suspensions. *AIChE Journal*, 54(6):1431–1448, 2008.
- [17] Yesim Igci and Sankaran Sundaresan. Verification of filtered two-fluid models for gas-particle flows in risers. *AIChE Journal*, 57(10):2691–2707, October 1 2011.
- [18] Yesim Igci and Sankaran Sundaresan. Constitutive models for filtered two-fluid models of fluidized gasparticle flows. *Industrial & Engineering Chemistry Research*, 50(23):13190–13201, December 7 2011.
- [19] J. Smagorinsky. General circulation experiments with the primitive equations. *Monthly Weather Review*, 91(3):99, 1963.
- [20] A. T. Andrews, P. N. Loezos, and S. Sundaresan. Coarse-grid simulation of gas-particle flows in vertical risers. *Industrial & Engineering Chemistry Research*, 44(16):6022–6037, April 5 2005.
- [21] J. F. Parmentier, O. Simonin, and O. Delsart. A functional subgrid drift velocity model for filtered drag prediction in dense fluidized bed. *AIChE Journal*, 58(4):1084–1098, 2012.
- [22] Pekka I. Viitanen. Tracer studies on a riser reactor of a fluidized catalyst cracking plant. *Industrial & Engineering Chemistry Research*, 32(4):577–583, April 1 1993.

- [23] C. Wu, Y. Cheng, and Y. Jin. Downer-to-riser coupling technique for petroleum refining. *Chemical Engineering & Technology*, 32(3):482–491, March 1 2009.
- [24] K. Agrawal, W. Holloway, C. C. Milioli, F. E. Milioli, and S. Sundaresan. Filtered models for scalar transport in gasparticle flows. *Chemical Engineering Science*, 95:291–300, May 24 2013.
- [25] Thomas M. Cioppa and Thomas W. Lucas. Efficient nearly orthogonal and space-filling latin hypercubes. *Technometrics*, 49(1):45–55, February 1 2007.
- [26] State-of-the-art review: A users guide to the brave new world of designing simulation experiments. *INFORMS Journal on Computing*, 17(3):263–289, August 1 2005.
- [27] Andrea Saltelli, K. Chan, and E. M. Scott. *Sensitivity analysis*. Wiley, New York, 2009.
- [28] J. C. Helton. Uncertainty and sensitivity analysis in the presence of stochastic and subjective uncertainty. *Journal of Statistical Computation and Simulation*, 57(1-4):3–76, April 1 1997.
- [29] Jeremy Oakley and Anthony O’Hagan. Bayesian inference for the uncertainty distribution of computer model outputs. *Biometrika*, 89(4):769–784, 2002.
- [30] D. Higdon, M. Kennedy, J. Cavendish, J. Cafeo, and R. Ryne. Combining field data and computer simulations for calibration and prediction. *SIAM Journal on Scientific Computing*, 26(2):448–466, January 1 2004.
- [31] Dave Higdon, Herbie Lee, and Chris Holloman. Markov chain Monte Carlo-based approaches for inference in computationally intensive inverse problems. page 181. in J.M. Bernardo et al. (eds.) *Bayesian Statistics 7: Proceedings of the Seventh Valencia International Meeting*. New York: Oxford University Press, 2003.
- [32] Tingwen Li, Jean-Francois Dietiker, Yongmin Zhang, and Mehrdad Shahnám. Cartesian grid simulations of bubbling fluidized beds with a horizontal tube bundle. *Chemical Engineering Science*, 66(23):6220–6231, December 1 2011.
- [33] Fernanda Ribeiro Gaspar Branco da Silva, Marcos de Souza, Alexandre Marconi de Souza da Costa, Luiz Mario de Matos Jorge, and Paulo Roberto Paraso. Experimental and numerical analysis of soybean meal drying in fluidized bed. *Powder Technology*, 229:61–70, October 2012.
- [34] Tim McKeen and Todd Pugsley. Simulation and experimental validation of a freely bubbling bed of FCC catalyst. *Powder Technology*, 129(13):139–152, January 8 2003.

- [35] Jonghwun Jung and Isaac K. Gamwo. Multiphase CFD-based models for chemical looping combustion process: Fuel reactor modeling. *Powder Technology*, 183(3):401–409, April 21 2008.
- [36] Tingwen Li, John Grace, and Xiaotao Bi. Study of wall boundary condition in numerical simulations of bubbling fluidized beds. *Powder Technology*, 203(3):447–457, November 25 2010.
- [37] Fei Li, Feifei Song, Sofiane Benyahia, Wei Wang, and Jinghai Li. MP-PIC simulation of CFB riser with EMMS-based drag model. *Chemical Engineering Science*, 82:104–113, September 12 2012.
- [38] N. Reuge, L. Cadoret, and B. Caussat. Multifluid eulerian modelling of a silicon fluidized bed chemical vapor deposition process: Analysis of various kinetic models. *Chemical Engineering Journal*, 148(23):506–516, May 15 2009.
- [39] E. M. Ryan, D. DeCroix, R. Breault, W. Xu, E. D. Huckaby, K. Saha, S. Darteville, and X. Sun. Multi-phase CFD modeling of solid sorbent carbon capture system. *Powder Technology*, 242:117–134, July 2013.
- [40] M. Syamlal and W. Rogers. MFIx theory guide, (DOE/METC-94/1004, DE94000087). Technical report, Department of Energy, Office of Fossil Energy, 1993.
- [41] M. Syamlal. A review of granular stress constitutive relations, (DOE/MC/21353-2372, DE87006499). Technical report, National Technical Information Services, 1987.
- [42] C. Wen and Y. Yu. Mechanics of fluidization. *Chemical Engineering Progress Symposium Series*, 62:100–111, 1966.
- [43] Ehsan Esmaili and Nader Mahinpey. Adjustment of drag coefficient correlations in three dimensional CFD simulation of gas-solid bubbling fluidized bed. *Advances in Engineering Software*, 42(6):375–386, June 2011.
- [44] M. Syamlal and T. J. O’Brien. The derivation of a drag coefficient formula from velocity-voidage correlations. Technical report, U.S. Department of Energy, Office of Fossil Energy, 1987.
- [45] Reghan J. Hill, Donald L. Koch, and Anthony J. C. Ladd. The first effects of fluid inertia on flows in ordered and random arrays of spheres. *Journal of Fluid Mechanics*, 448:213–241, December 2001.
- [46] Reghan J. Hill, Donald L. Koch, and Anthony J. C. Ladd. Moderate-reynolds-number flows in ordered and random arrays of spheres. *Journal of Fluid Mechanics*, 448:243–278, December 2001.

- [47] R. Beetstra, M A van der Hoef, and J. A. M. Kuipers. Numerical study of segregation using a new drag force correlation for polydisperse systems derived from lattice-boltzmann simulations. *Chemical Engineering Science*, 62(12):246–255, January 2007.
- [48] William Holloway, Xiaolong Yin, and Sankaran Sundaresan. Fluid-particle drag in inertial polydisperse gassolid suspensions. *AIChE Journal*, 56(8):1995–2004, August 1 2010.
- [49] Sabri Ergun and A. A. Orning. Fluid flow through randomly packed columns and fluidized beds. *Industrial & Engineering Chemistry*, 41(6):1179–1184, 1949.
- [50] D. J. Gunn. Transfer of heat or mass to particles in fixed and fluidised beds. *International Journal of Heat and Mass Transfer*, 21(4):467–476, April 1978.
- [51] N. I. Gelperin and V. G. Einstein. *Heat Transfer in Fluidized Beds*. Academic Press, New York, 1971.
- [52] Sergej S. Zabrodskiy. *Hydrodynamics and heat transfer in fluidized beds*. M.I.T. Press, Cambridge, MA, 1966.
- [53] D. C. Miller, M. Syamlal, D. S. Mebane, C. Storlie, D. Bhattacharyya, N. V. Sahinidis, D. Agarwal, C. Tong, S. E. Zitney, A. Sarkar, X. Sun, S. Sundaresan, E. M. Ryan, D. Engel, and C. Dale. Carbon capture simulation initiative: A case study in multiscale modeling and new challenges. *Annual Review of Chemical and Biomolecular Engineering*, 5(1):301–323, June 2014.
- [54] S. E. Olsson, J. Wiman, and A. E. Almstedt. Hydrodynamics of a pressurized fluidized bed with horizontal tubes: Influence of pressure, fluidization velocity and tube-bank geometry. *Chemical Engineering Science*, 50(4):581–592, February 1995.
- [55] Teklay Weldeabzgi Asegehegn, Matthias Schreiber, and Hans Joachim Krautz. Investigation of bubble behavior in fluidized beds with and without immersed horizontal tubes using a digital image analysis technique. *Powder Technology*, 210(3):248–260, July 10 2011.
- [56] Ashley S. Hull, Zumao Chen, Jack W. Fritz, and Pradeep K. Agarwal. Influence of horizontal tube banks on the behavior of bubbling fluidized beds: 1. bubble hydrodynamics. *Powder Technology*, 103(3):230–242, July 26 1999.
- [57] Ashley S. Hull, Zumao Chen, and Pradeep K. Agarwal. Influence of horizontal tube banks on the behavior of bubbling fluidized beds: 2. mixing of solids. *Powder Technology*, 111(3):192–199, September 11 2000.

- [58] Sung Won Kim, Jung Yeul Ahn, Sang Done Kim, and Dong Hyun Lee. Heat transfer and bubble characteristics in a fluidized bed with immersed horizontal tube bundle. *International Journal of Heat and Mass Transfer*, 46(3):399–409, January 2003.
- [59] T. Li, J. Grace, and X. Bi. Study of wall boundary condition in numerical simulations of bubbling fluidized beds. *Powder Technology*, 203(3):447–457, 2010.
- [60] Zhongxi Chao, Yuefa Wang, Jana P. Jakobsen, Maria Fernandino, and Hugo A. Jakobsen. Derivation and validation of a binary multi-fluid eulerian model for fluidized beds. *Chemical Engineering Science*, 66(16):3605–3616, August 15 2011.
- [61] Nicoleta Herzog, Matthias Schreiber, Christoph Egbers, and Hans Joachim Krautz. A comparative study of different CFD-codes for numerical simulation of gassolid fluidized bed hydrodynamics. *Computers & Chemical Engineering*, 39:41–46, April 6 2012.
- [62] Teklay Weldeabzgi Asegehegn, Matthias Schreiber, and Hans Joachim Krautz. Numerical simulation and experimental validation of bubble behavior in 2d gassolid fluidized beds with immersed horizontal tubes. *Chemical Engineering Science*, 66(21):5410–5427, November 1 2011.
- [63] Ian Hulme, Eric Clavelle, Loni van der Lee, and Apostolos Kantzas. CFD modeling and validation of bubble properties for a bubbling fluidized bed. *Industrial & Engineering Chemistry Research*, 44(12):4254–4266, June 1 2005.
- [64] Hvard Lindborg, Magne Lysberg, and Hugo A. Jakobsen. Practical validation of the two-fluid model applied to dense gassolid flows in fluidized beds. *Chemical Engineering Science*, 62(21):5854–5869, November 2007.
- [65] Yuemin Zhao, Ligang Tang, Zhenfu Luo, Chuncheng Liang, Hongbo Xing, Wanchang Wu, and Chenlong Duan. Experimental and numerical simulation studies of the fluidization characteristics of a separating gassolid fluidized bed. *Fuel Processing Technology*, 91(12):1819–1825, December 2010.
- [66] Teklay Weldeabzgi Asegehegn, Matthias Schreiber, and Hans Joachim Krautz. Influence of two- and three-dimensional simulations on bubble behavior in gas-solid fluidized beds with and without immersed horizontal tubes. *Powder Technology*, 219:9–19, March 2012.
- [67] Sun Dan, Wang Jianzhi, Lu Huilin, Zhao Yunhua, Chen Juhui, Dimitri Gidaspow, and Chen Ming. Numerical simulation of gas-particle flow with a second-order moment method in bubbling fluidized beds. *Powder Technology*, 199(3):213–225, May 15 2010.

- [68] Degang Rong, Takafumi Mikami, and Masayuki Horio. Particle and bubble movements around tubes immersed in fluidized beds a numerical study. *Chemical Engineering Science*, 54(23):5737–5754, December 1999.
- [69] Rahel Yusuf, Britt Halvorsen, and Morten C. Melaaen. An experimental and computational study of wall to bed heat transfer in a bubbling gassolid fluidized bed. *International Journal of Multiphase Flow*, 42:9–23, June 2012.
- [70] J. C. Helton and F. J. Davis. Latin hypercube sampling and the propagation of uncertainty in analyses of complex systems. *Reliability Engineering & System Safety*, 81(1):23–69, July 2003.
- [71] Marc C. Kennedy and Anthony O’Hagan. Bayesian calibration of computer models. *Journal of the Royal Statistical Society: Series B (Statistical Methodology)*, 63(3):425–464, January 1 2001.
- [72] Curtis B. Storlie, William A. Lane, Emily M. Ryan, James R. Gattiker, and David M. Higdon. Calibration of computational models with categorical parameters and correlated outputs via bayesian smoothing spline ANOVA. *Journal of the American Statistical Association*, 110(509):68–82, January 2 2015.
- [73] Brian J. Reich, Curtis B. Storlie, and Howard D. Bondell. Variable selection in bayesian smoothing spline ANOVA models: Application to deterministic computer codes. *Technometrics*, 51(2):110–120, May 1 2009.
- [74] Geof H. Givens and Jennifer A. Hoeting. *Computational statistics*. Wiley, Hoboken, N.J, 2. ed. edition, 2013.
- [75] Curtis B. Storlie, Laura P. Swiler, Jon C. Helton, and Cedric J. Sallaberry. Implementation and evaluation of nonparametric regression procedures for sensitivity analysis of computationally demanding models. *Reliability Engineering & System Safety*, 94(11):1735–1763, November 2009.
- [76] Curtis B. Storlie and Jon C. Helton. Multiple predictor smoothing methods for sensitivity analysis: Example results. *Reliability Engineering & System Safety*, 93(1):55–77, January 2008.
- [77] Curtis B. Storlie and Jon C. Helton. Multiple predictor smoothing methods for sensitivity analysis: Description of techniques. *Reliability Engineering & System Safety*, 93(1):28–54, January 2008.
- [78] K. Everaert, J. Baeyens, and K. Smolders. Heat transfer from a single tube to the flowing gas-solid suspension in a CFB riser. *Heat Transfer Engineering*, 27(6):66–70, June 1 2006.

- [79] Nanak S. Grewal and Satish C. Saxena. Maximum heat transfer coefficient between a horizontal tube and a gas-solid fluidized bed. *Industrial & Engineering Chemistry Process Design and Development*, 20(1):108–116, January 1 1981.
- [80] Nima Masoumifard, Navid Mostoufi, Ali-Asghar Hamidi, and Rahmat Sotudeh-Gharebagh. Investigation of heat transfer between a horizontal tube and gas-solid fluidized bed. *International Journal of Heat and Fluid Flow*, 29(5):1504–1511, October 2008.
- [81] N. S. Grewal and S. C. Saxena. Heat transfer between a horizontal tube and a gas-solid fluidized bed. *International Journal of Heat and Mass Transfer*, 23(11):1505–1519, November 1980.
- [82] Rahel Yusuf, Britt Halvorsen, and Morten Christian Melaaen. Eulerianeulerian simulation of heat transfer between a gassolid fluidized bed and an immersed tube-bank with horizontal tubes. *Chemical Engineering Science*, 66(8):1550–1564, April 15 2011.
- [83] D. J. Patil, J. Smit, M. van Sint Annaland, and J. a. M. Kuipers. Wall-to-bed heat transfer in gassolid bubbling fluidized beds. *AIChE Journal*, 52(1):58–74, January 1 2006.
- [84] Sung Won Kim and Sang Done Kim. Heat transfer characteristics in a pressurized fluidized bed of fine particles with immersed horizontal tube bundle. *International Journal of Heat and Mass Transfer*, 64:269–277, September 2013.
- [85] J. F Dietiker. Multiphase Flow with Interface eXchanges Cartesian Grid User Guide, from https://mfix.net1.doe.gov/download/mfix/mfix_current_documentation/Cartesian_grid_user_guide.pdf, 2015.
- [86] W. Holloway and S. Sundaresan. Filtered models for reacting gasparticle flows. *Chemical Engineering Science*, 82:132–143, September 12 2012.
- [87] K. Agrawal, P. N. Loezos, M. Syamlal, and S. Sundaresan. The role of meso-scale structures in rapid gassolid flows. *Journal of Fluid Mechanics*, 445:151–185, October 2001.
- [88] H. H. Ku. Notes on the use of propagation of error formulas. *Journal of Research of the National Bureau of Standards, Section C: Engineering and Instrumentation*, 70C(4):263–273, October 1966.
- [89] E. Buckingham. On physically similar systems; illustrations of the use of dimensional equations. *Physical Review*, 4(4):345–376, October 1914.
- [90] E. Jones, T. Oliphant, P. Peterson, and et al. SciPy: Open source scientific tools for Python, 2001.

- [91] F. P. Incropera and D. P. Dewitt. *Fundamentals of Heat and Mass Transfer*. Wiley, 5th edition, 2002.
- [92] W. A. Khan, J. R. Culham, and M. M. Yovanovich. Convection heat transfer from tube banks in crossflow: Analytical approach. *International Journal of Heat and Mass Transfer*, 49(2526):4831–4838, December 2006.
- [93] S. M. Sanchez. NOLHdesigns spreadsheet. available online via <http://harvest.nps.edu/>, 2011.
- [94] T. M. Cioppa and T. W. Lucas. Efficient nearly orthogonal and space-filling Latin hypercubes. *Technometrics*, 49(1):45–55, February 2007.
- [95] I. Sobol. Sensitivity estimates for nonlinear mathematical models. *Mathematics and Computers in Simulation*, 1:407–414, 1993.
- [96] I. Sobol. On sensitivity estimation for nonlinear mathematical models. *Matematicheskoe Modelirovanie*, 2(1):112–118, 1990.
- [97] Will Usher, Jon Herman, David Hadka, xantares, bernardoct, Fernando Rios, Chris Mutel, and Joeri van Engelen. SALib: Improvements to Morris sampling and Sobol groups/distributions, February 2016.
- [98] A. Saltelli, Marco Ratto, Terry Andres, Francesca Campolongo, Michaela Saisana, Jessica Cariboni, Debora Gatelli, and Stefano Tarantola. *Global Sensitivity Analysis: The Primer*. Wiley-Interscience, February 11 2008.
- [99] Anubhav Pratap Singh and Hosahalli S. Ramaswamy. Simultaneous optimization of heat transfer and reciprocation intensity for thermal processing of liquid particulate mixtures undergoing reciprocating agitation. *Innovative Food Science & Emerging Technologies*, 33:405–415, February 2016.
- [100] T. A. Pimenta and J B L M Campos. Heat transfer coefficients from newtonian and non-newtonian fluids flowing in laminar regime in a helical coil. *International Journal of Heat and Mass Transfer*, 58(12):676–690, March 2013.
- [101] Gianfranco Caruso, Damiano Vitale Di Maio, and Antonio Naviglio. Condensation heat transfer coefficient with noncondensable gases inside near horizontal tubes. *Desalination*, 309:247–253, January 15 2013.
- [102] F. Illan-Gomez, A. Lopez-Belchi, J. R. Garcia-Cascales, and F. Vera-Garcia. Experimental two-phase heat transfer coefficient and frictional pressure drop inside mini-channels during condensation with R1234yf and R134a. *International Journal of Refrigeration*, 51:12–23, March 2015.

- [103] Guangxu Liu, Yanping Huang, Junfeng Wang, and Laurence H. K. Leung. Heat transfer of supercritical carbon dioxide flowing in a rectangular circulation loop. *Applied Thermal Engineering*, 98:39–48, April 5 2016.
- [104] Rodrigo Barraza, Gregory Nellis, Sanford Klein, and Douglas Reindl. Measured and predicted heat transfer coefficients for boiling zeotropic mixed refrigerants in horizontal tubes. *International Journal of Heat and Mass Transfer*, 97:683–695, June 2016.
- [105] K. C. Neethu, A. K. Sharma, Heartwin A. Pushpadass, F. Magdaline Eljeeva Emerald, and M. Manjunatha. Prediction of convective heat transfer coefficient during deep-fat frying of pantoa using neurocomputing approaches. *Innovative Food Science & Emerging Technologies*, 34:275–284, April 2016.
- [106] Canhai Lai, Zhijie Xu, Wenxiao Pan, Xin Sun, Curtis Storlie, Peter Marcy, Jean-Francois Dietiker, Tingwen Li, and James Spenik. Hierarchical calibration and validation of computational fluid dynamics models for solid sorbent-based carbon capture. *Powder Technology*, 288:388–406, January 2016.
- [107] Zhijie Xu, Canhai Lai, Peter William Marcy, Jean-Francois Dietiker, Tingwen Li, Avik Sarkar, and Xin Sun. Predicting the performance uncertainty of a 1-MW pilot-scale carbon capture system after hierarchical laboratory-scale calibration and validation (submitted). *Powder Technology*.
- [108] James Spenik. Development of a circulating fluidized bed for flue gas carbon capture using solid sorbent. Presented at NETL 2011 Workshop on Multiphase Flow Science, Pittsburgh, PA. Available from https://mfix.netl.doe.gov/workshop-files/2011/07_James_Spenik_Development_of_a_Circulating_Fluidized_Bed.pdf, 2011.

CURRICULUM VITAE

William A. Lane

110 Cummington Mall, Boston MA, 02215 • (857) 444-7857 • lanew@bu.edu

EDUCATION

Boston University	Boston, MA
<i>Doctor of Philosophy in Mechanical Engineering</i>	2016
<i>Masters of Science in Mechanical Engineering</i>	2015
Dissertation: Subgrid models for heat transfer in multiphase flows with immersed geometry	
University of New Brunswick	Fredericton, NB
<i>Bachelor of Science in Mechanical Engineering</i>	2012
<i>Diploma in Technology, Management, and Entrepreneurship</i>	
New Brunswick Community College	Moncton, NB
<i>Computer Numerically Controlled Manufacturing Technician</i>	2008
<i>Precision Machinist</i>	

EXPERIENCE

Research

Boston University Computational Energy Laboratory	Boston, MA
<i>Research Assistant</i>	2012–Present
<ul style="list-style-type: none"> • Developed efficient CFD tools for heat transfer in gas-particle reactor systems, achieving increases in computational efficiency by 10,000+ times • Collaborated with 50+ scientists from national labs and 70+ industry partner • Wrote and reviewed technical reports, user manuals, and journal articles 	
University of New Brunswick Manufacturing Laboratory	Fredericton, NB
<i>Research Assistant</i>	2011
<ul style="list-style-type: none"> • Optimized manufacturing methods for research samples, increasing productivity by 5000% and reducing scrap • Trained graduate students on basic machining center operations 	
IntelliCyt Research & Development	Albuquerque, NM
<i>Engineering Intern</i>	2011
<ul style="list-style-type: none"> • Co-developed an alternative pump solution, saving \$500 per product • Developed an alternative pump-stop and sample-injection-port interface 	

Teaching

Boston University Computational Energy Laboratory Boston, MA
Graduate Teaching Assistant 2012

- Co-created and graded assignments and tests
- Facilitated classroom discussions and held office hours

University of New Brunswick Fredericton, NB
Undergraduate Teaching Assistant 2010–2012

- Mechanics of Materials I & II;
- Manufacturing Engineering I & II
- Applied Fluid Mechanics

MENTORING

Massachusetts Institute of Technology Cambridge, MA
Graduate Resident Tutor 2013–Present

- Live-in mentor to 43 undergraduate students studying science and engineering

Boston University Boston, MA
Research Mentor 2012–Present

- Christopher Moulder, Benjamin Schrage
 - Masters students; modeling multiphase flows and solid oxide fuel cells
- Luis Borroso, Kelsey Bilsback
 - Undergraduate students; modeling multiphase heat transfer
- Emily Broude, Adit Namdev
 - High school students; modeling Li-air batteries

VOLUNTEERING

Tutoring Plus Cambridge Cambridge, MA
Tutor 2015–Present

- Tutor high school students in all subjects, including: languages, sciences, mathematics, and information technology

Massachusetts Institute of Technology Electric Vehicle Team Cambridge, MA
Manufacturing Consultant, Team Member 2014–Present

- Advised team on best practices for design-for-manufacturing, dimensioning & tolerancing, and manufacturing processes
- Trained students on CAM software; and setting up and operating lathes, mills, and CNC machining centers

Boston University Summer Pathways Boston, MA
Assistant 2013

- Helped setup and run a hands-on workshop on batteries, fuel cells, and electrochemistry for female high school seniors to build interest in STEM careers

PUBLICATIONS

W. A. Lane and E. M. Ryan, "Verification, validation, and uncertainty quantification of sub-grid models for heat transfer in gas-particle flows with immersed heat transfer cylinders," Chem. Eng. Sci., (Submitted)

W. A. Lane, A. Sarkar, S. Sundaresan, and E. M. Ryan, "Sub-grid models for heat transfer in gas-particle flows with immersed heat transfer cylinders," Chem. Eng. Sci., (Submitted)

W. A. Lane, A. Sarkar, S. Sundaresan, and E. M. Ryan, "Sub-grid filtering of heat transfer in gas-solid flows with immersed heat transfer cylinders," in ASME 2014 IIMECE, Montreal, QC, Canada, 2014.

C. B. Storlie, **W. A. Lane**, and E. M. Ryan, "Calibration of computational models with categorical parameters and correlated outputs via bayesian smoothing spline anova," J. Amer. Statist. Assoc., 2013.

W. A. Lane, C. B. Storlie, C. J. Montgomery, and E. M. Ryan, "Numerical modeling and uncertainty quantification of a bubbling fluidized bed with immersed horizontal tubes," Powder Tech., vol. 253, pp. 733743, Feb. 2014.

W. A. Lane, C. B. Storlie, C. J. Montgomery, and E. M. Ryan, "Modeling and validation of a large scale, multiphase carbon capture system," in ASME 2013 FEDSM, Incline Village, NV, 2013.

PRESENTATIONS & POSTERS

W. A. Lane, E. M. Ryan, A. Sarkar, and S. Sundaresan, "Sub-grid filtering of heat transfer in gas-solid flows with immersed heat transfer cylinders," presented at the ASME 2014 IIMECE, Montreal, QC, Canada, 2014.

W. A. Lane, E. M. Ryan, A. Sarkar, and S. Sundaresan, "Efficient simulations of heated gas-particle flows with immersed horizontal cylinders," poster presented at the XXVI IUPAC Conference on Computational Physics, Boston, MA, 2014.

W. A. Lane, C. B. Storlie, C. J. Montgomery, and E. M. Ryan, "Modeling and validation of a large scale, multiphase carbon capture system," presented at the ASME 2013 FEDSM, Incline Village, NV, 2013.